EXPERIMENTAL AND NUMERICAL ANALYSIS OF HIGH-THROUGHPUT DRILLING OF TITANIUM ALLOYS

By

Rui Li

A dissertation submitted in partial fulfillment
of the requirements for the degree of
Doctor of Philosophy
(Mechanical Engineering)
in The University Of Michigan
2007

Doctoral Committee:

Professor Albert J. Shih, Chair
Professor Amit K. Ghosh
Professor Jun Ni
David Stephenson, Third Wave Systems Inc.

ACKNOWLEDGEMENTS

First of all, I would like to thank my advisor, Dr. Albert Shih, for his guidance and help on my research in the PhD. program. I also thank Dr. Amit Ghosh, Dr. Jun Ni, and Dr. Dave Stephenson for their review of this dissertation and comments as a committee member.

A portion of this research was sponsored by the Heavy Vehicle Propulsion Systems Materials Program and Advanced Materials for High BMEP Engines Program, Office of Transportation Technologies, US Department of Energy. The assistance from Parag Hegde and Paul Prichard of Kennametal, Paul Becker, Raymond Johnson, Laura Riester, Thomas Watkins, and Peter Blau of US Department of Energy, and Nishant Saini, Rahul Aphale, Troy Marusich, and Sarang Garud of Third Wave Systems are greatly appreciated.

Finally, special thanks to my family and friends in Wu Manufacturing Research Center for their supports and encouragements.

TABLE OF CONTENTS

ACKNOWLEDGEMENTS ii

LIST OF FIGURES vii

LIST OF TABLES xii

LIST OF APPENDICES xiii

CHAPTER

- 1. INTRODUCTION 1
  - 1.1. Machinability of Ti 2
  - 1.2. Drilling of Ti 2
  - 1.3. Influence of Machining on Ti Materials 3
  - 1.4. Research Motivation 4
  - 1.5. Outline 7
- 2. EXPERIMENTAL ANALYSIS OF HIGH-THROUGHPUT DRILLING OF TI ALLOYS 9
  - 2.1. Introduction 10
  - 2.2. Experimental Setup and Design 13
    - 2.2.1 Drill Geometry and Material 13
    - 2.2.2. Experiment Setup 14
    - 2.2.3. Tool Wear Observation and Hole Surface Roughness 18
  - 2.3. HSS Twist Drill 19
    - 2.3.1. Dry Drilling (Exp. I) 19
    - 2.3.2. Drilling with External Cutting Fluid Supply (Exp. II) 21
  - 2.4. Drill Performance Comparison (Exp. III) 21

2.5. WC-Co Spiral Point Drill High Throughput Drilling – Effect of Cutting Fluid Supply (Exp. IV) 25
    2.5.1. Dry Drilling 26
    2.5.2. Drilling with External Cutting Fluid Supply 26
    2.5.3. Drilling with Internal Cutting Fluid Supply 28
2.6. WC-Co Spiral High Throughput Drilling – Effect of Feed (Exp. V) 28
2.7. Light Emission in Chip Formation and Chip Morphology 30
2.8. Tool Wear 34
2.9. Concluding Remarks 36
3. SPIRAL POINT DRILL TEMPERATURE AND STRESS IN HIGH-THROUGHPUT DRILLING OF TI 38
3.1. Introduction 39
3.2. Experimental Setup and Design 45
3.3. Spiral Point Drill Geometry and Oblique Cutting Analysis 47
    3.3.1. Drill Solid Modeling 47
    3.3.2. Elementary Cutting Tools (ECT) 49
    3.3.3. Oblique Cutting Mechanics in ECT 49
    3.3.4. Heat Generation 54
3.4. Drill Thermo-Mechanical Modeling Procedure 55
    3.4.1. Finite Element Thermal Model 56
    3.4.2. Inverse Heat Transfer Solution 57
    3.4.3. Finite element drill stress analysis 60
3.5. Drill Temperature Analysis Results 61
    3.5.1. Exp. D183 61
    3.5.2. Exp. W183 64
    3.5.3. Exps. W91 and W61 66
3.6. Drill Deformation 68
3.7. Drill Stress and Failure Prediction 70
3.8. Concluding Remarks 76
4. 3D FINITE ELEMENT MODELING OF HIGH-THROUGPUT DRILLING PROCESS 78

4.1. Introduction.. 79
4.2. Finite Element Drilling Model... 80
    4.2.1. Drill Geometry Model and Oblique Cutting Mechanics........... 80
    4.2.2. Oblique Cutting FEM Modeling... 81
    4.2.3. Equations of Motion.. 82
    4.2.4. Thermal Equations 84
    4.2.5. Material and Friction Models... 85
    4.2.6. Thermo-Mechanical Coupling 87
4.3. Experimental Setup and Design.. 88
4.4. Results and Discussions... 88
    4.4.1. Experimental Validation of Thrust Force and Torque at ECTs .. 88
    4.4.2. FEM Prediction of Tool, Workpiece, and Chip Temperatures and Stresses.. 91
4.5. Concluding Remarks 95
5. METALLURGICAL ANALYSIS AND NANOINDENTATION CHARACTERIZATION OF TI-6AL-4V WORKPIECE AND CHIPS IN HIGH-THROUGHPUT DRILLING 97
5.1. Introduction.. 98
5.2. Experimental Setup... 101
    5.2.1. Sample Preparation 101
    5.2.2. SEM Microstructure Observations.. 102
    5.2.3. Quantitative Analysis of Phase Content by XRD 102
    5.2.4. Analysis of Chemical Composition by Electron Microprobe .. 103
    5.2.5. Nanoindentation Characterization of Mechanical Properties .. 104
5.3. Metallurgical Analysis of Hole Surface and Subsurface Layer............ 105
    5.3.1. Microstructural Observations.. 105
    5.3.2. Quantitative XRD Analysis of Phase Transformation 108
    5.3.3. Chemical Composition Analysis..111
    5.3.4. Nanoindentation Hardness 112
5.4. Drilling Chips 116
    5.4.1. Chip Morphology 116

5.4.3. Nanoindentation hardness 120
5.5. Concluding Remarks 122
6. CONCLUSIONS.. 124
6.1. Major Contributions... 124
6.2. Recommendations for Future Study 128
APPENDICES 130
BIBLIOGRAPHY.. 167

LIST OF FIGURES

Figure 2.1. Top and side view of three types of drill: (a) HSS Twist, (b) WC-Co Twist, (c) WC-Co Spiral, and (d) WC-Co Sprial+Coating. 14

Figure 2.2. Illustration of three stages A, B, and C in drilling. 16

Figure 2.3. Exp. I - thrust force and torque of HSS Twist drill without cutting fluid..... 20

Figure 2.4. Exp. II - thrust force and torque of HSS Twist drill with external cutting fluid supply. 22

Figure 2.5. Exp. III - Thrust force and torque of WC-Co Twist and WC-Co Spiral at 18.3 m/min peripheral cutting speed (1470 rpm). 23

Figure 2.6. Burr formation of three types of drill at 18.3 m/min peripheral cutting speed (1470 rpm). 25

Figure 2.7. Exp. IV - thrust force and torque of WC-Co Spiral drill for high throughput drilling at 183 m/min peripheral cutting speed and 0.051 mm/rev feed under the dry and internal and external cutting fluid supply conditions. 27

Figure 2.8. Exp. V - thrust force and torque of WC-Co Spiral drill for high throughput drilling at 0.75 m/min feed rate and 156 mm3/s material removal rate with internal cutting fluid supply. 30

Figure 2.9. Hole surface roughness under high throughput drilling with the same material removal rate (156 mm3/s) using WC-Co Spiral drill in Exp. VI and V. 31

Figure 2.10. Chip morphology of Ti-6Al-4V generated by WC-Co Spiral drill at 18.3 m/min cutting speed and 0.051 mm/rev feed in dry drilling: (a) whole chip, (b) initial spiral cone (c) steady-state spiral cone, (d) transition between spiral cone and folded long ribbon, and (e) steady-state folded long ribbon. 33

Figure 3.1. Experimental setup: (a) workpiece, drill, fluid hose, and dynamometer and

(b) top view and coordinates of thermocouple tips on drill flank face. 46
Figure 3.2. The drill cross section profile of the spiral point drill. 48
Figure 3.3. Solid model of the spiral point drill: (a) side view and (b) top view with marked seven ECTs. 48
Figure 3.4. The rake angle, inclination angle, and angle between drill axis and ECT cutting edge. 50
Figure 3.5. Illustration of two stages in drilling: (a) partial engagement of drill tip with the workpiece (ECT 1, 2, and 3 engaging the workpiece) and (b) full engagement of the tool tip and all seven ECTs with workpiece. 51
Figure 3.6. Oblique cutting model of an ECT. 52
Figure 3.7. Mesh for the 3D finite element thermal model: (a) side view and (b) top view. 56
Figure 3.8. Flow chart of the inverse heat transfer solution of heat partition on tool-chip interface. 59
Figure 3.9. Flow chart of the inverse heat transfer solution of cutting fluid convection coefficient. 60
Figure 3.10. The heat generation rate per unit length q'_{tool} at seven ECTs after 1.9 mm depth of drilling. 62
Figure 3.11. Comparison of the measured and calculated temperatures at TC1 (input of inverse heat transfer analysis) and TC2 (for validation). 63
Figure 3.12. Temperature distributions along drill chisel and cutting edges as a function of drilling depth. 65
Figure 3.13. Temperature distributions at the drill tip after 10.2 mm depth of drilling in Exps: (a) D183, (b) W183, (c) W91, and (d) W61. 67
Figure 3.14. Drill deformation after 10.2 mm drilling in Exp. D183 (scale factor of deformation: 20). 69
Figure 3.15. Maximum principal stress, σ_1, and minimum stress, σ_3, along the drill chisel and cutting edges after 10.2 mm depth of drilling. 71
Figure 3.16. Comparison of dimensionless stresses, $\bar{\sigma}_r$, $\bar{\sigma}_{m-c}$, and $\bar{\sigma}_{m-m}$, after 10.2 mm depth of drilling in Exp. D183. 74

Figure 3.17. Distributions of dimensionless stress $\bar{\sigma}_{m-m}$ at the drill tip after 10.2 mm depth of drilling in Exps: (a) W183, (b) W91, and (c) W61........................ 75
Figure 4.1. Initial finite element mesh for 3D oblique cutting model of three ECTs. 82
Figure 4.2. Comparison of thrust force and torque of ECTs... 90
Figure 4.3. Temperature distributions in Exp. D183: (a) ECT1, (b) ECT4, and (c) ECT7. 92
Figure 4.4. Peak temperature and stress distributions at tool and workpiece/chip in Exps. D183-W61. 94
Figure 5.1. SEM micrograph of an etched microstructure of Ti-6Al-4V with dark region for HCP α phase and light region for BCC β phase..................................... 98
Figure 5.2. Macroscopic pictures of the Ti-6Al-4V specimen: (a) hole cross-section and (b) chip.. 101
Figure 5.3. PANalytical XPERT-PRO MPD X-ray diffractometer.............................. 102
Figure 5.4. Hysitron triboindenter^{TM}. 105
Figure 5.5. SEM micrographs of the polished and etched cross-sections of drilled holes in Exps. D183 (dry): (a) hole, subsurface, bulk material, (b) subsurface layer, (c) transition layer, and (d) bulk material. 106
Figure 5.6. SEM micrographs of the polished and etched cross-sections of drilled holes with cutting fluid supply (Exps. W183-W61). 107
Figure 5.7. X-ray diffraction patterns of the as-polished bulk material and hole surface of Exp. D183 (intensity plotted as square root of counts to help distinguish the weak peaks from the background).. 109
Figure 5.8. X-ray diffraction spectra of as polished bulk material and hole edge of Exps. D183-W61 and calculated profiles from 30° to 45° diffraction angle. 110
Figure 5.9. Nanoindentation on the workpiece cross-section in Exp. D183: (a) array of indents, (b) indents close to the hole edge, (c) load-displacement curve of indent A away from hole edge, and (d) load-displacement curve of indent B close to the hole edge.. 113
Figure 5.10. Nanoindentation hardness profile of subsurface adjacent to the hole edge in Exps. D183-W61. 115
Figure 5.11. SEM micrographs of chip morphology in Exp. D183: (a) spiral cone chip, (b)

outer edge of the chip, and (c) inner side of the chip. 117
Figure 5.12. SEM micrographs of chips in: (a) Exp. D183 (dry drilling), (b) Exp. W183 (internal cutting fluid supply), and (c) close-up view of regions H (Exp. D183) and J (Exp. W183). 119
Figure 5.13. Nanoindentation on the chip cross-sections in Exp. D183: (a) before etch and (b) after etch (circled indents: indents close to the shear band). 121
Figure 5.14. Chip nanoindentation hardness vs. the distance to the shear band: Exps. (a) D183 and (b) W183. 122
Figure B.1. Drill cutting edge profile (Measured at relative location r/R=0.8). 133
Figure D.1. Experimental setup with workpiece in the spindle and drill in a vertical tool holder. 137
Figure D.2. The spiral point drill and thermocouple locations in the drill flank face: (a) original drill, (b) drills with thermocouples embedded, (c) close-up view of TC1 and TC2, and (c) close-up view of TC3 and TC4. 139
Figure D.3. Ti chip at 2350 rpm spindle speed (73.2 m/min peripheral cutting speed): (a) the spiral cone followed by the folded long ribbon chip morphology, (b) close-up view of the spiral cone chip at the start of drilling, and (c) chip cross-section and chip thickness variation of ECT. 140
Figure D.4. Chip thickness and shear angle of seven ECTs. 142
Figure D.5. Thrust force and torque vs. drilling depth. 143
Figure D.6. Thrust force and torque of seven ECTs. 144
Figure D.7. Comparison of the measured and modeled temperature at four thermocouple locations. 145
Figure D.8. The heat partition factor K at seven ECTs after 1.9 mm depth of drilling. 146
Figure D.9. The heat generation rate per unit length q'_{tool} at seven ECTs after 1.9 mm depth of drilling. 147
Figure D.10. Temperature distribution at the drill tip after 12.7 mm depth of drilling at peripheral cutting speeds: (a) 24.4, (b) 48.8, and (c) 73.2 m/min. 150
Figure D.11. Temperature along the drill chisel and cutting edges at 12.7 mm depth of drilling. 151
Figure D.12. Temperature along the drill chisel and cutting edges at 73.2 m/min cutting

speed. 152
Figure E.1. Experimental setup of embedded foil tool-work thermocouple method. ... 155
Figure E.2. Drill cutting edge temperature distribution at 10 m/min peripheral cutting speed and 0.05 mm/rev feed using a HSS conventional twist drill. 156
Figure F.1. Parameterization of a standard two flute twist drill.................................. 158
Figure F.2. Finite element mesh for 3D drilling model. 159
Figure F.3. Comparison of modeling and experimental thrust forces and torques. 161
Figure F.4. FEM results: (a) drill, chip, and workpiece temperature, (b) chip and workpiece temperature, and (c) chip and workpiece von Mises stress (13.7 m/min peripheral cutting speed). 162
Figure F.5. FEM results of drill: (a) temperature and (b) mises stress distributions (13.7 m/min peripheral cutting speed). 164
Figure F.6. Peak temperature and von Mises stress vs. drill peripheral cutting speed. 165

LIST OF TABLES

Table 2.1. Experiment process parameter selection, material removal rate, drill life, drilling time, and summary of the thrust force and torque, energy, and length of spiral cone chip. 17
Table 3.1. Experiment process parameters for high-throughput drilling of Ti-6Al-4V with 4.97 mm/s feed rate and 384 mm3/s material removal rate. 47
Table 3.2. Root mean square and percentage errors of the predicted and measured temperatures. 64
Table 3.3. Drill deformation under the thermo-mechanical and mechanical-only conditions. 70
Table 4.1. Comparison of thrust force, torque, and power of the whole spiral point drill89
Table 5.1. Comparison of Al and V content in the chemical analysis of cross-sectional subsurface layer (within 10 μm from the hole surface) in Exps. D183 and W183 and the bulk material. 111
Table A.1. Material properties of CP Ti and Ti-6Al-4V.......... 131
Table B.1. Drill geometrical parameters.......... 132
Table D.1. Root mean square (RMS) and percentage errors.......... 149

LIST OF APPENDICES

A. Material Properties of CP Ti and Ti-6Al-4V 131
B. Geometrical and Grinding Parameters of Spiral Point Drill 132
C. Oblique Cutting Analysis of Elementary Cutting Tool 134
D. Inverse Heat Transfer Solution of Drill Temperature in Drilling of Commercially Pure Ti 136
E. Drill Temperature Measurement Using Embedded Foil Tool-Work Thermocouple Method 154
F. 3D Finite Element Modeling of Low Speed Drilling of Ti-6Al-4V Using Conventional Drills 157

CHAPTER 1

INTRODUCTION

Titanium (Ti) and its alloys are light-weight, corrosion resistant, and high temperature materials. Titanium has the highest strength-weight ratio of all commonly used metals up to 550°C (Hurless and Froes, 2002). Titanium is the ninth most abundant element and the fourth most abundant metal in earth's crust (Kraft, 2003). However, the extraction and processing cost to produce the raw Ti material is high due to its high free energy for reduction of oxide (Kraft, 2003). The high cost has limited Ti to the military, aerospace, racing, and other applications in which the material cost is not a key factor.

As reported by Hurless and Froes (2002), Kraft (2003), and Turner and Hansen (1993), several emerging technologies have been developed to reduce the cost of producing raw Ti material in recent years. This has brought about the potential of low cost Ti and the possibility for automotive applications (Kraft, 2002). While reducing the material cost can go a long way toward the usage of Ti, the high machining cost is another major technical barrier that needs to be overcome.

1.1. Machinability of Ti

Ti and its alloys have low thermal conductivity (16.4 W/m-K for grade two commercially pure (CP) Ti and 6.6 W/m-K for grade five Ti-6Al-4V). During the machining process, most of energy generated in deforming the chip and in overcoming friction between the tool and workpiece is converted to heat, producing very high temperatures in the deformation zones and surrounding regions of the chip, tool and workpiece. The high temperature in a small, concentrated area at the tool tip softens the tool material and promotes the tool diffusion wear. This high temperature and severe tool wear have hindered the productivity and increased the cost of machining Ti for industrial applications. To enable the cost-effective machining of Ti alloys, research efforts should be directed to overcome these technical challenges.

1.2. Drilling of Ti

Among all the machining processes, drilling is a widely used machining process and has considerable economical importance because it is usually among final steps in the fabrication of mechanical components. The tool geometry and material deformation in drilling are complicated. In the drill center, so called chisel edge, cutting speed is close to zero and work-material is plowed under a high negative rake angle. Along the drill cutting edge, the cutting speed and rake angle both vary with respect to the distance from the drill center. The outmost point on the cutting edge has the highest cutting speed, called the peripheral cutting speed.

Technical difficulties of Ti drilling include:

1. High drill temperature
2. Severe drill wear, even at moderate feed rate and spindle speed
3. Limited cutting speed and productivity
4. Chip ejection
5. Exit burr formation – for conventional twist drill

Due to these difficulties, the material removal rate of Ti drilling is typically very low.

Although Ti drilling has been widely utilized in industry, research publications are still limited on this subject. Sakurai et al. (1992a, 1992b, 1996) have conducted a series of experiments in drilling of Ti-6Al-4V. Effects of coated and surface-treated high speed steel drills and cutting speed and feed on thrust force and torque (Sakurai et al., 1992a) and benefits of the vibratory motion of the drill (Sakurai et al., 1992b) and the variable feed for chip ejection (Sakurai et al., 1996) were studied. Other researches in Ti drilling include Arai and Ogawa (1997) on the high pressure (7 MPa) cutting fluid assisted drilling, Dornfeld et al. (1999) and Min et al. (2001) on the burr formation, Reissig et al. (2004) on temperature analysis by metallurgical analysis, and Cantero et al. (2005) on the dry drilling tool wear and workpiece subsurface damage,

1.3. Influence of Machining on Ti Materials

Ti has two crystal structures: the hexagonal closed-pack (HCP) α phase, and body centered cubic (BCC) β phase (Lütjering and Williams, 2003; Donachie, Jr., 1988). Pure Ti is 100% α at room temperature. The allotropic transformation from α to β phase takes place at the β transus temperature 883°C. For Ti-6Al-4V, Vanadium (V) is added to pure Ti to stabilize the β phase by lowering the β transus temperature (Lütjering and Williams, 2003; Donachie, Jr., 1988). Aluminum (Al) is added to increase the β transus temperature (Lütjering and Williams, 2003; Donachie, Jr., 1988). With 6 wt% of Al and 4 wt% V, the β transus temperature of Ti-6Al-4V is 980°C, beyond which Ti is 100% β (Donachie, Jr., 1988). Because Ti-6Al-4V is a two-phase alloy, it can be heat treated and aged to provide exceptional properties like the high strength-density ratio at elevated temperature (Donachie, Jr., 1988). Generally, higher α content results in higher creep resistance and high-temperature strength, while higher β content leads to higher density and room-temperature strength (Donachie, Jr., 1988).

In high-throughput drilling of Ti-6Al-4V, the workpiece and chips undergo large deformation at high strain rate and temperature, which can alter the microstructure and material properties of the Ti work-material and chips.

1.4. Research Motivation

The objective of this research is to investigate the drilling mechanism and the new technologies to overcome the technical difficulties mentioned in section 1.2 and to achieve the high-throughput drilling of Ti alloys. This will be pursued in the following directions:

1. Experimental investigation of high-throughput drilling (Li and Shih, 2006; Li et al., 2007): to investigate the feasibility of high-throughput drilling by selecting the

appropriate drill geometry and drilling conditions and study the drilling mechanism, drill wear, and chip formation under high-throughput drilling condition, in order to increase the productivity.

2. Analysis of drill temperature and stress (Li and Shih, 2007a; Li and Shih, 2007b; Huang et al., 2007) : to analyze the spatial and temporal distributions of the temperature and stress of a spiral point drill in high-throughput drilling of Ti-6Al-4V by using a thermal-mechanical finite element model of the drill.
3. Finite element modeling of drilling process (Li and Shih, 2007c): to study the chip formation process of high-throughput drilling of Ti-6Al-4V by using updated-Lagrangian finite element modeling.
4. Metallurgical analysis and nanoindentation characterization of Ti workpiece and chips (Li et al., 2006): to investigate the influence of high temperature, large strain, and high strain rate deformation of high-throughput drilling on the $\beta \rightarrow \alpha$ phase transformation and mechanical properties.

Increasing the drilling productivity is a main purpose of this study. To increase the drilling productivity, the material removal rate can be increased by increasing the cutting speed and feed rate, among which using high cutting speed is the most common way (Rahman et al., 2003). The effect of feed in drilling is an area that has not been studied extensively, so it becomes one of the research goals of this study. Drill geometry has an important influence on tool performance. Due to the high temperature in drilling Ti, the supply of cutting fluid is usually needed to reduce the temperature. In this research, the appropriate drill geometry and cutting fluid supply method are investigated to achieve the high productivity.

The thermal analysis of the drill is conducted since the tool temperature is expected to be high and a critical factor of tool life in Ti drilling. Duo to the fact that the heat generation rate and drill temperature distribution during Ti drilling are difficult to measure directly, and also because new drill geometry design and drill material have both advanced remarkably in the past years, detailed thermal modeling of advanced drills is essential for Ti drilling development. In the thermal modeling of drilling process, the heat partition between the drill and chip is recognized as one of the most difficult parameters to determine (Agapiou and Stephenson, 1994). The inverse heat transfer method is utilized in this study to estimate the heat partition on the tool-chip contact area and convection heat transfer coefficient of cutting fluid. For high-throughput Ti drilling, severe deformation and highly localized stresses are expected in the drill and will eventually lead to the drill failure. The temperature induced thermal stress combined with the mechanical stress caused by cutting forces is analyzed to predict the location of drill failure.

Yang and Liu (1999) concluded that, to further reduce the cost of effective machining of Ti, a better understanding of the underlying mechanism of Ti machining process was necessary through better process and performance models, thermal modeling, and finite element simulation. Advancements in machining process modeling have demonstrated the capability to provide reliable predictions of the performance of cutting process and the influence of the process parameters on the product quality (Ehmann et al., 1997). Although some drilling models have been conducted before, they all have limited accuracy or not suitable for simulating Ti drilling process. The updated-Lagrangian method is suitable for simulating Ti drilling, but has not yet been applied to predict the thrust force and torque in drilling due to the technical difficulty in modeling the material deformation under the complicated drill geometry, especially the large negative rake angle at the chisel edge. In this study, the chisel and cutting edges of a spiral point drill were treated as a series of straight-cutting-edge elementary cutting tools with various rake and inclination angles. The oblique-cutting finite element modeling is applied to study the cutting forces and material deformation of each elementary cutting tool.

In high-throughput drilling of Ti-6Al-4V, the workpiece and chips undergo large deformation at high strain rate and temperature, which can alter the microstructure and material properties of the Ti work-material and chips. To study the Ti-6Al-4V hole surface and subsurface and the chips in high-throughput drilling tests, the metallurgical analyses, including SEM, XRD, electron microprobe, and nanoindentation characterization are conducted.

1.5. Outline

Chapter 2 investigates the feasibility of high throughput drilling of Ti alloys through a systematic experimental analysis. The tool material and geometry and drilling process parameters, including cutting speed, feed, and fluid supply, are studied to evaluate the effect on drill life, thrust force, torque, energy, and burr formation. The tool wear mechanism, hole surface roughness, and chip light emission and morphology for high throughput drilling are investigated. Supplying the cutting fluid via through-the-drill holes has proven to be a critical factor for drill life. The balance of cutting speed and feed is found to be essential to achieve long drill life and good hole surface roughness.

Chapter 3 analyzes spatial and temporal distributions of the temperature and stress of a spiral point drill used in high-throughput drilling of Ti-6Al-4V. A finite element thermal model using the inverse heat transfer method is applied to find the heat partition on the tool-chip contact area and convection heat transfer coefficient of cutting fluid. Thermo-mechanical finite element analysis is applied to solve the drill stress distribution. The location of drill failure is analyzed using various failure criteria.

Chapter 4 introduces a 3D updated-Lagrangian finite element simulation of high-throughput drilling process. In this chapter, the chisel and cutting edges of a spiral point drill are treated as a series of straight-cutting-edge elementary cutting tools. The oblique-cutting finite element modeling is applied to study the cutting forces and material deformation of each elementary cutting tool.

Chapter 5 studies the influence of high temperature, large strain, and high strain rate deformation in high-throughput drilling on the phase transformation and mechanical properties of Ti-6Al-4V hole surface and subsurface and the chips. The metallurgical analyses, including SEM, XRD, electron microprobe, and nanoindentation characterization are conducted

The conclusions and recommendations for future work are presented in Chapter 5.

CHPATER 2

EXPERIMENTAL ANALYSIS OF HIGH-THROUGHPUT DRILLING OF TI ALLOYS

Experiments of high throughput drilling of Ti-6Al-4V at 183 m/min cutting speed and 156 mm^3/s material removal rate using a 4 mm diameter WC-Co spiral point drill were conducted. The tool material and geometry and drilling process parameters, including cutting speed, feed, and fluid supply, were studied to evaluate the effect on drill life, thrust force, torque, energy, and burr formation. The tool wear mechanism, hole surface roughness, and chip light emission and morphology for high throughput drilling were investigated. Supplying the cutting fluid via through-the-drill holes has proven to be a critical factor for drill life, which can be increased by 10 times compared to that of dry drilling at 183 m/min cutting speed and 0.051 mm/rev feed. Under the same material removal rate of 156 mm^3/s with a doubled feed of 0.102 mm/rev (91 m/min cutting speed), over 200 holes can be drilled. The balance of cutting speed and feed is essential to achieve long drill life and good hole surface roughness. This study demonstrates that, using proper drilling process parameters, spiral point drill geometry, and fine-grained WC-Co tool material, the high throughput drilling of Ti alloy is technically feasible.

2.1. Introduction

In drilling, high material removal rate (MRR) and long drill life are essential to increase productivity and reduce cost. To achieve the desired MRR, high cutting speed and feed per revolution of drill are required (Stephenson and Agapiou, 2005). This research investigates the process parameters, tool material, and drill geometry to achieve the high throughput drilling of Ti-6Al-4V, a material widely used in aerospace industry.

Feed and cutting speed are two important process parameters to achieve the desired MRR and productivity in drillining. The use of better tool material with higher strength and hot hardness (Stephenson and Agapiou, 2005) and better drill geometry design can enable larger feed and cutting speed in drilling. The effect of feed in drilling is an area that has not been studied extensively, so it becomes one of the research goals of this study. The feed for turning of Al alloys can be 1.00 and 2.05 mm/rev using high speed steel (HSS) and tungsten carbide in cobalt matrix (WC-Co) tools, respectively (Machining Data Handbook, 1980). Gray cast iron can be turned at 0.75, 0.65, and 1.00 mm/rev with HSS, ceramic, and WC-Co tools (Machining Data Handbook, 1980). In comparison, the recommended maximum feed is small for Ti-6Al-4V, 0.40 mm/rev, using a WC-Co tool (Machining Data Handbook, 1980). In drilling, the maximum recommended feed depends on the drill diameter (Machining Data Handbook, 1980). For drilling using a WC-Co twist drill with diameter less than 6 mm, the feeds for Al alloys, gray cast iron, and Ti-6Al-4V are 0.18, 0.10, and 0.05 mm/rev, respectively (Machining

Data Handbook, 1980). It is obvious that the recommended feed for machining Ti is small.

Besides feed, cutting speed can also be increased to improve the MRR. Depending on the work- and tool-materials, the cutting speed in machining may vary considerably (Schulz and Moriwaki, 1992). In turning, Al alloys can be machined at 300 m/min using HSS and 600 m/min using WC-Co tool materials (Trent and Wright, 2000). For gray cast iron, typical maximum cutting speeds are 40, 120, and 450 m/min, using HSS, WC-Co, and ceramic cutting tools, respectively (Machining Data Handbook, 1980). Machining Ti alloys at high speed is difficult because of the inherent material properties, particularly the low thermal conductivity, which results in high tool temperature at increased cutting speed. High tool temperature accelerates tool wear and limits drill life (Li and Shih, 2006). For Ti alloys, over 100 m/min can be considered as a high speed in turning (Kitagawa et al., 1997; Zareena, 2001). The cutting speed of drilling is typically much lower than that of turning. Using a HSS twist drill with diameter less than 6 mm, the maximum recommended peripheral cutting speeds for Al alloys, gray cast iron, and Ti-6Al-4V are 105, 49, and 11 m/min, respectively (Machining Data Handbook, 1980). With internal cutting fluid supply, the cutting speeds are increased to 245, 90, and 30 m/min using a WC-Co twist drill with diameter less than 6 mm, for Al alloys, gray cast iron, and Ti-6Al-4V, respectively (Machining Data Handbook, 1980). The recommended cutting speed for drilling Ti alloys is very low. This has hindered the productivity and increased the cost of machining Ti for industrial applications.

Machining of Ti-6Al-4V at high cutting speed has been studied. In turning, Lei and Liu (2002) achieved 480 m/min cutting speed at 0.15 mm/rev feed using a rotary

WC-Co tool. Zareena et al. (2001) conducted face milling at 400 m/min cutting speed and 0.1 mm/tooth feed using a polycrystalline cubic boron nitride (PCBN) tool insert. Balkrishna and Shin (2002) using a polycrystalline diamond (PCD) tool in face milling reached 180 m/min cutting speed and 0.051 mm/rev feed. Norihiko (2002) was able to use a WC-Co tool for end milling at 283 m/min cutting speed and 0.05 mm/tooth feed. Machining of other Ti alloys with high cutting speed has also been investigated: Kitagawa et al. (1997) studied the end milling of Ti-6Al-6V-2Sn at a cutting speed up to 628 m/min and 0.06 mm/tooth feed using a WC-Co tool and Hirosaki et al. (2004) investigated the turning of Ti-6Al-2Nb-1Ta at 252 m/min cutting speed and 0.15 mm/rev feed and milling at 498 m/min cutting speed and 0.05 mm/tooth feed using a binder-less PCBN tool. It is noticed that all these studies were limited in either turning or milling. The research of high throughput drilling of Ti alloys is still lacking.

High throughput drilling has been studied by Lin and Ni (1999) using coated WC-Co drills with specially designed drill geometry. For cast Al and gray cast iron, 533 and 235 m/min peripheral cutting speed and 0.50 and 0.36 mm/rev feed, respectively, have been achieved (1999). In the past decade, drills with advanced geometry and new fine-grained WC-Co tool material have become commercially available. The research presented in this paper is a systematic study of the performance of conventional HSS twist drills and advanced WC-Co web thinned and spiral point drills for high throughput drilling of Ti-6Al-4V. The thrust force, torque, drill life, burr formation, and chip morphology are investigated. The experimental setup and design is first introduced in Sec. 2.2. Drilling results for HSS drill are presented in Sec. 2.3. A performance comparison of three types of drill at the same peripheral cutting speed and feed is summarized in Sec. 2.4. In Secs. 2.5 and 2.6, the spiral point drill for high throughput drilling is discussed. The light emission in chip formation and chip morphology are elaborated in Sec. 2.7. The tool wear is analyzed in Sec. 2.8.

2.2. Experimental Setup and Design

2.2.1 Drill Geometry and Material

Four types of drills, as shown in Figure 2.1, were studied. All drills were double-flute and 4 mm in diameter.

1. HSS twist drill (Greenfield Industries 44210): This M2 HSS twist drill, denoted as HSS Twist, was a conventional drill used as the baseline for Ti drilling tests. The drill had 118° point angle, 30° helix angle, and 0.7 mm web thickness.
2. WC-Co web thinned point twist drill (Kennametal KWCD00344): This uncoated drill, denoted as WC-Co Twist, also had 118° point angle and 30° helix angle. The web was thinned to 0.45 mm. A notch was ground at the chisel edge corner for web thinning (Stephenson and Agapiou, 2005). The tool material was Kennametal grade K600 WC with 10% Co.
3. WC-Co spiral point drill (Kennametal K285A01563): This uncoated drill, denoted as WC-Co Spiral, had advanced drill geometry design. The drill point with S-shaped chisel edge had lower negative rake angle than that of the conventional twist drill (Ernst and Haggerty, 1958; Li and Shih, 2006). The low negative rake angle was expected to generate low thrust force. The tool material was

Kennametal grade K715 WC with 9.5% Co. The drill had 135° point angle, 30° helix angle, and 0.72 mm web thickness.

4. TiAlN coated WC-Co spiral point drill (Kennametal K285A01563): This TiAlN coated drill, denoted as WC-Co Spiral+Coating, had the same geometrical design as WC-Co Spiral.

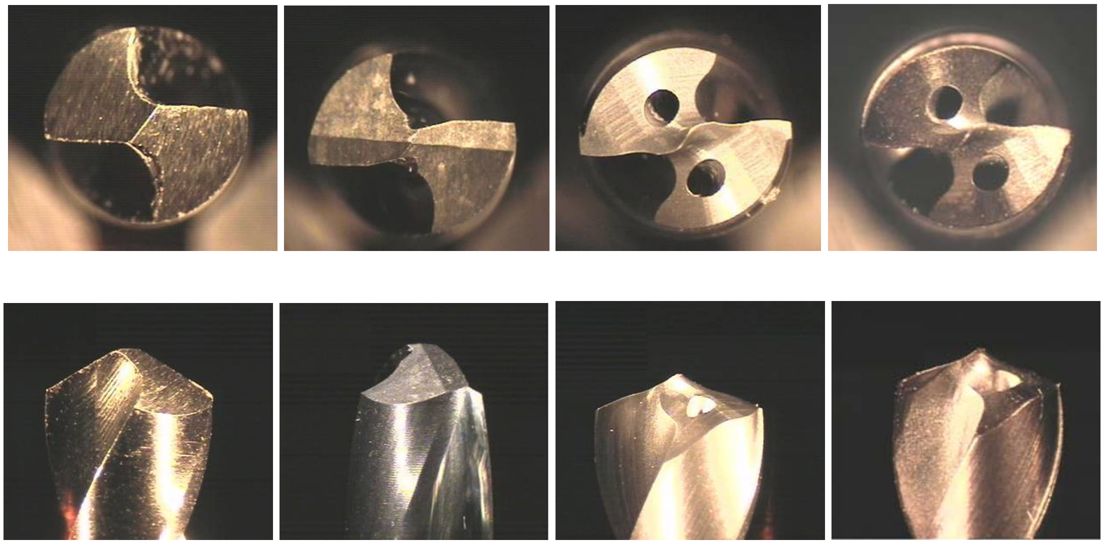

(a) (b) (c) (d)

Figure 2.1. Top and side view of three types of drill: (a) HSS Twist, (b) WC-Co Twist, (c) WC-Co Spiral, and (d) WC-Co Spiral+Coating.

2.2.2. Experiment Setup

Cutting fluid and delivery method are important to reduce the tool and workpiece temperatures and enhance the drill life (Trent and Wright, 2000). Two ways to supply the cutting fluid, internally from two through-the-drill holes and externally from outside the drill, were studied. The cutting fluid was 5% CIMTECH 500, a synthetic metalworking fluid.

The workpiece material was 6.35 mm thick Ti-6Al-4V plate with Knoop hardness of 4.34 GPa. The thrust force and torque during drilling were measured using a Kistler 9272 dynamometer.

Five sets of experiments, marked as Exps. I, II, III, IV, and V, were conducted. Table 2.1 summarizes the type of drill, cutting fluid supply, peripheral cutting speed, and feed in each drilling experiment. Exp. I was conducted using the HSS Twist drill at three peripheral cutting speeds, 9.1, 13.7, and 18.3 m/min and a constant feed of 0.051 mm per revolution or 0.025 mm feed per tooth, without cutting fluid. To study the effect of cutting fluid, Exp. II was conducted with external cutting fluid supply, HSS Twist drill, higher peripheral cutting speeds at 13.7, 18.3, and 27.4 m/min, and 0.051 mm/rev feed. Exp. III was conducted to compare the thrust force, torque, energy, and burr formation of three drills (HSS Twist, WC-Co Twist, WC-Co Spiral, and WC-Co Spiral + Coating) at 18.3 m/min peripheral cutting speed and 0.051 mm/rev feed without cutting fluid. Exp. IV studied the high speed drilling of Ti using WC-Co Spiral drills. By gradually increasing the drill rotational speed and maintaining the same feed at 0.051 mm/rev, drilling at 183 m/min peripheral cutting speed, which corresponded to 14700 rpm of the drill, was possible under the dry drilling condition. Three sets of drilling under dry and external and internal (through-the-drill) cutting fluid supply conditions were conducted to evaluate the drill life and drilling performance. Using the same WC-Co Spiral drill with internal cutting fluid supply, Exp. V studied the balance of feed and cutting speed on drill life in high throughput drilling of Ti under the same MRR. The feed was gradually increased from 0.051 to 0.076, 0.102, and 0.152 mm/rev at corresponding drill rotational speed to maintain the same 0.75 m/min feed rate. The drill life, hole surface roughness, chip morphology, thrust force, torque, and energy were studied. For all five sets of drilling experiments, chips were collected, and drills and workpieces were cooled by free convection in air by at least 60 s after drilling each hole. The drill life was defined as the number of holes drilled before tool breakage.

Figure 2.2 illustrates the three stages, marked as A, B, and C, in drilling. Stage A occurs when the drill has traveled by a distance *d*, which is called the drill point length, from the initial contact. For the HSS Twist, WC-Co Twist, and WC-Co Spiral (WC-Co Spiral+Coating) drills used in this study, *d* is equal to 1.24, 1.19, and 0.74 mm, respectively. Neglecting the deformation of the workpiece, the drill cutting edge becomes fully engaged with the workpiece at this stage. When the drill tip reaches the back surface of the plate without considering material deformation, as shown in Figure 2.2, it is marked as the Stage B. Stage C is defined when the drill cutting edge is disengaged with the workpiece without considering the deformation of the workpiece and burr formation.

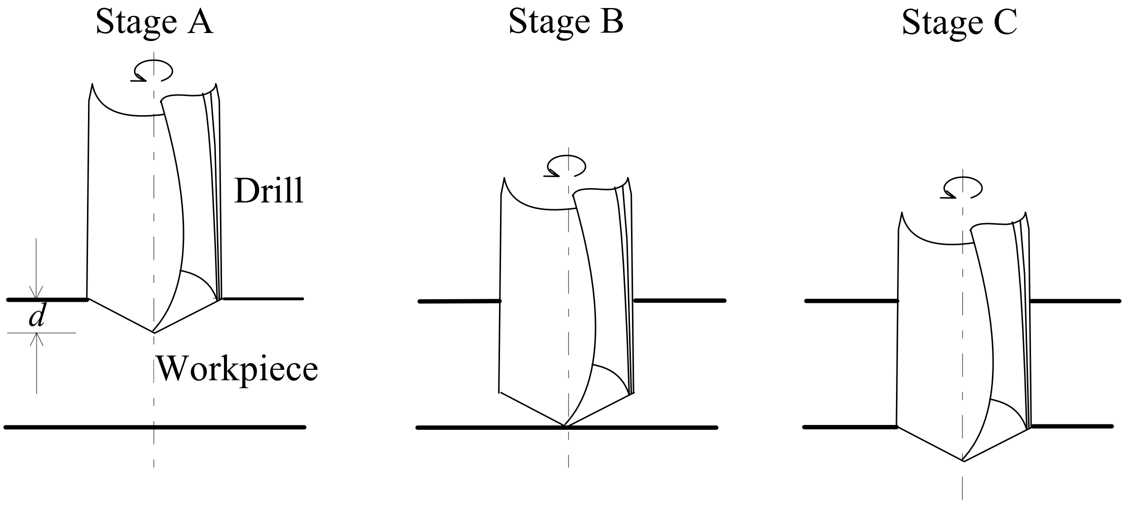

Figure 2.2. Illustration of three stages A, B, and C in drilling.

Table 2.1. Experiment process parameter selection, material removal rate, drill life, drilling time, and summary of the thrust force and torque, energy, and length of spiral cone chip.

Exp.	I			II			III				IV			V		
Drill type	HSS Twist			HSS Twist			HSS Twist	WC-Co Twist	WC-Co Spiral	WC-Co Sprial+Coating	WC-Co Spiral			WC-Co Spiral		
Cutting fluid supply*	No			Ext			No				No	Ext	Int	Int		
Peripheral cutting speed (m/min)	9.1	13.7	18.3	13.7	18.3	27.4	18.3				183			122	91	61
Feed (mm/rev)	0.051			0.051			0.051				0.051			0.076	0.102	0.152
Feed rate (mm/min)	37.2	56.0	74.9	56.0	74.9	112.1	74.9				749			749		
MRR (mm^3/s)	7.7	11.6	15.6	11.6	15.6	23.3	15.6				156			156		
Drill life (Number of holes)	N/A	N/A	2	N/A	N/A	2	2	N/A	N/A	N/A	10	14	101	153	205	164
Drilling time** (s)	12.2	8.1	6.1	8.1	6.1	4.1	6.1	6.1	5.7	5.7	0.57			0.57		
F_A (N)	401–413	464–486	390	417–420	430–446	400	390	233–255	166–169	290-313	132–144	145–167	172–202	184–195	258–292	277–315
T_A (N-m)	0.40–0.44	0.39–0.40	0.36	0.40–0.44	0.39–0.41	0.3	0.36	0.23–0.32	0.38–0.42	0.37-0.39	0.24–0.29	0.28–0.31	0.47–0.53	0.72–0.92	1.22–1.34	1.26–1.51
F_m (N)	0.40–0.44	464–486	390	420–434	430–446	485	390	235–257	177–181	325-360	166–201	145–181	205–241	205–210	264–327	304–334
T_m (N-m)	0.56–0.58	0.72–0.79	0.80	0.50–0.54	0.70–0.76	0.79	0.80	0.76–0.86	0.42–0.49	0.44-0.57	0.96–1.31	0.53–1.45	1.02–1.48	1.47–1.56	1.72–3.61	2.01–2.58
E (J)	391–400	426–455	453	367–390	387–427	412	453	603–628	351–375	358-407	497–709	504–574	762–995	1027–1119	1288–2415	1432–1803
Length of spiral cone chip (mm)	20–35	12–20	N/A	14–24	14–20	N/A	N/A	25–35	48–54	40-58	0–5	0–10	18–25	18–30	20–30	5–15

*: Ext: external cutting fluid supply, Int: internal, through-the-drill cutting fluid supply (at 0.2 MPa), No: no cutting fluid supply

**: Through 6.35 mm thick plate

The torque and force changed throughout the drilling process. Values of thrust force and torque at Stage A, denoted as F_A and T_A, and maximum thrust force and torque during drilling, denoted as F_m and T_m, respectively, were compared to quantify different drilling conditions.

Besides thrust force and torque, another variable indicating the effect of drilling condition is the energy E required to drill a hole. Drilling energy E can be expressed as:

$$E = \int_l F dl + \int_l \frac{2\pi T}{f} dl \tag{2.1}$$

where l is the depth of drilling, F is the thrust force, T is the torque, and f is the feed per revolution. The E was found to be dominated by the torque term, which accounted for over 99% of the E, based on the experimental data of all drilling tests in this research.

2.2.3. Tool Wear Observation and Hole Surface Roughness

A Hitachi S-4700 scanning electron microscope (SEM) was used to examine the tool wear. Energy dispersive spectroscopy (EDS) method was applied to further study the tool wear mechanism.

The test pieces were cut in two along the hole axis to measure the roughness of hole surface using a Taylor Hobson Talysurf Model 120 stylus surface profilometer with 0.8 mm cutoff length and 100:1 bandwidth ratio. For each drilling test in Exp. V, the first three holes were measured. For each hole, three roughness readings were taken, approximately 45° apart circumferentially.

2.3. HSS Twist Drill

The performance of HSS Twist drill under dry (Exp. I) and with external cutting fluid supply conditions (Exp. II) was investigated.

2.3.1. Dry Drilling (Exp. I)

Figure 2.3 shows the thrust force and torque as a function of drilling depth using the HSS Twist drill without cutting fluid. The time to reach Stage C, i.e., the drill penetrating 6.35 mm thick workpiece, is 12.2, 8.1, and 6.1 s at 9.1, 13.7, and 18.3 m/min peripheral cutting speeds, respectively. This time is labeled in Figure 2.3. Cutting speed has significant effect on the drill performance. No obvious wear was observed on the HSS Twist drill after 3 holes at 9.1 and 13.7 m/min peripheral cutting speeds. At 18.3 mm/min peripheral cutting speed, the drill tip melted in the second hole due to high temperature. The HSS Twist drill, a low-cost, conventional tool, has limited cutting speed and material removal rate in drilling Ti.

By increasing the cutting speed from 9.1 to 13.7 m/min, the thrust force rise by about 50 N or 12%. This is because the strain-rate hardening outweighs thermal softening (Trent and Wright, 2000). At both speeds, the thrust force decreased slightly after Stage A. Between Stages B and C, the thrust force rapidly reduced because the chisel and cutting edges gradually disengaged with the workpiece. The torque increased, instead of decreasing as in the thrust force, after Stage A, because the resistance to chip ejection (Ke, 2003) had a more significant effect on torque. Torque started to decrease after Stage B at 9.1 m/min cutting speed. At 13.7 m/min cutting speed, the torque started to peak after Stage B, i.e., the drill chisel edge had already penetrated the workpiece. The difficulty for chip ejection resulting from the chip welding to the drill flute near the cutting edge was the likely cause. It was also confirmed by the difficulty to remove the chip from the drill after each drilling. At 18.3 m/min cutting speed, the curves of thrust force and torque last longer past Stage C due to the melting of drill tip.

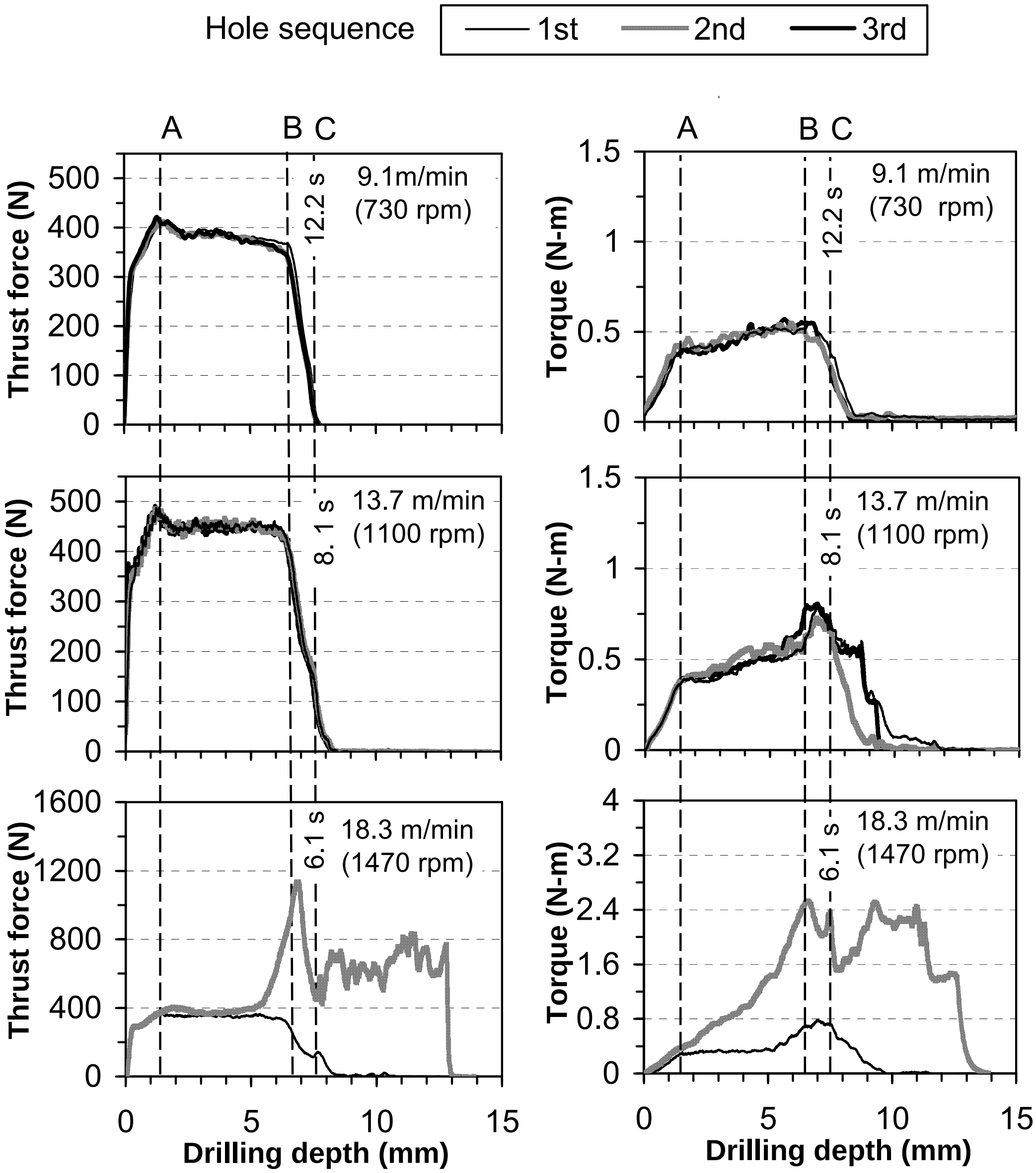

Figure 2.3. Exp. I - thrust force and torque of HSS Twist drill without cutting fluid.

2.3.2. Drilling with External Cutting Fluid Supply (Exp. II)

Figure 2.4 shows the thrust force and torque at 13.7, 18.3, and 27.4 m/min peripheral cutting speeds with external cutting fluid supply. At 13.7 m/min cutting speed, compared to dry drilling, the thrust force and torque were both reduced. At 18.3 m/min, the maximum cutting speed in dry drilling, the drill lasted more than 3 holes with no obvious wear on cutting edges. This is a significant improvement of drill life from the dry drilling condition. At both cutting speeds, the benefit of cutting fluid is obvious. When the peripheral cutting speed further increased to 27.4 m/min, which was still low for effective material removal, the drill tip melted in 2 holes. This illustrates the limited cutting speed and MRR of the conventional HSS twist drill in Ti machining.

The T_A, F_A, T_m, F_m, and E for all drilling tests are summarized in Table 2.1. For HSS Twist drill, as shown in Exps. I and II, at 13.7 m/min peripheral cutting speed, the supply of cutting fluid decreased T_m by about 30%, F_m by about 10%, F_A by about 10%, and E by 15%. With the combination of low energy input and the cooling effect of cutting fluid, the drill life was improved.

2.4. Drill Performance Comparison (Exp. III)

Figure 2.5 shows the thrust force and torque for WC-Co Twist and WC-Co Spiral drills at the same 18.3 m/min peripheral cutting speed and 0.051 mm/rev feed with no cutting fluid.

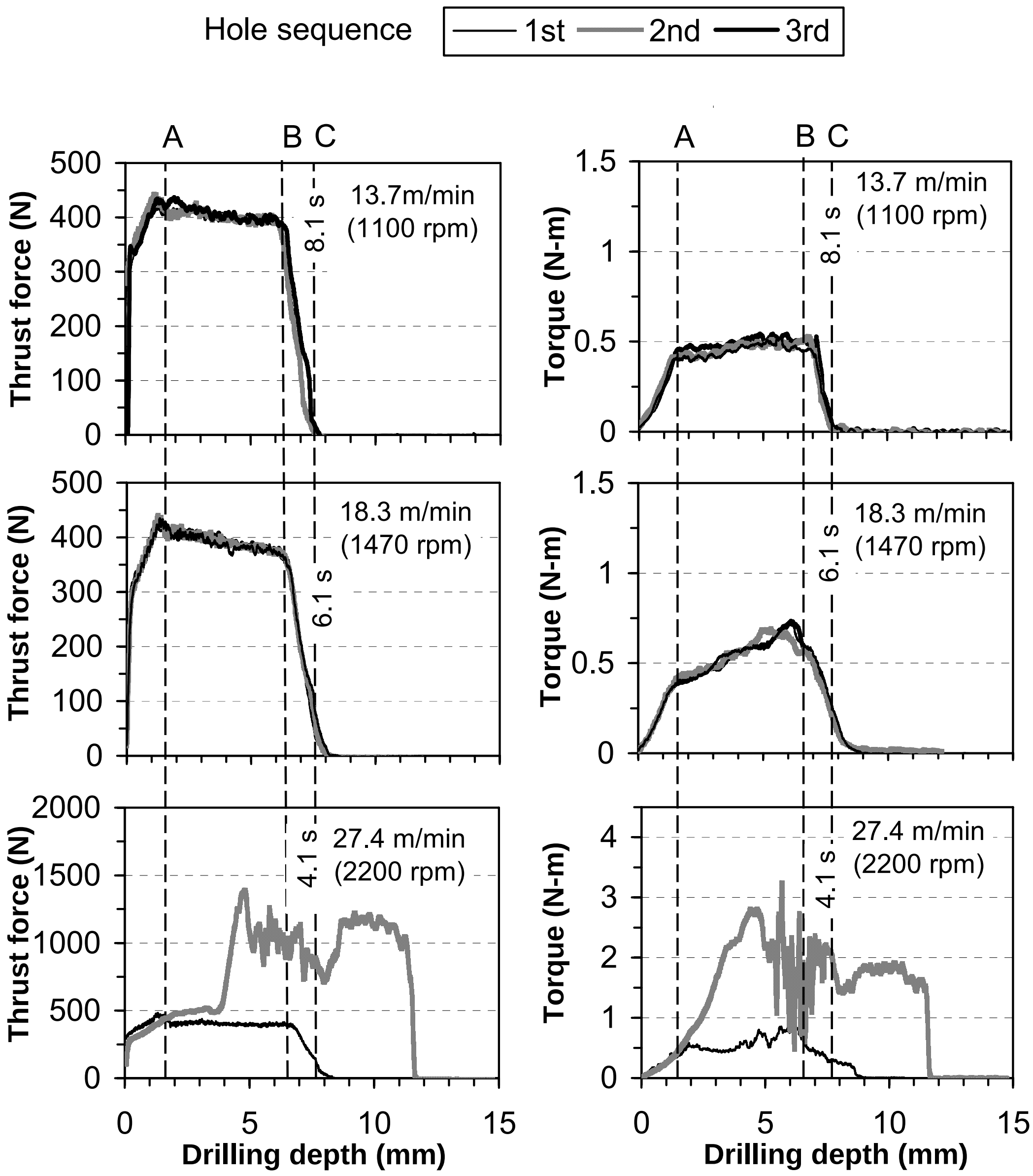

Figure 2.4. Exp. II - thrust force and torque of HSS Twist drill with external cutting fluid supply.

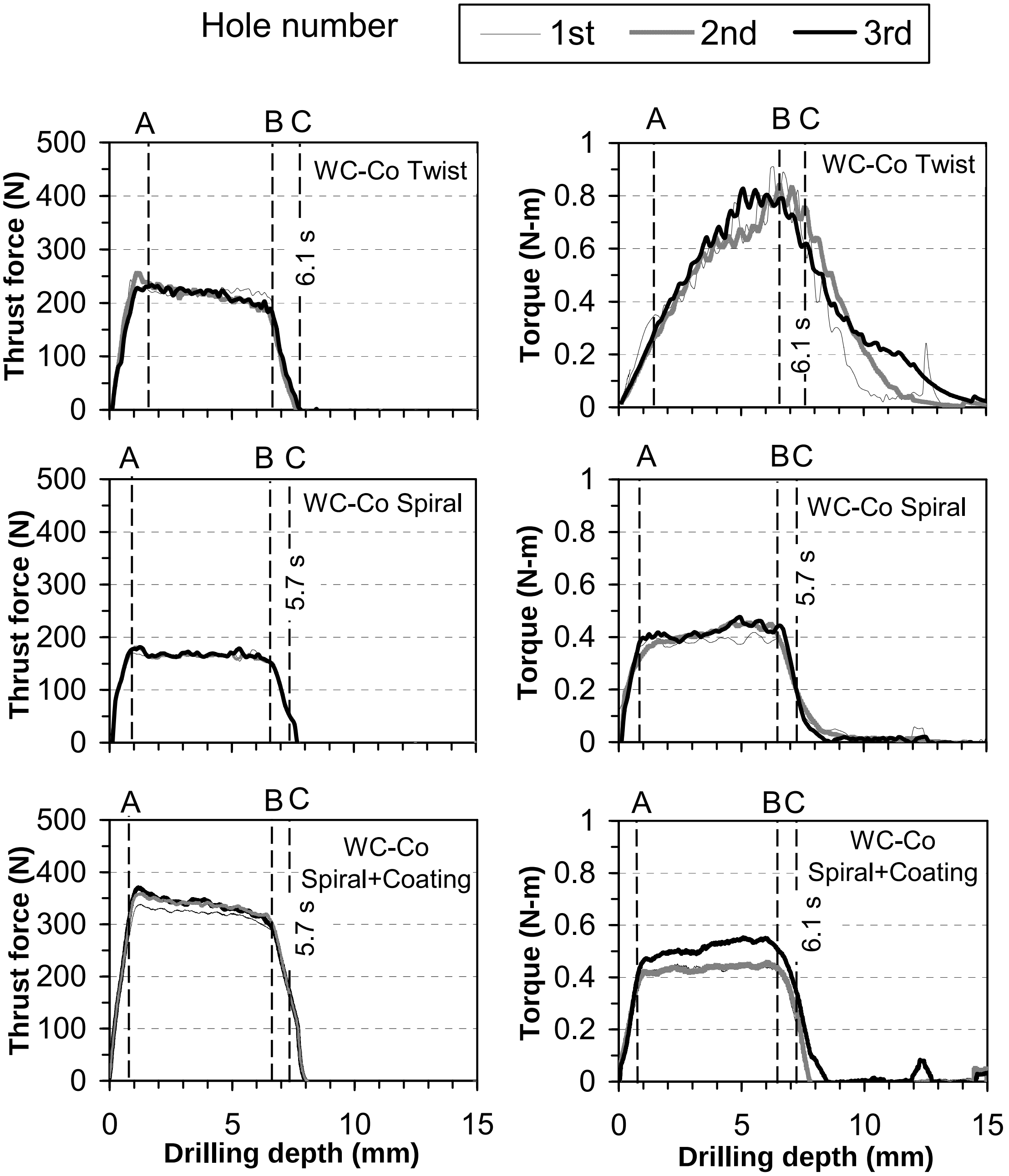

Figure 2.5. Exp. III - Thrust force and torque of WC-Co Twist, WC-Co Spiral and WC-Co Spiral+Coating at 18.3 m/min peripheral cutting speed (1470 rpm).

By comparing with the results of HSS Twist under the same drilling condition in Figure 2.3, the advantage of drill material can be identified. The WC-Co Spiral drill had the lowest thrust force and torque among all four drills used in this paper. The torque curve for WC-Co Spiral drill is particularly stable, maintaining at 0.4 N-m after Stage A. The chip ejection was not a problem for WC-Co Spiral drill at this cutting speed. In comparison, the torque for WC-Co Twist drill continuously increased from about 0.3 N-m in Stage A to 0.8 N-m in Stage B. The torque for WC-Co Spiral+Coating is in the range of 0.37-0.57 N-m. As shown in Table 2.1, comparing to the WC-Co Twist and WC-Co Spiral+Coating drills, the WC-Co Spiral drill also had lower thrust force (166–181 vs. 233–257 N and 293-360 N) and energy (351–375 vs. 603–628 J and 358-407 J). For the HSS Twist drill, compared to the WC-Co Twist drill, the first hole needed much higher thrust force (390 N) and about the same peak torque (0.8 N-m). This shows the benefit of web-thinning to reduce the thrust force in drill geometry design.

Burr formation is another advantage of the WC-Co Spiral drill. Exit burr in Ti drilling is a problem and has been studied (Sakurai, et al., 1992; Dornfeld, et al., 1999). Figure 2.6 shows pictures of the exit burr formation of HSS Twist, WC-Co Twist, and WC-Co Spiral drills at 18.3 m/min peripheral cutting speed and 0.051 mm/rev feed. WC-Co Spiral + Coating drill generated a similar burr as WC-Co Spiral drill. Due to the low thrust force in the S-shaped web, the short drill point length, and large point angle of WC-Co Spiral drill, a cap was formed between Stages B and C at the exit. As a result of the efficient cutting on the periphery of the cutting edge as the drill exits the workpiece, the residual burr was very small, compared to the crown and flower-like exit burr generated by the HSS Twist and WC-Co Twist drills, respectively.

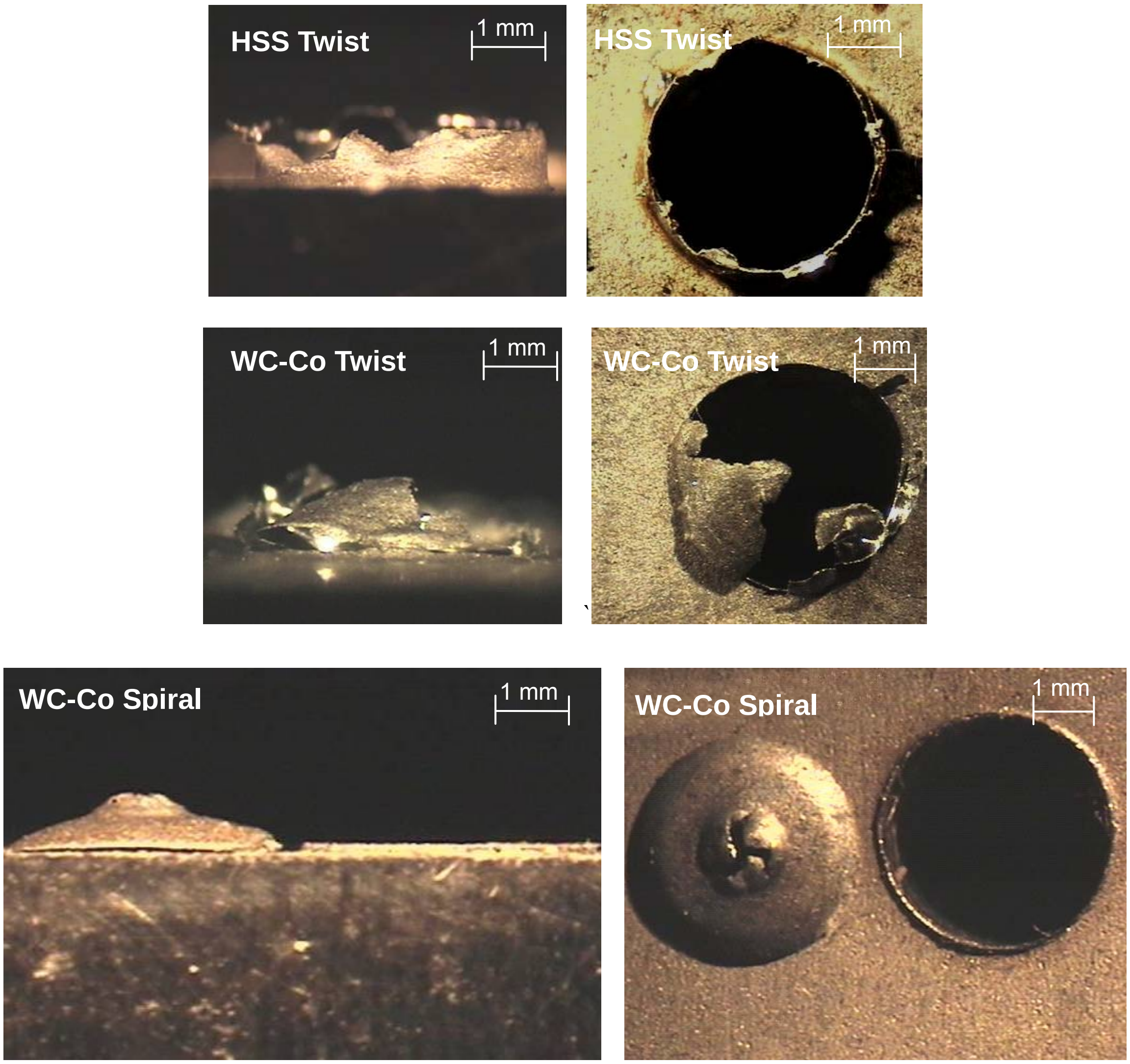
HSS Twist
1 mm
HSS Twist
1 mm
WC-Co Twist
1 mm
WC-Co Twist
1 mm
WC-Co Spiral
1 mm
WC-Co Spiral
1 mm

Figure 2.6. Burr formation of three types of drill at 18.3 m/min peripheral cutting speed (1470 rpm).

2.5. WC-Co Spiral Point Drill High Throughput Drilling – Effect of Cutting Fluid Supply (Exp. IV)

The WC-Co Spiral drill was selected for high throughput Ti drilling. At a constant feed (0.051 mm/rev), tests were conducted by gradually increasing the drill rotational speed. The drill could perform at 183 m/min peripheral cutting speed (14700 rpm) under dry drilling. At this high speed, the feed rate was also high, 0.75 m/min, which was more than 5 times the value commonly used in industrial practice (Machining Data Handbook, 1980). It took only 0.57 s at 156 mm^3/s MRR to drill a through hole in the 6.35 mm thick Ti plate.

2.5.1. Dry Drilling

As shown in the summary of drill life in Table 2.1, under dry condition, the WC-Co Spiral drill lasted about 10 holes at 183 m/min peripheral cutting speed and 0.051 mm/rev feed. Figure 2.7 shows the thrust force and torque before drill breakage in dry drilling.

The thrust force was about 150–200 N after Stage A. This was the same level of thrust force for the same drill at 18.3 m/min cutting speed, as shown in Figure 2.5. The torque started to peak after Stage B, as a result of difficulty in chip ejection due to the chip welding to the drill. The same phenomenon was observed in HSS Twist drill at 13.7 m/min cutting speed, as shown in Figure 2.3. A significant increase in torque (T_m increased by about 30%) but not the thrust force was observed in the last hole before the drill broke catastrophically during drilling. It indicated that the wear was concentrated on the periphery of the cutting edges, which had been confirmed by visual observation of this drill wear pattern during the test.

2.5.2. Drilling with External Cutting Fluid Supply

Using external flood cutting fluid supply, the drill life only increased slightly to about 14 holes under the same cutting speed and feed as in dry drilling. The high drill rotational speed generated high centrifugal force and prevented the cutting fluid from reaching the cutting region. As shown in Figure 2.7, the thrust force and torque have similar values and patterns as in dry drilling. The increase in torque near the end of drilling also exists. This is another indication that the externally supplied cutting fluid did not help drilling at high speed. The chip ejection continued to be a problem for drilling with external cutting fluid supply.

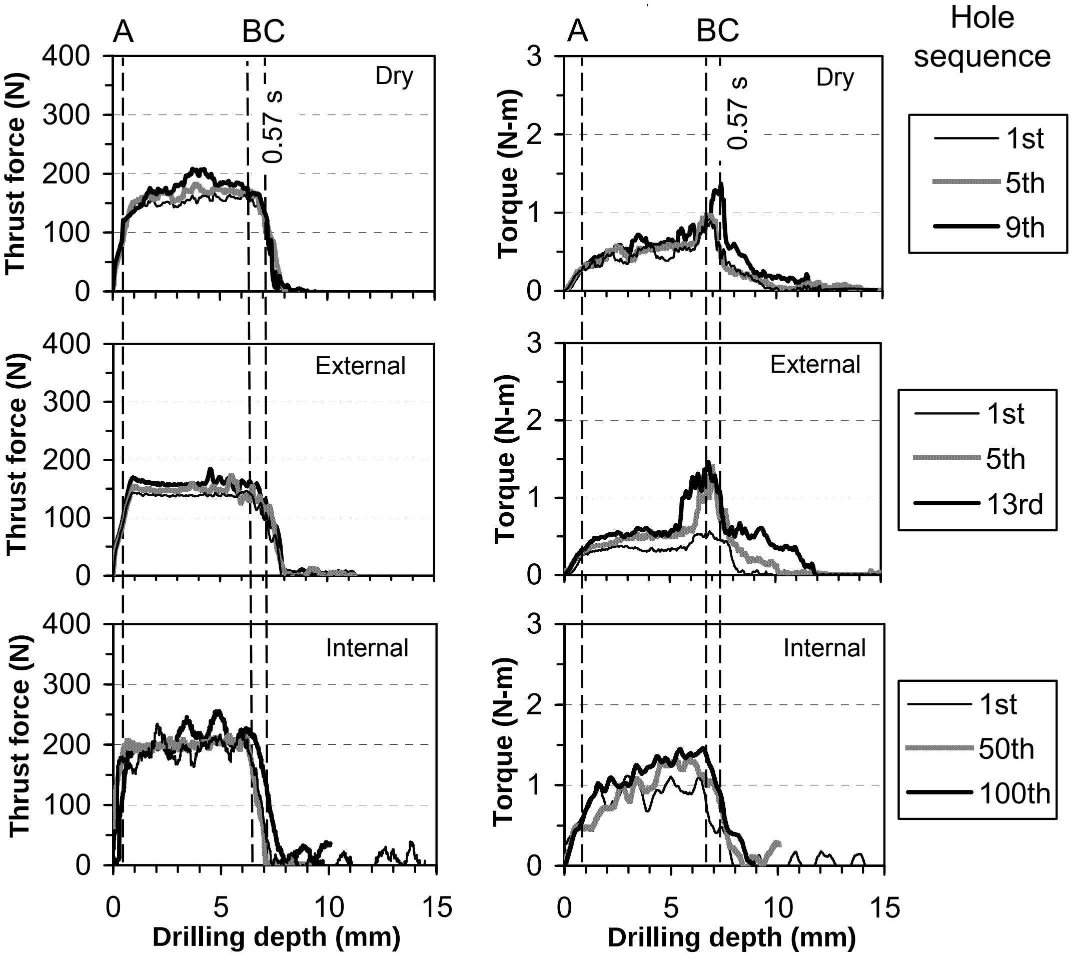

Figure 2.7. Exp. IV - thrust force and torque of WC-Co Spiral drill for high throughput drilling at 183 m/min peripheral cutting speed and 0.051 mm/rev feed under the dry and internal and external cutting fluid supply conditions.

2.5.3. Drilling with Internal Cutting Fluid Supply

The internal cutting fluid supply significantly increased the drilling life to 101 holes at the 183 m/min cutting speed and 0.051 mm/rev feed. The internal cutting fluid supplied through machine spindle and drill could go directly to the tool-chip interface for effective cooling, lubrication, and, more importantly, assistance of chip ejection. The torque curve does not have the high peak between Stages B and C. The peak torque ranged from 1.02 to 1.48 N-m and was located before reaching Stage B. The thrust force was slightly higher, about 200–240 N, likely caused by the hydrodynamic force. As shown in the energy *E* in Table 2.1, drilling with internal cutting fluid supply required more energy (762–995 J vs. 497–709 J for dry and 504–574 J for external fluid supply) because of the more uniform torque curve after Stage A.

2.6. WC-Co Spiral High Throughput Drilling – Effect of Feed (Exp. V)

While maintaining the same MRR (156 mm^3/s) as drilling under 183 m/min cutting speed and 0.051 mm/rev feed in Exp. IV, the feed was increased to 0.076, 0.102, and 0.152 mm/rev, which, as shown in Table 2.1, matched with the 122, 91, and 61 mm/rev feed and 153, 205, and 164 holes drill life, respectively. The time required to penetrate the 6.35 mm Ti-6Al-4V plate, 0.57 s, was the same as in Exp. VI. The best drill life of 205 holes was achieved at 91 m/min cutting speed and 0.102 mm/rev feed which is larger than the recommended feed for Ti drilling.

Adjusting the feed has a significant impact on drill life. Feed is a process parameter which has been overlooked by drilling researchers. Using the conventional twist drill, the range of feed is limited. For the 4 mm drill, the recommended feed is 0.051 mm/rev. Advanced spiral point drill geometry design and new tool material enable the drill to take a higher cutting force and feed. As shown Figs. 2.7 and 2.8, as the feed increases from 0.051 to 0.076 mm/rev, the thrust force stays at about 200 N. Increasing the feed to 0.102 mm/rev only raised the thrust force to about 260 N for the new drill and 330 N at the end of drill life (205 holes). New drill geometry design can withstand such increase in cutting forces. The lower cutting speed at higher feed helps to reduce the drill temperature, which is beneficial to the drill life.

This study also found that there was a limit of drill life associated with the increase of feed. As the feed increased to 0.152 mm/rev, the drill life (164 holes) started to reduce due to the high cutting force. In summary, Exp. V leads to the conclusion that feed is an important process parameter in high throughput drilling of Ti. The suggested values for feed are low for advanced drill design to achieve optimal drill life.

The drill which had good drill life also produced holes with low surface roughness. Figure 2.9 shows the hole surface roughness vs. drill life (number of holes) for high throughput drilling tests in Exps. VI and V. All tests had the same MRR, 156 mm^3/s. The range of upper and lower surface roughness of the first three holes is presented. In Exp. IV, the internal cutting fluid supply helped to improve the surface finish. Combined data in Exps. IV and V shows the long drill life positively correlates to the good initial hole surface finish.

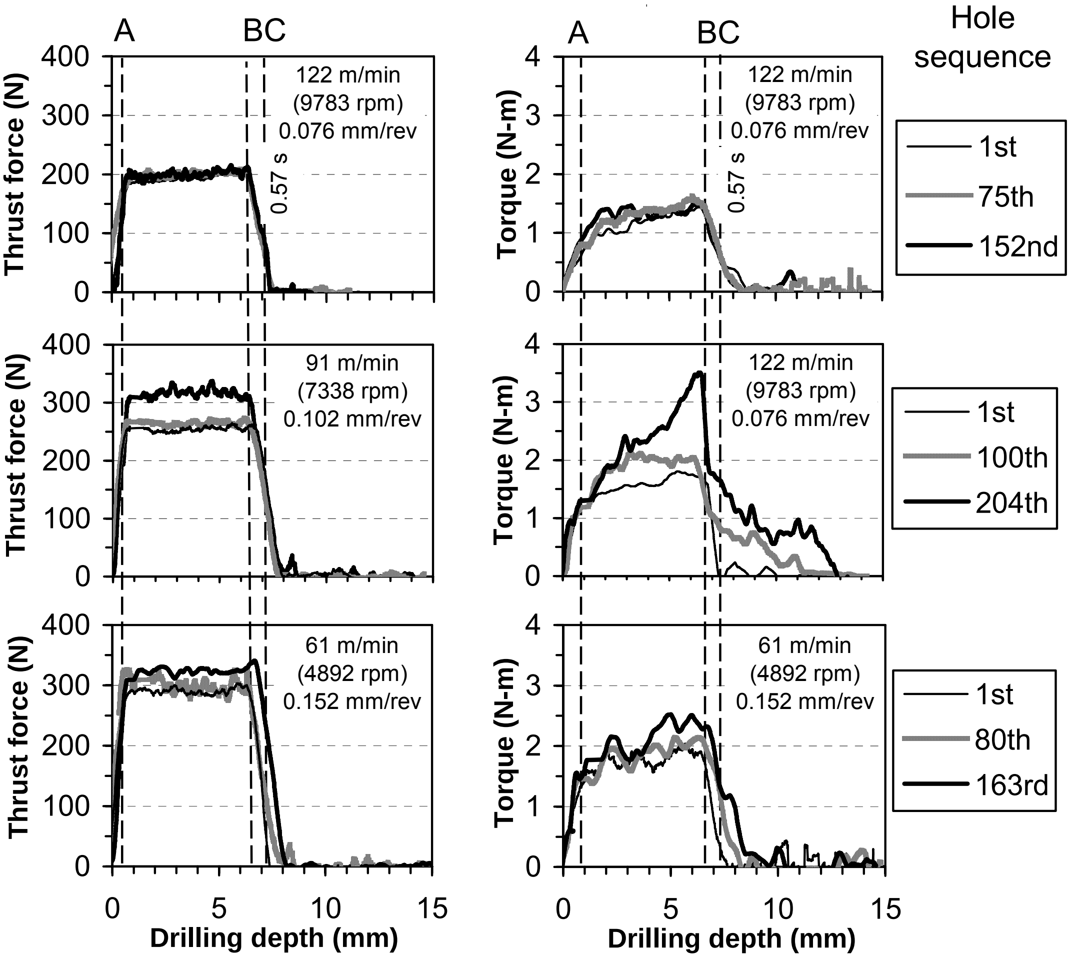

Figure 2.8. Exp. V - thrust force and torque of WC-Co Spiral drill for high throughput drilling at 0.75 m/min feed rate and 156 mm3/s material removal rate with internal cutting fluid supply.

2.7. Light Emission in Chip Formation and Chip Morphology

Chip light emission or sparks could be observed in some Ti drilling tests. Due to the low thermal conductivity of Ti, the chip temperature is high and subsequently creates oxidation or burning (Cantero, 2005; Bakkal, 2004; Bakkal, 2005). For HSS Twist drill, the chip light emission was observed at 13.7 and 27.4 m/min cutting speed for drilling under dry and external cutting fluid supply condition, respectively.

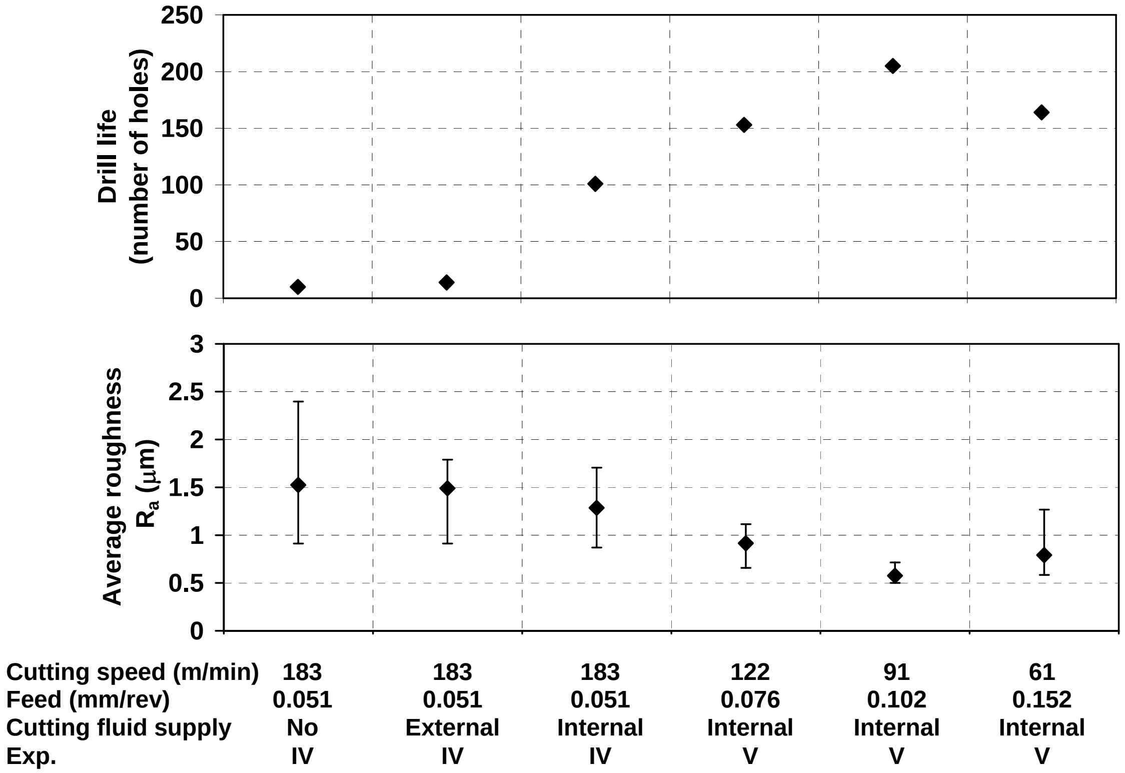

Figure 2.9. Hole surface roughness under high throughput drilling with the same material removal rate (156 mm^3/s) using WC-Co Spiral drill in Exp. VI and V.

For WC-Co Spiral drilling at 0.051 mm/rev feed, no light emission occurred at cutting speed below 82.3 m/min. For the same WC-Co Spiral at 183 m/min cutting speed and 0.051 mm/rev feed, chips sparked in almost every hole drilled in dry drilling and drilling with external cutting fluid supply. When the cutting fluid was supplied internally through the drill at the same cutting speed and feed, no chip light emission could be observed initially. In the 80th hole (out of 101 holes drilled), when the drill wear reached a level, the chip light emission started to occur. For three drilling conditions in Exp. V, the chip light emission occurred in the 120th, 125th, and 140th hole at 122, 91, and 61 m/min cutting speed, respectively. This shows that for drilling at the highest and lowest feed under the same MRR in Exp. V, the drill failed quickly after the start of chip light emission. This light emission was usually associated with the chip welding, which could be identified by the difficulty to remove the chip in the flute near the drill tip.

After drilling, the Ti chip could be entangled around two flutes of the drill and bend by the tool holder. This is called chip entanglement, which is due to the difficulty for smooth chip ejection. Chip entanglement occurred in all tests except the drilling with internal cutting fluid supply before the drill wear reached a threshold level. In Exps. IV and V with internal cutting fluid supply, chip entanglement occurred after the 95th, 130th, 150th, and 150th hole at 183, 122, 91, and 61 m/min cutting speed, respectively.

The same chip morphology, a continuous chip with three regions of initial spiral cone followed by the steady-state spiral cone and folded long ribbon chip, could be seen in all Ti drilling tests in this study. An example of the chip generated by WC-Co Spiral drill at 18.3 m/min cutting speed and 0.051 mm/rev feed in dry drilling is shown in Figure 2.10(a). The close-up view of the initial spiral cone, generated at the start of drilling from the beginning of contact to Stage A, is illustrated in Figure 2.10(b). After Stage A, the steady-state spiral cone chip morphology, as shown in Figure 2.10(c), was generated. Due to the increased resistance to eject the chip, the spiral cone was changed to folded ribbon chip morphology. Close-up view of the chip transition region and the folded ribbon chip are shown in Figs 2.10(d) and (e), respectively.

The length of spiral cone chip can be considered as a scale to evaluate the difficulty for chip evacuation in drilling. As shown in Table 2.1, for HSS Twist drill, the chip length of spiral cone was about 12–35 and 14–24 mm in dry drilling and drilling with cutting fluid, respectively. At high cutting speed, the chip was generated at a high rate, the chip ejection was more difficult, the transition from steady-state spiral cone to folded long ribbon chip occurred early, and the length of spiral cone was short.

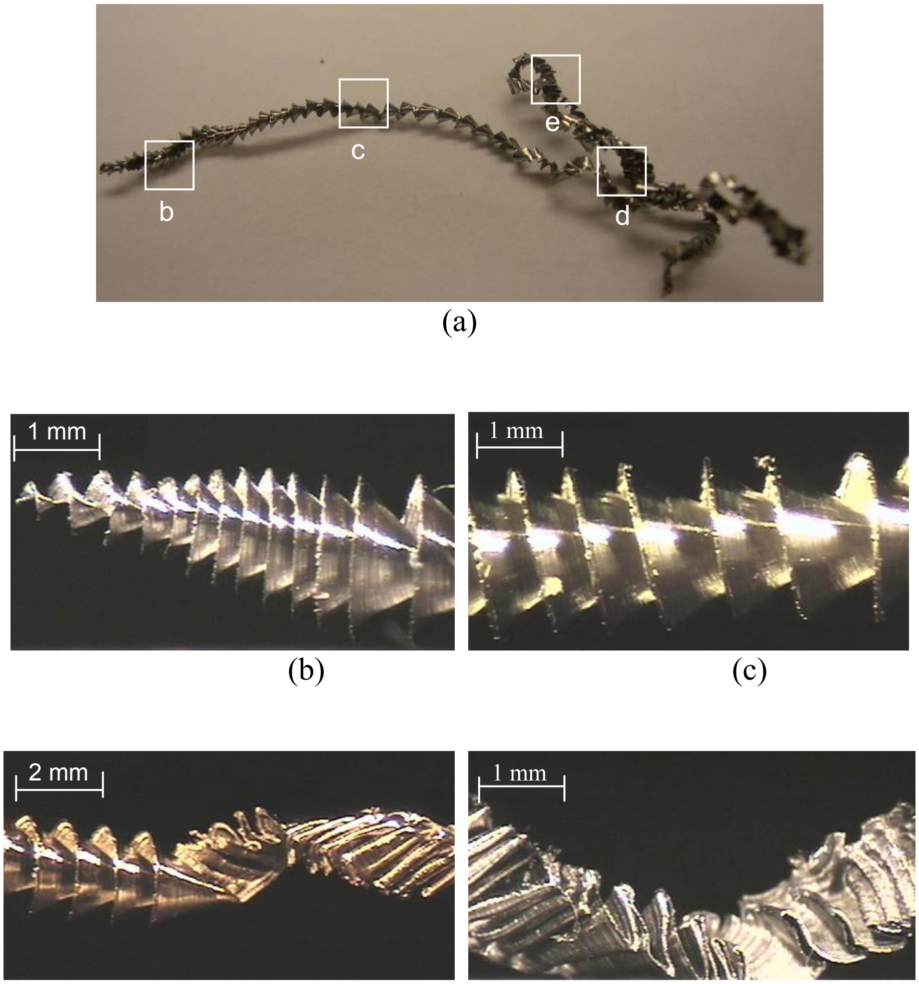

(a)

(b) (c)

(d) (e)

Figure 2.10. Chip morphology of Ti-6Al-4V generated by WC-Co Spiral drill at 18.3 m/min cutting speed and 0.051 mm/rev feed in dry drilling: (a) whole chip, (b) initial spiral cone (c) steady-state spiral cone, (d) transition between spiral cone and folded long ribbon, and (e) steady-state folded long ribbon.

In dry drilling using WC-Co Spiral drill, the length of spiral cone chip decreased from 48–54 to 0–5 mm when the cutting speed increased from 18.3 and 183 m/min. At 183 m/min cutting speed, the use of internal cutting fluid supply could assist the chip ejection and increase the length of spiral cone chip to 18–25 mm. In Exp. V, at the same MRR, the drilling condition with the longest drill life also had the longest spiral cone chip length, indicating the improved chip ejection under such drilling condition.

2.8. Tool Wear

SEM micrographs of the progressive wear of a WC-Co Spiral drill for high throughput drilling at 61 m/min cutting speed and 0.152 mm/rev feed with internal cutting fluid supply in Exp. V are presented in Figure 2.11. The drill was removed from the machine and examined after drilling 25, 100, and 164 holes. The drill broke in the drill body while drilling the 164th hole and left the drill tip in the workpiece. It enabled the observation of the drill wear at the end of drill life. The same mode of drill breakage was observed in all high throughput Ti drilling tests using WC-Co Spiral drills.

Four SEM micrographs, the overview of drill point and the close-up views of the chisel edge, middle of cutting edge, and intersection of the margin and cutting edge, as shown by boxes in the overview of the drill tip, are presented after drilling 25, 100, and 164 holes. After drilling 25 holes, minimal drill wear could be recognized. The chisel edge was sharp with slight work-material buildup. The middle of cutting had slight material buildup, as marked by A2. Relatively more significant, but not severe, material buildup was observed at the intersection of cutting edge near the margin due to the relatively high cutting speed in this area.

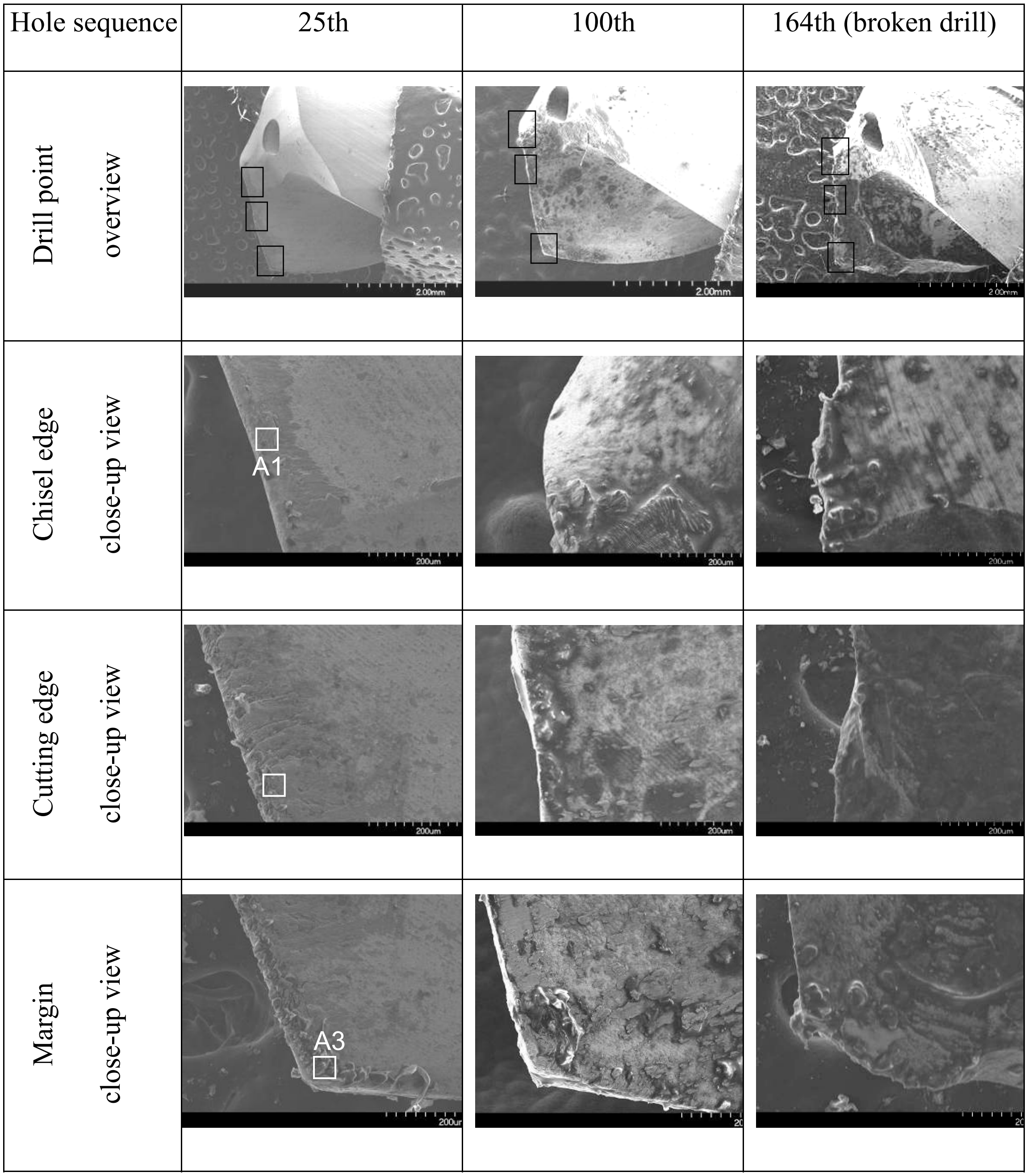
Hole sequence
25th
100th
164th (broken drill)
Drill point overview
Chisel edge close-up view
Cutting edge close-up view
Margin close-up view
A1
A3
2.00mm
200um

Figure 2.11. SEM micrographs of tool wear of the WC-Co Spiral drill at 61 m/min cutting speed and 0.152 mm/rev feed with internal cutting fluid supply.

The EDS x-ray of areas A1, A2, and A3 showed identical outcome in elemental analysis. It had Ti, Al, and V, the composition of the Ti-6Al-4V alloy, which indicated the adhesion of work-material on the drill. It also had W and C, the composition of the tool material, and O, representing the oxidation at high drilling temperatures.

After drilling 100 holes, as shown in Figure 2.11, the tool wear was obvious. On the chisel edge, residual Ti work-material buildup on the surface became more apparent. Similar material buildup was observed in the middle and outside corner of the cutting edge. The corner of the drill margin and cutting edge remained sharp, indicating the drill was still capable of effective drilling.

The drill tip at the time of drill breakage at 164 holes was not melted but had fractured significantly. Close-up views show that the chisel edge and middle cutting edge were both fractured. The corner of drill margin and cutting edge was also severely fractured and no longer sharp. The drill had lost the shape for effective drilling. The cutting forces were expected to be high and a broken drill was expected.

2.9. Concluding Remarks

This study demonstrated the feasibility of high throughput drilling of Ti-6Al-4V and the importance of feed and internal cutting fluid supply to improve the drill life. High MRR of 156 mm^3/s with peripheral cutting speed up to 183 m/min was achieved using a commercially available 4 mm diameter WC-Co spiral point drill. In comparison, a conventional HSS twist drill could only work below 27.4 m/min cutting speed and 23.3 mm^3/s MRR. The spiral point drill design showed advantages of low thrust force, torque, energy, and burr size. The balance of cutting speed and feed was demonstrated to be critical in high throughput drilling of Ti. Under the same MRR (156 mm^3/s), the best drill life and surface finish results were achieved at 91 m/min peripheral cutting speed and 0.102 mm/rev feed using the WC-Co spiral point drill.

The internal cutting fluid supply through the drill at 0.2 MPa was critical for long drill life. It also helped to improve the chip ejection, as demonstrated by the increased length of steady-state spiral cone chip region. As a future research work, high pressure fluid delivery systems (Arai and Ogawa, 1997) may further improve the tool life for high throughput drilling of Ti. Chip light emission in high throughput drilling of Ti was observed. It was particularly prominent for the worn drill.

Modeling of the drilling process based on the finite element method (Strenkowski, et al., 2004) is an important research direction to understand the work-material deformation and temperature distribution in high throughput drilling. Drilling tests in this study were time consuming and expensive. Drilling process modeling can potentially narrow the range of experiments carried out and reduce the time and effort required to find optimal drilling process conditions.

CHPATER 3

SPIRAL POINT DRILL TEMPERATURE AND STRESS IN HIGH-THROUGHPUT DRILLING OF TI

The spatial and temporal distributions of the temperature and stress of a 9.92 mm diameter spiral point drill are studied in high-throughput drilling of Ti-6Al-4V with 384 mm^3/s material removal rate (MRR). A finite element thermal model using the inverse heat transfer method is applied to find the heat partition on the tool-chip contact area and convection heat transfer coefficient of cutting fluid. In this model, the chisel and cutting edges of a spiral point drill are treated as a series of elementary cutting tools. Using the oblique cutting analysis of the measured thrust force and torque, the forces and frictional heat generation on elementary cutting tools are calculated. Temperatures measured by thermocouples embedded on the drill flank face are used as the input for the inverse heat transfer analysis to calculate the heat partition factor between the drill and chip. The temperature distribution of the drill is solved by the finite element method and validated by experimental measurements with good agreement. Thermo-mechanical finite element analysis is applied to solve the drill stress distribution.

Modeling results confirm that the supply of cutting fluid is important to reduce the temperature across the drill cutting and chisel edges. At 183 m/min peripheral cutting speed, 0.05 mm/rev feed and 10.2 mm depth of drilling, the drill peak temperature is reduced from 1210°C in dry drilling to 651°C with cutting fluid supplied through the drill body. Under the same MRR, 61 m/min peripheral cutting speed and 0.15 mm/rev feed, the analysis shows that the drill peak temperature is reduced to 472°C. The temperature induced thermal stress combined with the mechanical stress caused by cutting forces is analyzed to predict the location of drill failure. Applying the modified Mohr failure criterion, the drill cutting and chisel edges are found to be prone to failure in dry and wet drilling conditions, respectively. This study demonstrates the effectiveness of drill thermal and stress modeling for drilling process parameter selection and drill design improvement.

3.1. Introduction

A major technical challenge in machining titanium (Ti) and Ti alloys is the high tool temperature. The inherent material properties, particularly the low thermal conductivity, of Ti and its alloys is the primary cause (Yang and Liu, 1999; Rahman et al., 2003). High tool temperature softens the tool material and is detrimental to the tool life. For drilling, since the tool is constrained in a hole, the temperature is significantly high in the drill tip. This results in the limited MRR and, subsequently, low productivity and high cost in machining Ti.

The research in high-throughput Ti drilling experiments has demonstrated that advanced tool geometry design and proper process parameter selection can achieve high

MRR with satisfactory tool life (Li and Shih, 2007a). It is known that the supply of cutting fluid and the selection of feed and cutting speed in drilling greatly affect drill temperature, stress, and life in Ti drilling (Li and Shih, 2007a). The goal of this study is to study the detailed drill temperature distribution and understand the effect of cutting speed in Ti drilling and quantify the spatial and temporal drill temperature and stress distributions in high-throughput drilling of Ti-6Al-4V, a commonly used Ti alloy.

Several methods have been developed to experimentally measure the drill temperature (Stephenson and Agapiou, 2006). A common method is to embed insulated wires in the workpiece to form the hot junction of a tool-work thermocouple (Tueda et al., 1961; Watanabe et al., 1977; Agapiou and Stephenson, 1994; Arai and Ogawa, 1997). The thermocouple electromotive force (emf) generated when the tool cuts is recorded through the wire and is used to detect the drill temperature. This method has good repeatability and time response, but can only measure temperatures at discrete points in low-speed drilling due to the short contact period. Using an embedded foil tool-work thermocouple overcomes these problems by replacing the embedded wires with a metallic foil. It can measure the tool temperature across the cutting edge (Bono and Ni, 2002). For metallic workpiece, the foil must be electrically isolated from the workpiece with insulating materials, but this multi-layer setup changes the drilling condition and the delamination between different layers becomes a problem. In drilling Ti, the cutting temperature is over 1000°C, which can melt the plastic insulating materials. Other disadvantages of the tool-work thermocouple methods are the requirement of extensive calibration work and limitation to dry drilling because cutting fluid can influence the contact between the drill tip and metallic wire or foil. Commercial thermocouples can also be embedded in the drill to measure the temperature (Agapiou and Stephenson, 1994; Devires, et al., 1967; Bono and Ni, 2001; Bagaci and Ozcelik, 2006). It requires careful specimen preparation to avoid damaging the thermocouple during drilling. Thermocouples can only measure temperature at discrete points away from the cutting edge. Since the tool and work-materials are subject to high temperature and undergo hardness change, metallurgical transformation, or even chemical composition change, the micro-hardness measurement (Thangaraj et al., 1984), scanning electron microscopy (Mills et al., 1981), and energy dispersive x-ray measurement (Reissig et al., 2004) have been developed to measure the drill temperature. Similarly, drills coated with thermo-sensitive paints can be utilized for temperature measurement (Tueda et al., 1961; Koch and Levi, 1971). A common disadvantage of these methods is that they only measure the peak temperature. Also, these methods require extensive post-test sample preparation and analysis. The infrared thermal camera is not suitable for drill temperature measurement because the drill cutting region is embedded inside the workpiece.

Because the heat generation rate and drill temperature distribution during Ti drilling are difficult to measure directly, numerical modeling becomes an important tool to study the drill temperature. Agapiou and Stephenson (1994) have reviewed the early analytical modeling of temperature distribution in the drill, which is represented as a semi-infinite body. The empirical force equations from a series of turning (oblique cutting) tests were used to calculate heat source and a transient heat transfer analysis was carried out to calculate the heat partition (Agapiou and Stephenson, 1994). On the analysis of drill as a finite domain, Saxena et al. (1971) and Watanabe et al. (1977) have applied the finite difference method. More recently, finite element method has been applied by Fuh (1987), Chen (1996), and Bono and Ni (2001, 2006) for the drill temperature analysis. These studies showed limitations in accurate prediction of drill temperature. The inverse heat transfer modeling using measured force, torque, and drill temperature as the inputs is developed to improve the accuracy in predicting the drill temperature distribution for Ti drilling.

By using the idea to divide the drill cutting edges into segments called elementary cutting tool (ECT) (Watson, 1985; Wang, 1994), Ke (2003) has developed the approach to extract the forces data acting on each ECT, which works like an oblique cutting tool during drilling. At the start of drilling, one ECT after another in the drill chisel and cutting edges gradually engages into the cutting action from center of the drill. Using measured thrust force and torque at the start of drilling, cutting forces in each ECT can be calculated. The chip thickness and shear angle associated with each ECT can be measured from the machined chip to estimate the chip speed. Based on this cutting data, the frictional force and heat generation can be determined. A heat partition factor is required to find the amount of heat transferred to the drill for thermal finite element analysis. This heat partition between the drill and chip is recognized as an important, but difficult, parameter to determine. Earlier studies used a constant value for heat partition along the tool-chip interface (Agapiou and Stephenson, 1994; Saxena et al., 1971; Watanabe et al., 1977; Fuh 1994). Variable heat partition factor depending on the cutting speed (Berliner and Krainov, 1991) has later been adopted by Bono and Ni (2001) for drilling temperature prediction. More advanced modeling of variable heat partition (Huang and Liang, 2005; Karpet and Ozel, 2005) in the sticking and sliding contact regions has been studied for two-dimensional orthogonal cutting. Due to the short length of contact region (Machado and Wallbank, 2000) relative to the characteristic size of finite elements and the lack of basic machining data of Ti to determine the model parameters, the variable heat partition in the contact regions is not used. In this study, the cutting speed dependent heat partition model (Berliner and Krainov, 1991) is adopted for drill temperature prediction.

Inverse heat transfer utilizes the temperature measured by thermocouples embedded on the drill flank surface as the input to predict the heat flux on the drill chisel and cutting edges. This model estimates the cutting edge heat generation rate by minimizing the discrepancy between the measured and predicted temperature at the thermocouple locations. In the dry drilling of CP Ti, thermocouples are routed from the frank surface, via through-the-drill coolant holes, to outside the tool (Agapiou and Stephenson, 1994). This setup is adequate for dry drilling but not suitable for the high-throughput drilling of Ti because of the need to use cutting fluid and the interference of cutting fluid with thermocouple wires in through-the-drill holes. In this study, shallow grooves were ground on the side (margin surface) of the drill body to guide the thermocouple wires from the drill tip to outside of a stationary drill. A validation process can be performed by comparing the drill temperature analyzed by finite element analysis to thermocouple measurements not used for inverse heat transfer analysis.

Most of the drill thermal analyses by previous researchers were conducted under the dry condition. In drilling with a supply of cutting fluid, so called wet drilling, the research on drill temperature is limited. Arai and Ogawa (Arai and Ogawa, 1997) measured drill temperature using the embedded wire tool-work thermocouple method in drilling Ti-6Al-4V with an external cutting fluid supply. Kalidas et al. (2002) modeled the workpiece temperature in drilling cast aluminum (Al) 356 with an external cutting fluid supply. Due to the high temperature in Ti drilling, supplying the cutting fluid via through-the-drill holes is necessary to enhance the drill life (Li and Shih, 2007a). To the best of our knowledge, no research publication is available on the analysis of spatial and temporal drill temperature distributions with an internal cutting fluid supply. This research is aimed to fill this gap. In this paper, the spatial and temporal drill temperature distribution in high-throughput (384 mm^3/s MRR) drilling of Ti-6Al-4V with an internal cutting fluid supply is studied using the inverse heat transfer method.

The drill temperature and cutting forces can be used as inputs to analyze the spatial and temporal distributions of the drill stress. For high-throughput Ti drilling, the drill temperatures and forces are both very high. Severe deformation and highly localized stresses are expected in the drill and will eventually lead to the drill failure. The drill deformation has been studied by Bono and Ni (2001) using a finite element model for drilling Al 319. The stress distribution in the drill has also been investigated both experimentally (Law et al., 1972) and numerically (Hinds and Treanor, 2000). This study conducts more in-depth drill stress analysis using the thermo-mechanical finite element model and predicts the initial failure location in a spiral point drill. The von Mises stress of the drill used in high-throughput drilling of Ti-6Al-4V has been presented in (Li and Shih, 2007b). For the WC-Co tool material, the brittle fracture is different from the failure of ductile metals predicted using the von Mises failure criterion (Paul and Mirandy, 1976; Usui et al., 1979; Takagi and Shaw, 1981). More advanced analysis of WC-Co at microstructure level has been conducted (Chernvavskii, et al., 1993; Park et al., 2006). In this paper, three most frequently used brittle failure criteria, Rankine, Mohr-Coulomb

(Chen and Han, 1988), and modified Mohr criteria (Barber, 2001), are compared to select the most suitable failure criterion for drilling. The location in the drill likely to initiate the failure is identified in the analysis.

In this section, the experimental setup of Ti drilling tests and drill temperature measurements is first introduced in Sec. 3.2. The drill solid modeling, elementary cutting tools, finite element thermal model, oblique cutting mechanics in ECT, calculation of heat generation rate, and inverse heat transfer analysis are discussed in Sec. 3.3. The drill temperature measurement and validation are presented. Finally, the drill stress, deformation, and failure analyses are performed.

3.2. Experimental Setup and Design

The high-throughput drilling tests of Ti-6Al-4V were conducted with the similar setup as dry drilling tests of CP Ti. Figure 3.1(a) shows the experimental setup with a rotating 25 mm diameter Ti-6Al-4V bar and a stationary 9.92 mm diameter spiral point drill (Kennametal K285A03906). Two fluid jets, under 0.2 MPa pressure, can be identified shooting from the drill body. As shown in Figure 3.1(b), the tips of 0.127 mm diameter thermocouples (OMEGA 5TC-TT-E-36-72), denoted as TC1 and TC2, are embedded in grooves hand ground on the drill flank face and located close to the cutting edge. An X_T-Y_T coordinate is defined at the center of the S-shaped chisel edge in the spiral point drill. The Y-axis is parallel to the tangent at the apex of the curved cutting edge. Coordinates of the tips of two thermocouples are identified in the Figure 3.1(b). Unlike the setup in dry drilling with thermocouple wires going through holes inside the drill body (Li and Shih, 2006), thermocouple wires in this study were routed up the drill body in hand ground grooves around the drill body surface to avoid the interference with the supply of cutting fluid.

Four drilling experiments, designated as D183, W183, W91, and W61, are listed in Table 3.1. Symbols D and W represent the dry and wet (internal cutting fluid supply) drilling conditions, respectively. The number represents the peripheral cutting speed in m/min. The first experiment, D183 was a dry drilling at 183 m/min peripheral cutting speed and 0.051 mm/rev feed. Using the cutting fluid and maintaining the same material removal rate (384 mm^3/s) and feed rate (4.97 mm/s) as in Exp. D183, three drilling tests, Exps. W183, W91, and W61 were conducted at 183, 91, and 61 m/min peripheral cutting speed and 0.051, 0.102, and 0.152 mm/rev feed, respectively. The depth of drilling was 10.2 mm and the drilling time was 2.0 s in all four experiments.

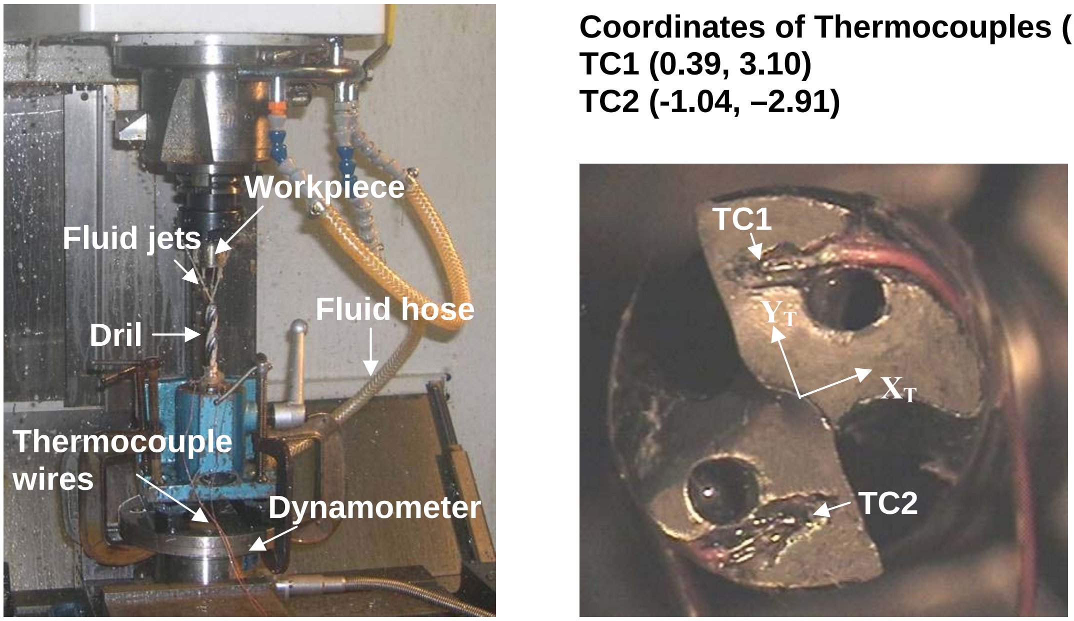

Coordinates of Thermocouples (mm):
TC1 (0.39, 3.10)
TC2 (-1.04, –2.91)

(a) (b)

Figure 3.1. Experimental setup: (a) workpiece, drill, fluid hose, and dynamometer and (b) top view and coordinates of thermocouple tips on drill flank face.

3.3. Spiral Point Drill Geometry and Oblique Cutting Analysis

The solid modeling of the spiral point drill, elementary cutting tools, oblique cutting mechanics in ECT, and calculation of heat generation rate are discussed in the following sections.

Table 3.1. Experiment process parameters for high-throughput drilling of Ti-6Al-4V with 4.97 mm/s feed rate and 384 mm^3/s material removal rate.

Exp.	D183	W183	W91	W61
Cutting fluid supply	Dry	Wet	Wet	Wet
Peripheral cutting speed (m/min)	183	183	91	61
Feed (mm/rev)	0.051	0.051	0.102	0.152

3.3.1. Drill Solid Modeling

The spiral point drill has more complex geometry than the conventional twist drill. To develop 3D finite element mesh for thermal analysis, the solid model of the drill was established in three steps. First, the drill cross-section profile (DCSP) perpendicular to the axis of the drill was measured using an optical tool-maker microscope, as shown in Figure 3.2. Then, a CAD software, SolidWorks^{TM}, was applied to generate the drill body by sweeping the DCSP along a spiral curve with the specified pitch and helix angle. Finally, the trajectory of grinding wheel to generate the spiral drill point with S-shaped chisel edge was simulated to remove unwanted material and create the solid model of drill tip geometry. The drill grinding parameters were provided by Kennametal. Appendix II lists major drill grinding parameters. The solid model of the spiral point drill is illustrated in Figure 3.3. Key parameters of the drill are: 30° helix angle, 135° point angle, 1.9 mm point length, 1.4 mm coolant hole diameter, 52° chisel edge angle, 7° clearance angle at cutting corner, 0.43 mm width of margin, 1.4 mm chisel edge radius, and 1.8 mm chisel edge length. The drill was ground using a grinding wheel with 150 mm diameter and 1.1 mm corner radius.

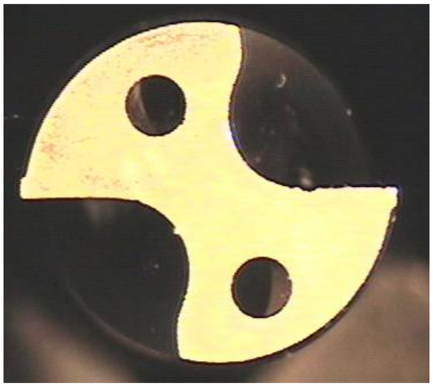

Figure 3.2. The drill cross section profile of the spiral point drill.

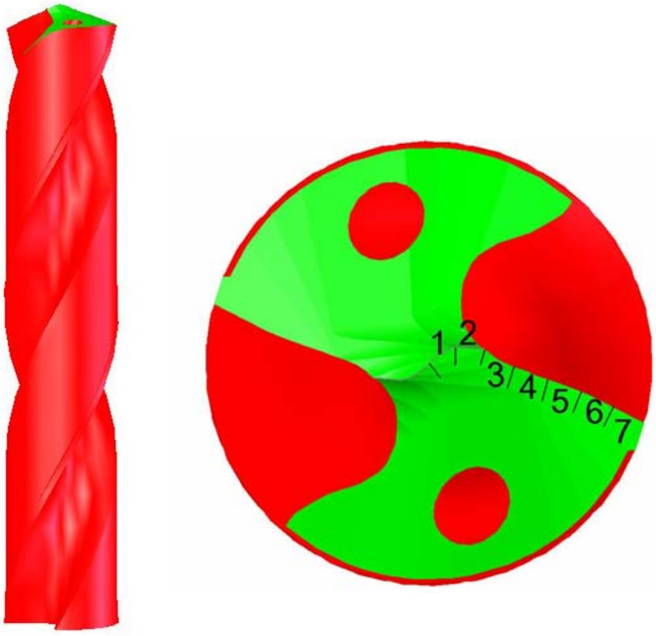

(a) (b)

Figure 3.3. Solid model of the spiral point drill: (a) side view and (b) top view with marked seven ECTs.

3.3.2. Elementary Cutting Tools (ECT)

As shown in Figure 3.3(b), two ECTs are used to represent half of the chisel edge (web of the drill) and five ECTs are used to model the cutting edge. The whole drill point is composed of 14 ECTs. Each ECT has a straight cutting edge. The length of cutting edge of the ECT is 0.71 and 0.85 mm in the chisel and cutting edge, respectively. Figure 3.4 shows the rake angle, inclination angle, and angle between drill axis and ECT cutting edge of the seven ECTs. These angles were obtained from the drill solid model since there is no existing formula to calculate these angles of the spiral point drill. The rake angle in the chisel edge is equal to –29 and –9° for ECT 1 and 2, respectively. Compared to the conventional twist drill with 118° point angle and –59° rake angle (Strenkowski et al., 2004), the spiral point drill has less negative rake angles.

Oblique cutting mechanics is applied to analyze the cutting forces (Bono and Ni, 2001; Strenkowski et al., 2004) in each ECT. Cutting forces in each ECT are obtained from experimentally measured thrust force and torque at the onset of drilling, before the full engagement of the drill tip with the workpiece.

3.3.3. Oblique Cutting Mechanics in ECT

The oblique cutting analysis is utilized to calculate the friction force and chip velocity along the chip flow direction on the ECT rake face. The side view of drill tip partially engaged with the workpiece at the start of contact is shown in Figure 3.5(a). Seven ECTs are marked on the drill tip. Starting from the ECT 1 at drill tip, the ECT sequentially engages with the workpiece at the start of drilling. After the drill is moved a distance equal to the drill point length, 1.9 mm into the workpiece for the drill used in this study, all seven ECTs are engaged with the workpiece, as shown in Figure 3.5(b)

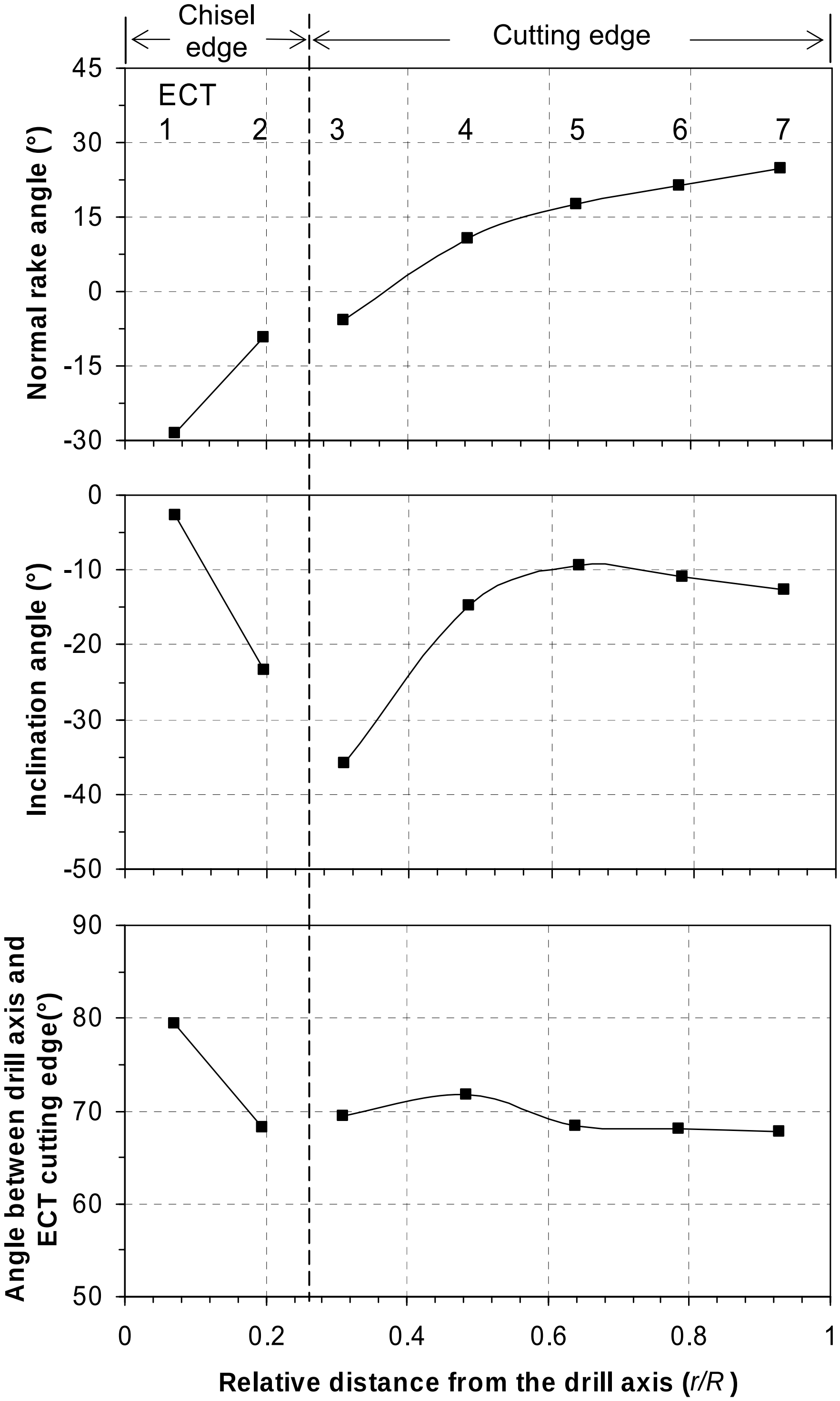

Figure 3.4. The rake angle, inclination angle, and angle between drill axis and ECT cutting edge.

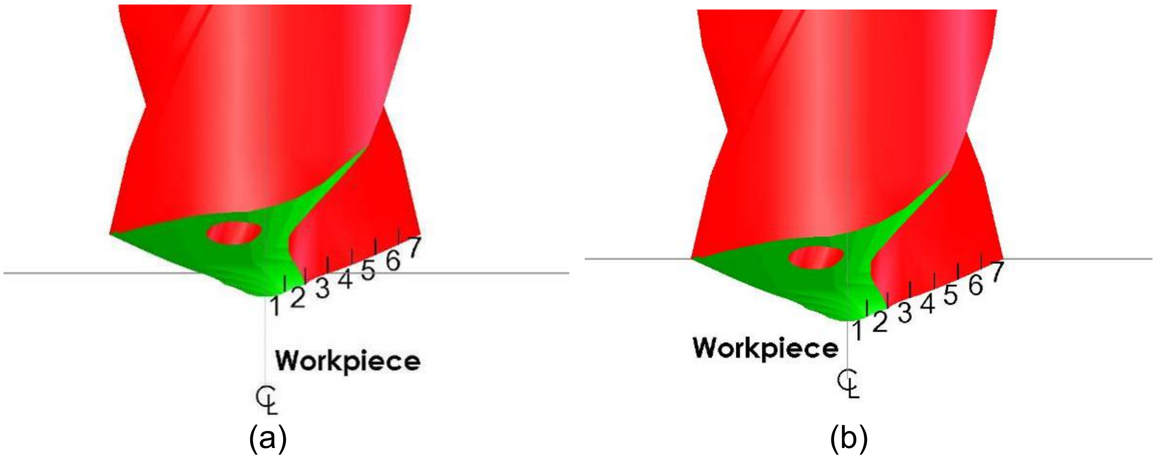

(a) (b)

Figure 3.5. Illustration of two stages in drilling: (a) partial engagement of drill tip with the workpiece (ECT 1, 2, and 3 engaging the workpiece) and (b) full engagement of the tool tip and all seven ECTs with workpiece.

Assuming the thrust force and torque on each ECT do not change and the workpiece does not deform during the drilling, the thrust force and torque contributed by each ECT can be found by identifying the incremental increase of measured thrust force and torque at the time when each of the ECT is fully engaged into the workpiece (Ke, 2003). After the drill tip penetrating the workpiece, i.e., drill penetrating beyond Figure 3.5(b), the thrust force and torque are affected by the contact between chips and drill flute, drill margin and hole, and chips and hole wall. In addition, the change of chip morphology and wear of the drill can also alter the thrust force and torque on ECT. In this research, these effects are neglected.

Figure 3.6 shows the oblique cutting model of an ECT. Five angles: inclination angle λ, normal rake angle α, angle between the drill axis and ECT cutting edge θ, chip flow angle η, and shear angle ϕ are defined According to Stabler's rule (Stabler, 1951), the chip flow angle η is assumed to be equal to the inclination angle λ. The uncut chip thickness and chip thickness are marked as *a* and a_c, respectively.

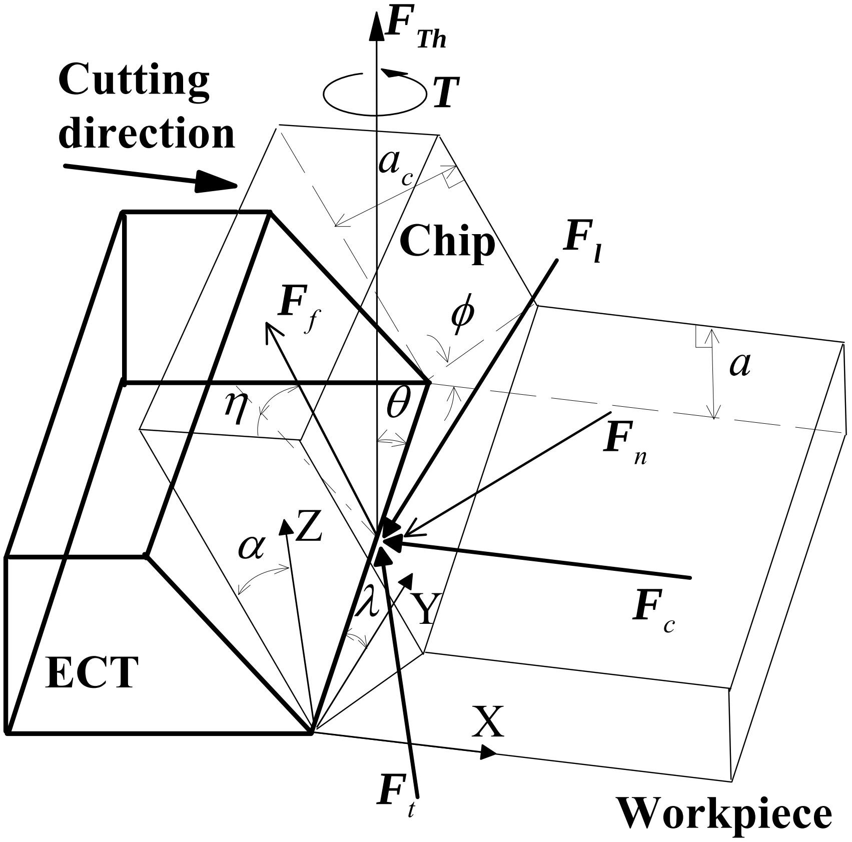

F_{Th}
Cutting direction
T
a_c
Chip
F_l
F_f
ϕ
a
η
θ
F_n
α
Z
λ
Y
F_c
ECT
X
F_t
Workpiece

Figure 3.6. Oblique cutting model of an ECT.

An orthogonal coordinate system with the X-axis in the cutting direction and the Z-axis perpendicular to the plane determined by the X-axis and the straight cutting edge is defined for each ECT. The Y-axis is perpendicular to the X- and Z-axes to form a right-handed coordinate system. The torque, denoted as *T*, generates a force component Fc along the X-axis direction. The $F_c = T/r$, where r is the distance from the drill axis to the center of the ECT. The component of resultant force in the Y-axis is F_l and in the Z-axis is F_t. The thrust force, denoted as F_{Th}, is parallel to the drill-axis and can be decomposed to F_t and F_l (Bono and Ni, 2001).

$$F_{Th} = -F_l \frac{\cos\theta}{\cos\lambda} + F_t \frac{\sqrt{\cos^2\lambda - \cos^2\theta}}{\cos\lambda} \tag{3.1}$$

The resultant force on an ECT can also be decomposed to the force components normal and parallel to the rake face, denoted as F_n and F_f, respectively. F_f is the friction force in the direction of chip flow on the tool rake face. Because the resultant force lies in the plane defined by F_n and F_f, F_l is related to F_c and F_t by (Lin et al., 1982):

$$F_l = \frac{F_c(\sin\lambda - \cos\lambda\sin\alpha\tan\eta) - F_t\cos\alpha\tan\eta}{\sin\lambda\sin\alpha\tan\eta + \cos\lambda} \tag{3.2}$$

F_c, F_l, and F_t are related with F_n and F_f by:

$$\begin{Bmatrix} F_l \\ F_c \\ F_t \end{Bmatrix} = \begin{bmatrix} \cos\lambda & \sin\lambda & 0 \\ \sin\lambda & \cos\lambda & 0 \\ 0 & 0 & 1 \end{bmatrix} \begin{bmatrix} -1 & 0 & 0 \\ 0 & \sin\alpha & \cos\alpha \\ 0 & \cos\alpha & -\sin\alpha \end{bmatrix} \begin{bmatrix} 0 & \sin\eta \\ 0 & \cos\eta \\ 1 & 0 \end{bmatrix} \begin{Bmatrix} F_n \\ F_f \end{Bmatrix} \tag{3.3}$$

From Eq. (4), F_f can be calculated as:

$$F_f = \frac{(\cos\alpha\cos\lambda)F_t + \sin\alpha F_c}{\cos\lambda\cos\eta + \sin\alpha\sin\lambda\sin\eta} \tag{3.4}$$

The F_t can be solved by substituting Eq. (3.2) into (3.1).

$$F_t = \frac{F_{Th}(\sin\lambda\sin\alpha\tan\eta + \cos\lambda)\cos\lambda + F_c(\sin\lambda - \cos\lambda\sin\alpha\tan\eta)\cos\theta}{\sqrt{\cos^2\lambda - \cos^2\theta}(\sin\lambda\sin\alpha\tan\eta + \cos\lambda) + \cos\alpha\tan\eta\cos\theta} \quad (3.5)$$

The chip velocity V_c along the chip flow direction is also required to calculate the frictional heat generation. V_c is calculated from the cutting speed $V = \omega r$, where ω is the drill rotational speed (Shaw et al., 1952).

$$V_c = V\frac{\cos\lambda\sin\phi}{\cos\eta\cos(\phi-\alpha)} \quad (3.6)$$

The chip thickness a_c corresponding to each ECT is experimentally measured and applied to determine the shear angle ϕ (Shaw, 1984).

$$\tan\phi = \frac{acos\alpha}{a_c - a\sin\alpha} \quad (3.7)$$

where $a = f_d \sin\theta$, in which f_d is the feed per tooth, and θ is the angle between the drill axis and ECT cutting edge.

3.3.4. Heat Generation

On the ECT cutting edge, the friction force and chip velocity are multiplied to calculate the heat generation rate by friction, $q_f = F_f V_c$. Defining K to be the heat partition factor determining the ratio of heat transferred to the tool, the heat generation rate on the ECT $q_{tool} = Kq_f$.

In this study, the cutting speed dependent K is applied (Berliner and Krainov, 1991):

$$K = 1 - (1 + 0.45 \frac{k_t}{k_w} \sqrt{\frac{\pi d_w}{V_c l}})^{-1} \tag{3.8}$$

where k_t and k_w are the thermal conductivities of WC-Co tool and Ti workpiece material, respectively, d_w is the diffusivity of Ti, and l is the tool-chip contact length. All thermal properties are temperature-dependent. The tool thermal conductivity k_t is provided by Kennametal. For Ti, k_w and d_w, are obtained from Material Properties Handbook (1981).

The tool-chip contact length l was assumed to be twice the chip thickness in the previous study of drill thermal modeling (Fuh et al., 1984). In this study,

$$l = sa_c \tag{3.9}$$

where s is the ratio of the tool-chip contact length to the chip thickness. The value of s is assumed to be the same across the chisel and cutting edges and is determined by the inverse heat transfer solution.

3.4. Drill Thermo-Mechanical Modeling Procedure

Thermo-mechanical finite element modeling was conducted in two steps. The first step is a thermal modeling incorporating the inverse heat transfer solution to calculate the heat partition on the tool-chip contact area and the convection heat transfer coefficient of cutting fluid and drill temperature distribution. Based on the analyzed drill temperature results, the mechanical modeling is conducted to calculate the drill deformation and stress distributions.

3.4.1. Finite Element Thermal Model

The drill solid model is exported to Abaqus^{TM}, the finite element analysis software used in this study, for mesh generation. Figure 3.7 shows the finite element mesh of the drill, which is modeled by 88,104 four-node tetrahedral elements. As shown in the top view in Figure 3.7(b), 13 nodes are located on the chisel edge and 11 nodes are placed on each cutting edge to achieve good resolution of the temperature distribution in the analysis of drill temperature distribution in Ti drilling.

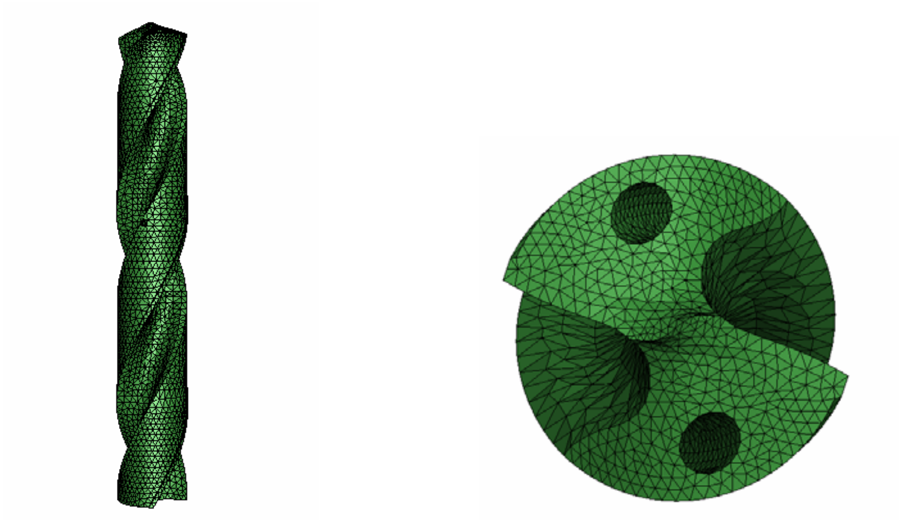

(a) (b)

Figure 3.7. Mesh for the 3D finite element thermal model: (a) side view and (b) top view.

The initial condition of finite element analysis is a uniform temperature of 20°C in the drill. Because the drill does not rotate in the experiment, free convection boundary condition is applied for the whole drill surface. The heat flux of a vertical wall due to free convection in air is applied on the drill surface (Orfueil, 1987):

$$q''_{conv} = B(T - T_\infty)^{1.25} \tag{3.10}$$

where B = 1.8 W/m^2-K$^{1.25}$ and T_∞ = 20°C. The boundary condition on the bottom surface at the end of the drill, opposite from the drill tip, is assumed to be maintained at 20°C.

The heat generation in drilling is applied as a line load at the chisel and cutting edges. As reported in (Machado and Wallbank, 1990), the contact between tool and chip is narrow in Ti machining. Compared to the 0.0254 mm feed per tooth, the characteristic length of the elements at chisel and cutting edges is much larger, around 0.4 mm. This allows the use of line heat source at the cutting edge in finite element thermal analysis. For the chisel edge, because the characteristic length of elements is shorter than the chip contact length, a parabolic heat source along the contact length is applied (Berliner and Krainov, 1991).

3.4.2. Inverse Heat Transfer Solution

Inverse heat transfer utilizes the temperature measured by some thermocouples embedded on the drill flank surface, TC1 in high-throughput drilling of Ti-6Al-4V, as the input to predict the heat generation rate at the drill chisel and cutting edges. The s is solved using an optimization method. The flowchart for inverse heat transfer solution is summarized in Figure 3.8. By assuming a value for s, the l, K, and q_{tool} are calculated and applied to nodes on the cutting and chisel edges of ECT. The spatial and temporal temperature distribution of the drill can then be found. The inverse heat transfer method is applied to solve s by minimizing an objective function determined by the experimentally measured and finite element modeled temperature at specific thermocouple locations, as shown in Figure 3.1, on the drill flank face.

The discrepancy between the experimentally measured temperature at thermocouple j at time t_i, $T_j^{t_i}\Big|_{\exp}$, and finite element estimated temperature at the same thermocouple location and time, $T_j^{t_i}\Big|_{\mathrm{est}}$, determines the value of the objective function:

$$Obj = \sum_{i=1}^{n_i}\sum_{j=1}^{n_j}\left(T_j^{t_i}\Big|_{\exp} - T_j^{t_i}\Big|_{\mathrm{est}}\right)^2 \tag{3.11}$$

where n_i is the number of time intervals during drilling and n_j is the number of thermocouples selected to estimate the objective function.

With the cutting fluid supply, the first step is to find an appropriate estimation of the convection coefficient of cutting fluid, h. This is also solved using the inverse heat transfer method, as illustrated by the flow chart in Figure 3.9 Exp. W183 uses the same cutting speed and feed as Exps. D183, therefore is assumed to have the same tool-chip contact length, s. This s is used in conjunction with the experimentally measured thrust force, torque, and chip thickness to calculate the heat generation rate, q_{tool} and drill temperature distribution. The convection coefficient h is then determined by iteration to minimize the objective function, *Obj*.

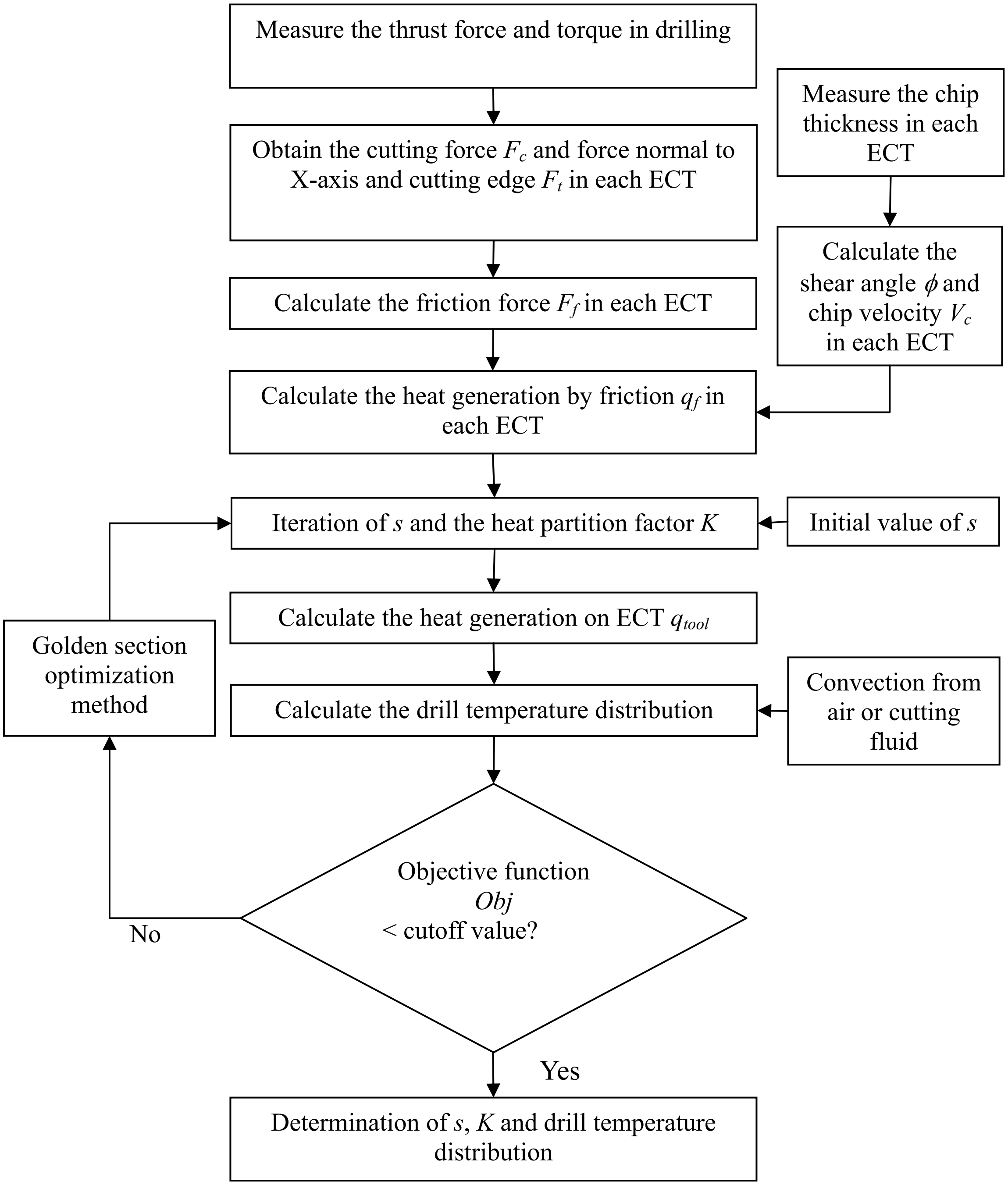

Measure the thrust force and torque in drilling
Obtain the cutting force F_c and force normal to X-axis and cutting edge F_t in each ECT
Measure the chip thickness in each ECT
Calculate the friction force F_f in each ECT
Calculate the shear angle ϕ and chip velocity V_c in each ECT
Calculate the heat generation by friction q_f in each ECT
Iteration of s and the heat partition factor K
Initial value of s
Calculate the heat generation on ECT q_{tool}
Golden section optimization method
Calculate the drill temperature distribution
Convection from air or cutting fluid
Objective function Obj < cutoff value?
No
Yes
Determination of s, K and drill temperature distribution

Figure 3.8. Flow chart of the inverse heat transfer solution of heat partition on tool-chip interface.

3.4.3. Finite element drill stress analysis

The drill stress is solved using thermo-mechanical finite element modeling. The combination of thermal stress due to high temperature in the drill and mechanical stress caused by the cutting force applied on ECTs determines the spatial and temporal distributions of the drill stress. The same 3D finite element mesh (Figure 3.7) used for thermal modeling is applied for stress analysis. The bottom (away from the tip) of the drill is assumed to be fixed. Cutting forces in each ECT are assumed to be uniformly distributed across the edge of the ECT. These distributed forces are converted into forces on nodes comprising the cutting and chisel edges.

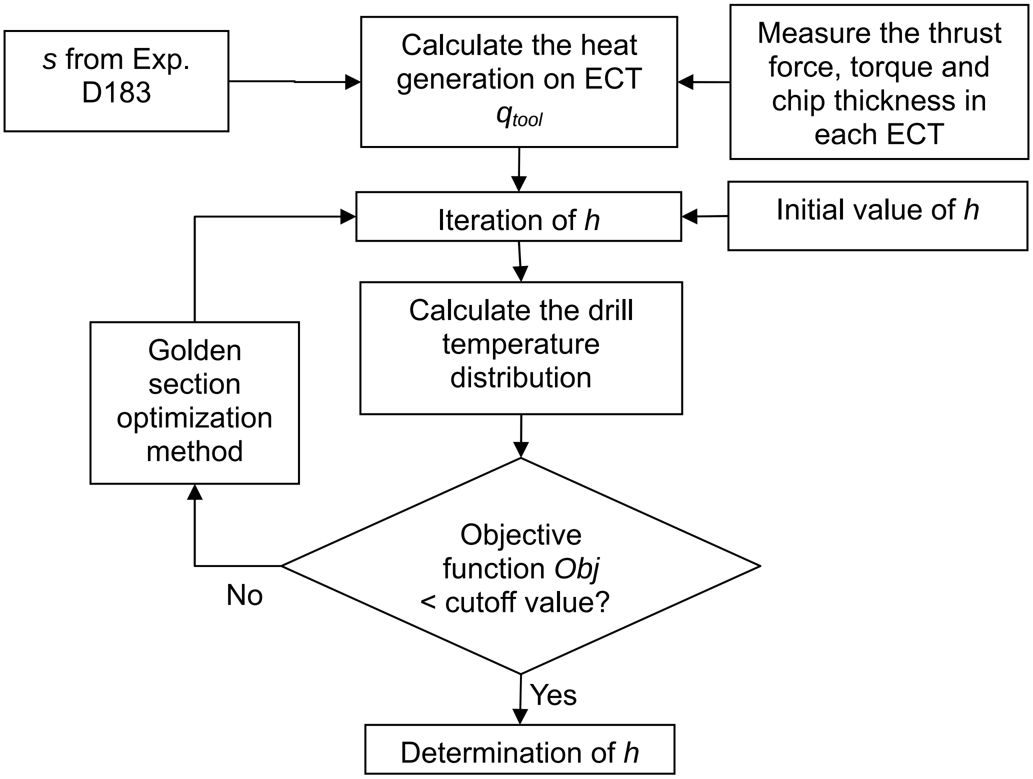
s from Exp. D183
Calculate the heat generation on ECT q_{tool}
Measure the thrust force, torque and chip thickness in each ECT
Iteration of h
Initial value of h
Calculate the drill temperature distribution
Golden section optimization method
Objective function Obj < cutoff value?
No
Yes
Determination of h

Figure 3.9. Flow chart of the inverse heat transfer solution of cutting fluid convection coefficient.

3.5. Drill Temperature Analysis Results

The temporal and spatial drill temperature distributions in four experiments, Exps. D183, W183, W91, and W61, are presented.

3.5.1. Exp. D183

The s and heat generation rate in Exp. D183 is solved first. By minimizing Obj using the measured temperature at TC1, the value of s is solved as 7.0. This is comparable to the values of s obtained in a previous study of drilling CP Ti using the same drill geometry (Li and Shih, 2006). Applying the s and temperature-dependent material properties, K and q_{tool} vary both spatially and temporally. To compare the heat transferred to each ECT, q_{tool} is divided by the length of the ECT cutting edge to calculate the heat generation rate per unit length of contact, denoted as q'_{tool}. Results of q'_{tool} after 1.9 mm depth of drilling, i.e., the drill cutting edge fully engaged in the workpiece, are shown in Figure 3.10. Consistently, ECTs at the cutting edge have a much higher q'_{tool} than those at the chisel edge.

The finite element thermal model is validated by comparing with the experimentally measured temperature at thermocouple TC2 which is not used as the input for inverse heat transfer analysis and is therefore an independent measurement. As shown in Figure 3.11, the model temperature matches well with experimentally measured temperature at TC2 as well as TC1, the input of the inverse heat transfer analysis.

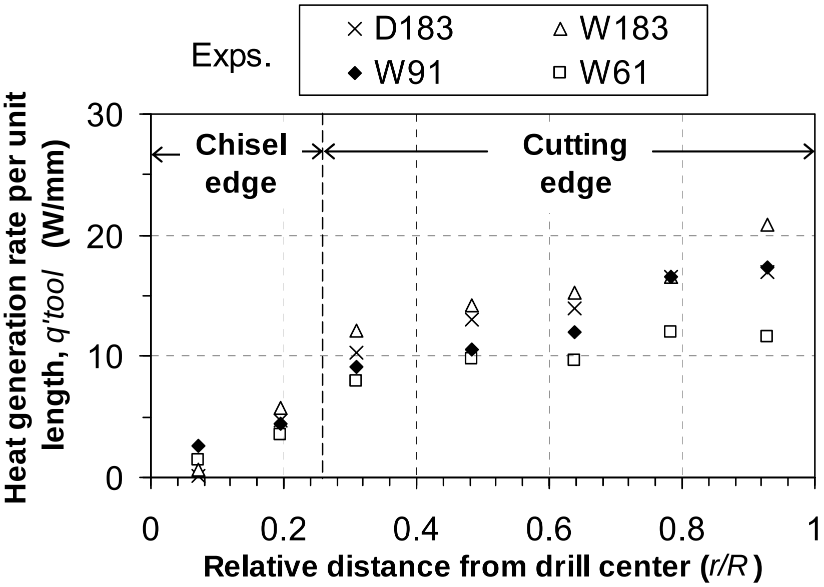

Figure 3.10. The heat generation rate per unit length q'_{tool} at seven ECTs after 1.9 mm depth of drilling.

To quantify the discrepancy between the experimental and modeling results, the root mean square (RMS) error, e_{RMS} (Li and Shih, 2006; Ozisik and Orlande, 2000) between the measured and predicted temperatures, and the percentage error, p, defined as the ratio of e_{RMS} to the highest measured temperatures, are compared in all four experiments. The results of e_{RMS} and p at TC1 and TC2 are listed in Table 3.2. For Exp. D183, the e_{RMS} at TC2 is very close to that of TC1. The p of both thermocouples is 1.4%. In summary, the low e_{RMS} and p at two thermocouples throughout the drilling process validates the proposed method to predict the spatial and temporal drill temperature distributions.

The temporal change of the ECT temperature at drill chisel and cutting edges in four drilling tests vs. the drilling depth is shown in Figure 3.12. When an ECT is engaged in cutting, the temperature of the ECT increases immediately. For dry drilling

(Exp. D183), the ECT temperatures continue to increase after the initial rapid jump which occurs upon engagement. This is detrimental to the drill life.

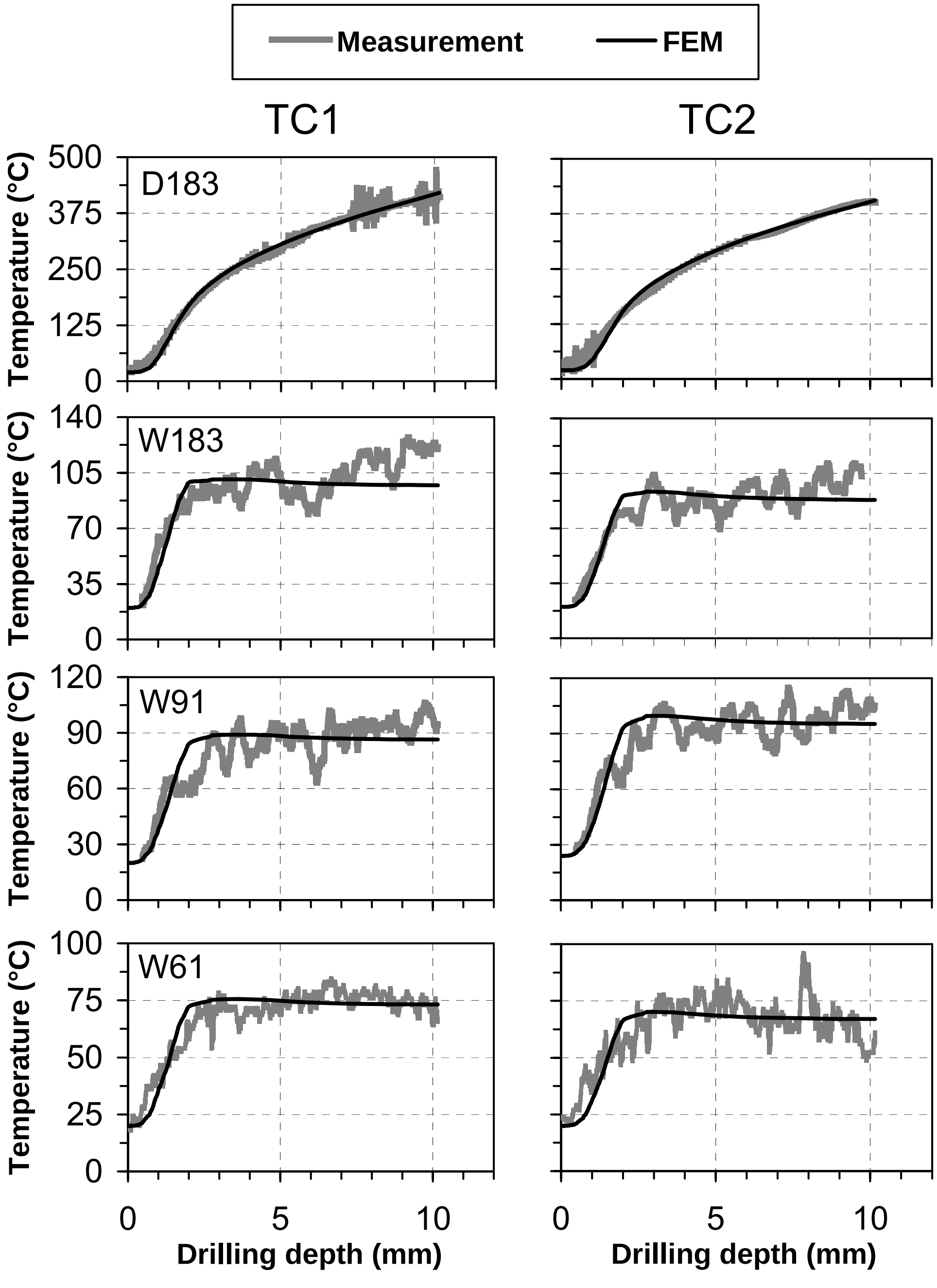

Figure 3.11. Comparison of the measured and calculated temperatures at TC1 (input of inverse heat transfer analysis) and TC2 (for validation).

The chisel edge temperature is higher than that of the cutting edge only at the very beginning, when the cutting edge has not engaged the workpiece. After drilling to a depth of 1.9 mm (the point length), ECT 7 becomes the hottest ECT and remains so until the end of drilling.

Table 3.2. Root mean square and percentage errors of the predicted and measured temperatures.

Exp.		TC1	TC2
D183	e_{RMS} (°C)	9.9	9.7
	p (%)	1.4	1.4
W183	e_{RMS} (°C)	31.3	28.7
	p (%)	4.6	4.3
W91	e_{RMS} (°C)	33.0	22.2
	p (%)	4.8	3.3
W61	e_{RMS} (°C)	7.1	10.4
	p (%)	1.0	1.5

The spatial drill temperature distribution of Exp. D183 at 10.2 mm depth of drilling is shown in Figure 3.13(a). High temperatures are concentrated along the cutting edge at the drill tip. The peak temperature is located on the cutting edge near the drill margin. The peak temperature is high, 1210ºC, which is close to the limit of WC-Co tool material.

3.5.2. Exp. W183

Assuming *s* does not change with the supply of cutting fluid at the same cutting speed and feed, the convection coefficient *h* for the cutting fluid is solved using the inverse heat transfer solution, and is found to be 15000 W/m^2-K. This value is in the range reported in published experimental data (Kalidas, 2002). As shown in Figure 3.10, at the same cutting speed and feed, the supply of cutting fluid results in higher q'_{tool} because of the lower tool and workpiece temperatures and higher cutting forces. Figure 3.24 shows that the discrepancy between the experimental and modeling results is small at thermocouples TC1 and TC2. The e_{RMS} and *p*, as shown in Table 3.2, are larger in Exp. W183 than those in Exp. D183. This is primarily due to the thermocouple measurement noise induced by cutting fluid, as shown in Figure 3.11. The prediction is still accurate. For both thermocouples, *p* is less than 5.0%.

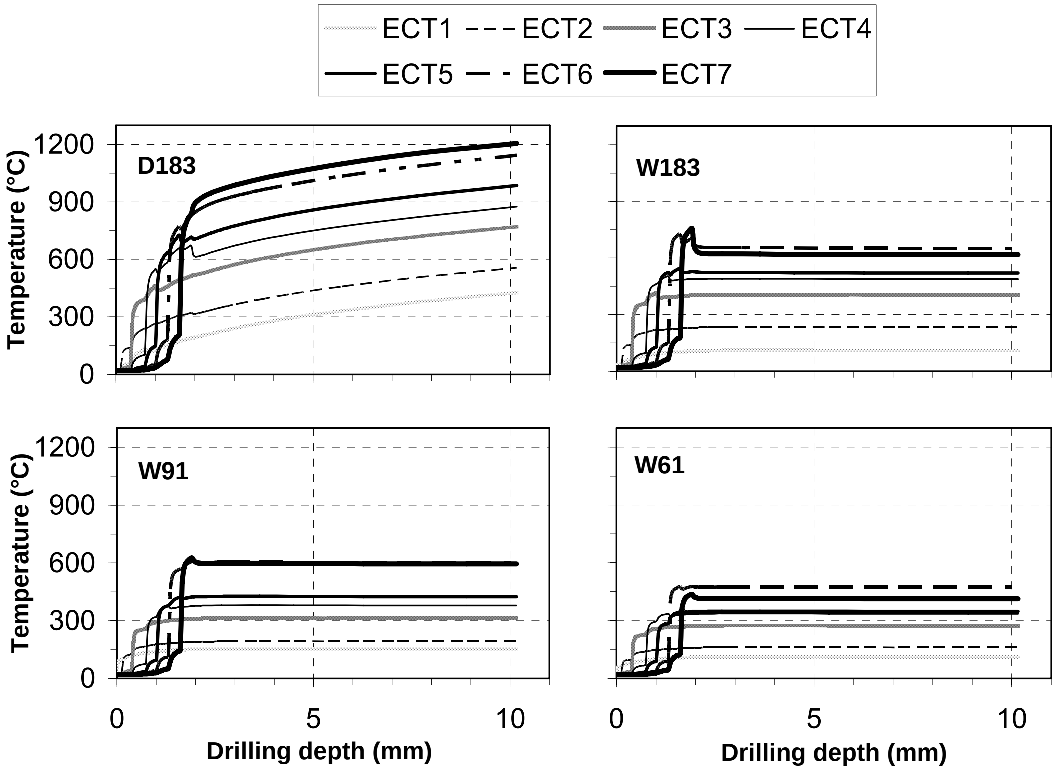

Figure 3.12. Temperature distributions along drill chisel and cutting edges as a function of drilling depth.

As shown in Figure 3.12, the temporal distributions of the chisel and cutting edge temperatures of Exp. W183, as compared to those of Exp. D183, illustrate the effects of cutting fluid to reduce and maintain the drill temperature at a much lower level. Drill temperatures in Exp. W183 reaches a steady state level shortly after the corresponding ECT is fully engaged with the workpiece. The chisel edge (ECTs 1 and 2) also has a low temperature. In Exp. W183, ECT 6 has a slightly higher temperature than that of ECT 7, which is a different trend than that of Exp. D183. The spatial temperature distribution of Exp. W183 after 10.2 mm of drilling is shown in Figure 3.13(b). The peak temperature has moved inside to ECT 6 as compared to Exp. D183 in Figure 3.13(a). The radial distance from the peak drill temperature on cutting edge to the drill margin is 0.36 and 1.09 mm for Exps. D183 and W183, respectively. This is beneficial because, away from the drill margin, ECT 6 has a smaller rake angle and stronger cutting edge geometry than ECT 7 to withstand the high temperature related tool strength softening. Under the same cutting speed, the internal cutting fluid supply has a significant effect on the peak drill temperature, reducing it by almost half to 651ºC after 10.2 mm of drilling.

3.5.3. Exps. W91 and W61

Assuming the same convection coefficient h as in W183, the s in Exps. W91 and W61 remains at 7.0, the same as the value in Exp. W183. The decrease of cutting speed (and corresponding increase of feed to maintain the same MRR) does not change the value of s, but as shown in Figure 3.10, it leads to a lower heat generation rate $q_{tool}^{'}$ and drill temperature.

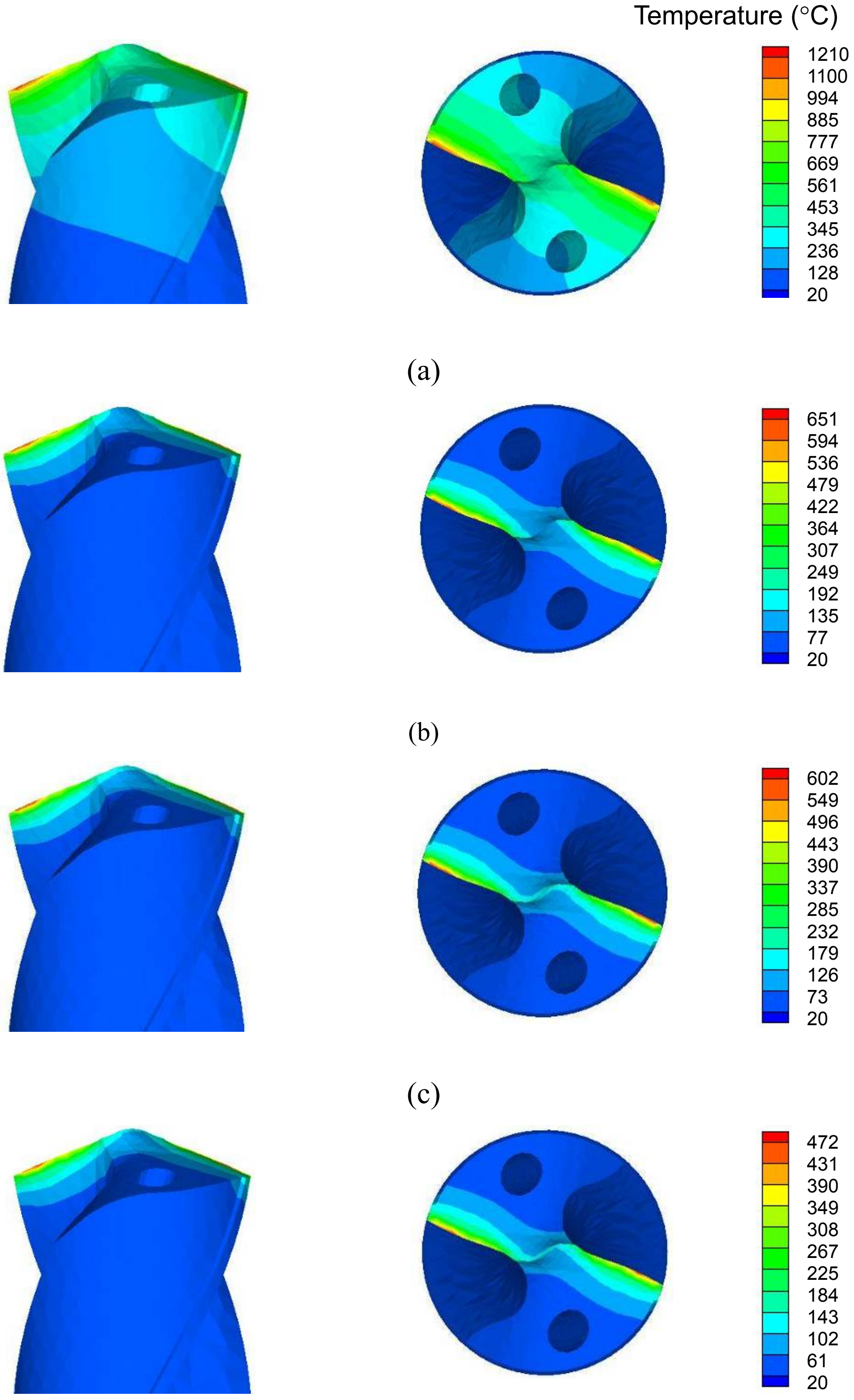

(a)

(b)

(c)

(d)

Figure 3.13. Temperature distributions at the drill tip after 10.2 mm depth of drilling in Exps: (a) D183, (b) W183, (c) W91, and (d) W61.

The inverse thermal modeling is accurate for Exps. W91 and W61. Figure 3.11 shows the close correlation between the measured and predicted temperatures at TC2. The eRMS and p of TC2, as listed in Table 3.2, are comparable to those of Exp. W183. Figure 3.12 shows the temporal development of ECT temperature remains nearly constant for each of the three tests in which cutting fluid was used.

The decrease of cutting speed and increase of feed have reduced the temperature at ECT 6, which has the highest temperature among all ECTs. The peak temperature, as shown in Figs. 3.13(c) and (d), has reduced from 651ºC in Exp. W183 to 602ºC and 472ºC in Exps. W91 and W61, respectively. However, the drill stress will increase as a result of the increase in feed and decrease in temperature. This will be quantified in Section 3.7.

3.6. Drill Deformation

Under high temperatures and stresses in drilling, the drill deforms both axially and radially. The increase in drill temperature expands the drill length and diameter due to thermal expansion. The force at the cutting edge decreases the drill length but increases the drill diameter. The combinational effect of temperature and stress changes the drill geometry and affects the shape of the hole.

The shape of the deformed drill for Exp. D183 after 10.2 mm of drilling is shown in Figure 3.14 with 20 times amplification of deformation. The drill deformation is quantified by two parameters: the change in the drill length and the diameter. The change in length is defined by the change of total length from the drill tip to the base after imposing the temperature and cutting force on the drill. The change of diameter is the difference between the diameter of the originally round drill and the largest enclosing diameter of the drill after 10.2 mm of drilling.

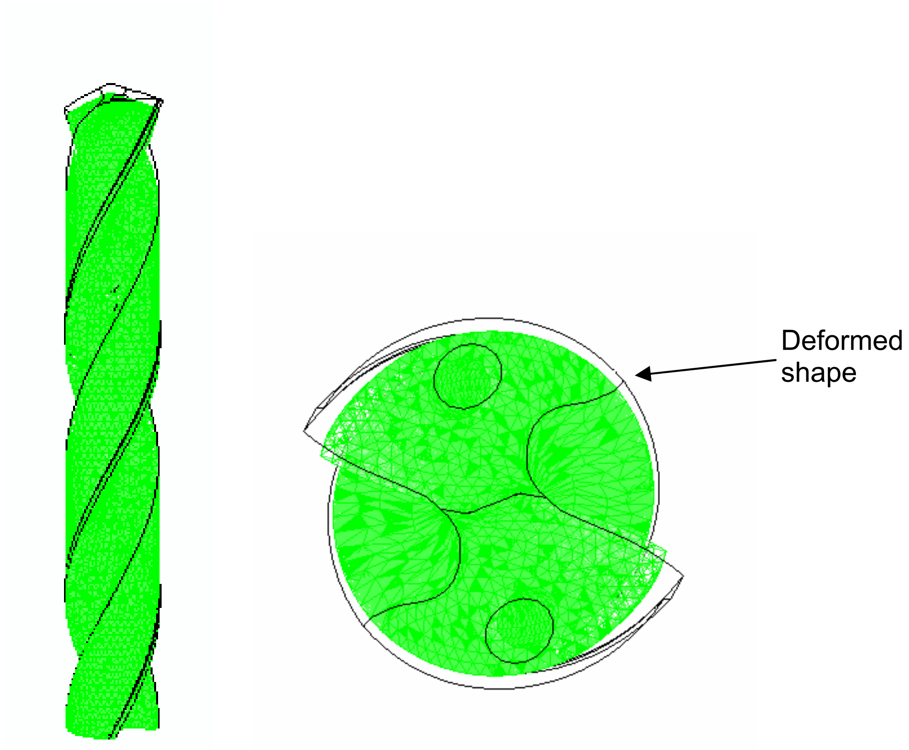

Figure 3.14. Drill deformation after 10.2 mm drilling in Exp. D183 (scale factor of deformation: 20).

Table 3.3 lists the change in drill length and diameter in four drilling experiments. In all experiments, the thermal expansion effect outweighs the mechanical force effect in increasing the total length and diameter of the drill. The drill expands the most, 18.4 μm in length and 12.0 μm in diameter, in dry drilling, Exp. D183. In wet drilling, the drill deformations are not as significant, about 7 μm increase in length and 3 μm increase in diameter.

The mechanical force effect (without considering the thermal expansion effect) on the change in length and diameter is also listed in Table 3.3. The drill shortens in axial direction and expands in radial direction, but the deformation is one order of magnitude lower than that under thermo-mechanical conditions. This concludes that the effect of thermal expansion outweighs the mechanical forces in drill deformation.

Table 3.3. Drill deformation under the thermo-mechanical and mechanical-only conditions.

Exp.	D183	W183	W91	W61
Length increase (μm)	18.4	7.66	6.84	6.79
Diameter increase (μm)	12.0	3.77	3.53	2.95
Length reduction by mechanical load only (mm)	0.59	0.42	1.17	0.93
Diameter increase by mechanical load only(mm)	0.28	0.29	0.38	0.41

3.7. Drill Stress and Failure Prediction

WC-Co is a brittle material with highly different tensile and compressive strengths (Paul and Mirandy, 1976). Three commonly used failure criteria for brittle materials are the Rankine, Mohr-Coulomb (Chen and Han, 1988) and modified Mohr criteria (Barber, 2001). All failure criteria used three principal stresses, denoted as σ_1, σ_2, and σ_3 with $\sigma_1 > \sigma_2 > \sigma_3$. The maximum and minimum principal stress, σ_1 and σ_3, along the drill chisel and cutting edges in four experiments are shown in Figure 3.15. Under all four drilling conditions, the drill shows high tensile (positive) σ_1 and compressive (negative) σ_3 at the chisel edge. A peak of high compressive principal stress σ_3 is observed at the location r/R (relative distance to drill center) = 0.2. The whole cutting edge is under a state of high compression with high compressive σ_1 and σ_3.

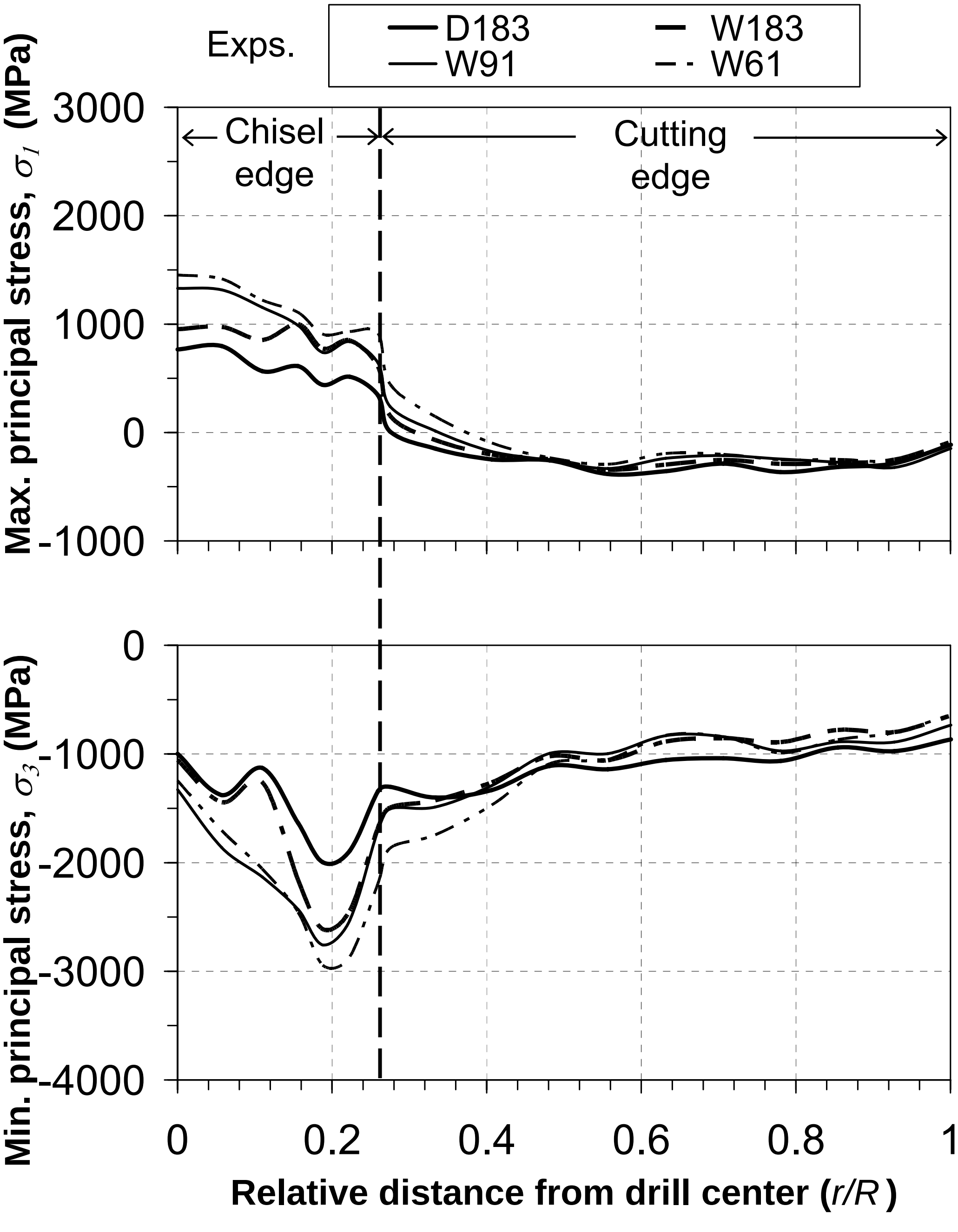

Figure 3.15. Maximum principal stress, σ_1, and minimum stress, σ_3, along the drill chisel and cutting edges after 10.2 mm depth of drilling.

The Rankine criterion is the simplest among the three brittle material failure criteria. Rankine criterion, also known as maximum normal stress criterion (Chen and Han, 1988), states that brittle material fails when the principal stress either exceeds the uniaxial tensile strength σ_t or compressive strength σ_c. The Rankine criterion can be expressed as $\sigma_1=\sigma_t$ or $\sigma_3=\sigma_c$.

Assuming that the maximum shear stress determines the onset of failure, the Mohr-Coulomb criterion or internal-friction theory, suggests that failure occurs when the Mohr's circle of a point in the body exceeds the envelope created by two Mohr's circles for uniaxial tensile strength σ_t and uniaxial compressive strength σ_c (Chen and Han, 1988). If the Mohr envelope is simplified as a straight line, this criterion can be written as:

$$\frac{\sigma_1}{\sigma_t}-\frac{\sigma_3}{\sigma_c}=1 \tag{3.12}$$

The modified Mohr criterion derives from the Rankine criterion and considers the variation of material strength with lateral compressive stress. It can be described by the following equation:

$$\max\left(\frac{\sigma_1}{\sigma_t},-\frac{\sigma_3}{\sigma_c},\frac{\sigma_1}{\sigma_t}-\frac{\sigma_1+\sigma_3}{\sigma_c}\right)=1 \tag{3.13}$$

The tensile strength σ_t and compressive strength σ_c are temperature-dependent. During drilling, the drill temperature and, subsequently, the strength vary temporally and spatially. Hence, the stress limits vary from point to point in a drill. To quantify how close the material is to failure, three dimensionless stresses $\bar{\sigma}_r = \max(\frac{\sigma_1}{\sigma_t}, -\frac{\sigma_3}{\sigma_c})$, $\bar{\sigma}_{m-c} = \frac{\sigma_1}{\sigma_t} - \frac{\sigma_3}{\sigma_c}$, and $\bar{\sigma}_{m-m} = \max(\frac{\sigma_1}{\sigma_t}, -\frac{\sigma_3}{\sigma_c}, \frac{\sigma_1}{\sigma_t} - \frac{\sigma_1 + \sigma_3}{\sigma_c})$ associated with the Rankine, Mohr-Coulomb, and Modified Mohr criteria, respectively, are defined. The closer these dimensionless stresses are to 1.0 indicates the higher likelihood of material failure.

Figure 3.16 compares these three dimensionless stresses in the drill after 10.2 mm drilling in Exp. D183. It is noticed that values of $\bar{\sigma}_r$ and $\bar{\sigma}_{m-m}$ are about the same, but $\bar{\sigma}_{m-c}$ has much lower value. The maximum values of $\bar{\sigma}_r$ and $\bar{\sigma}_{m-m}$ are 0.91 at the cutting edge. However, the maximum value of $\bar{\sigma}_{m-c}$ is only 0.71, which is located at the chisel edge. This difference lies in the fact that $\bar{\sigma}_{m-c}$ does not consider the limit of normal stress. At the cutting edge, the stress state is closer to the compressive strength than to the shear stress limit as defined by the Mohr-Coulomb criterion. Based on this observation, the modified Mohr criterion is selected to analyze the drill stress because it includes the maximum normal stress limit.

The contour plots of $\bar{\sigma}_{m-m}$ of three wet drilling experiments are shown in Figure 3.17. Dry and wet drilling experiments have a totally different pattern of $\bar{\sigma}_{m-m}$. In Exp. D183 (Figure 11), the highest $\bar{\sigma}_{m-m}$ (=0.91) is located at the cutting edge. This is primarily due to the high compressive stress and the low tensile strength σ_t and compressive strength σ_c due to high temperature at the cutting edge. In Exps. W183, W91, and W61 (Figure 3.13), $\bar{\sigma}_{m-m}$ at the cutting edge is much smaller compared with that of Exp. D183, and the highest $\bar{\sigma}_{m-m}$ is located at the chisel edge. This is due to the increase of tensile strength σ_t and compressive strength σ_c at low temperature, especially in the cutting edge. The supply of cutting fluid decreases the maximum $\bar{\sigma}_{m-m}$ from 0.91 in Exp. D183 to 0.75 in Exp. W183. Under the wet drilling condition, the maximum $\bar{\sigma}_{m-m}$ increases from 0.75 in Exp. W183 to 0.77 and 0.84 in Exps. W91, and W61, respectively.

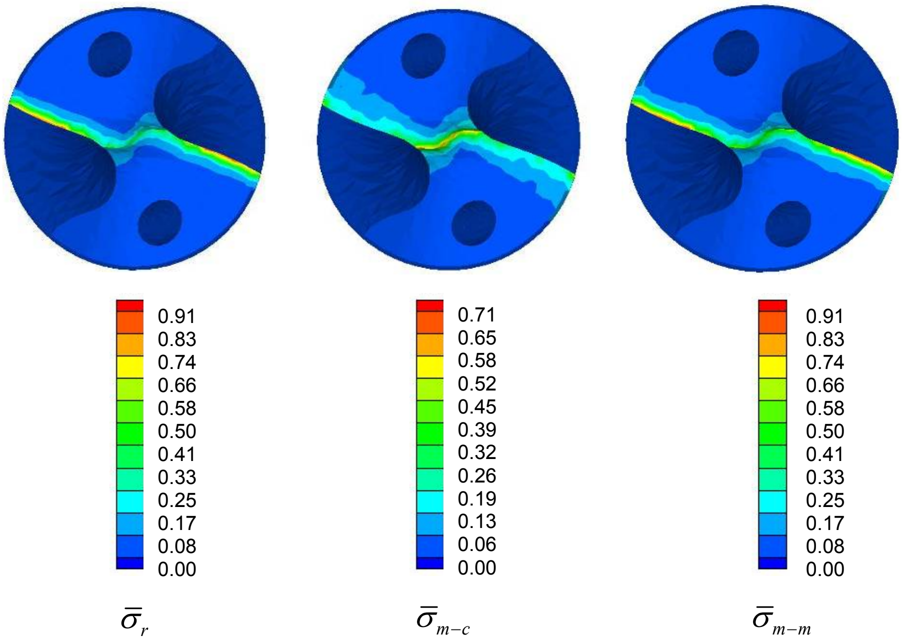

Figure 3.16. Comparison of dimensionless stresses, $\bar{\sigma}_r$, $\bar{\sigma}_{m-c}$, and $\bar{\sigma}_{m-m}$, after 10.2 mm depth of drilling in Exp. D183.

The high tool temperature promotes diffusion wear, while high stress induces brittle fracture. In dry drilling (Exp. D183), the temperature and dimensionless stress at the cutting edge are both high, which results in the severe drill wear at the cutting edge and short drill life.

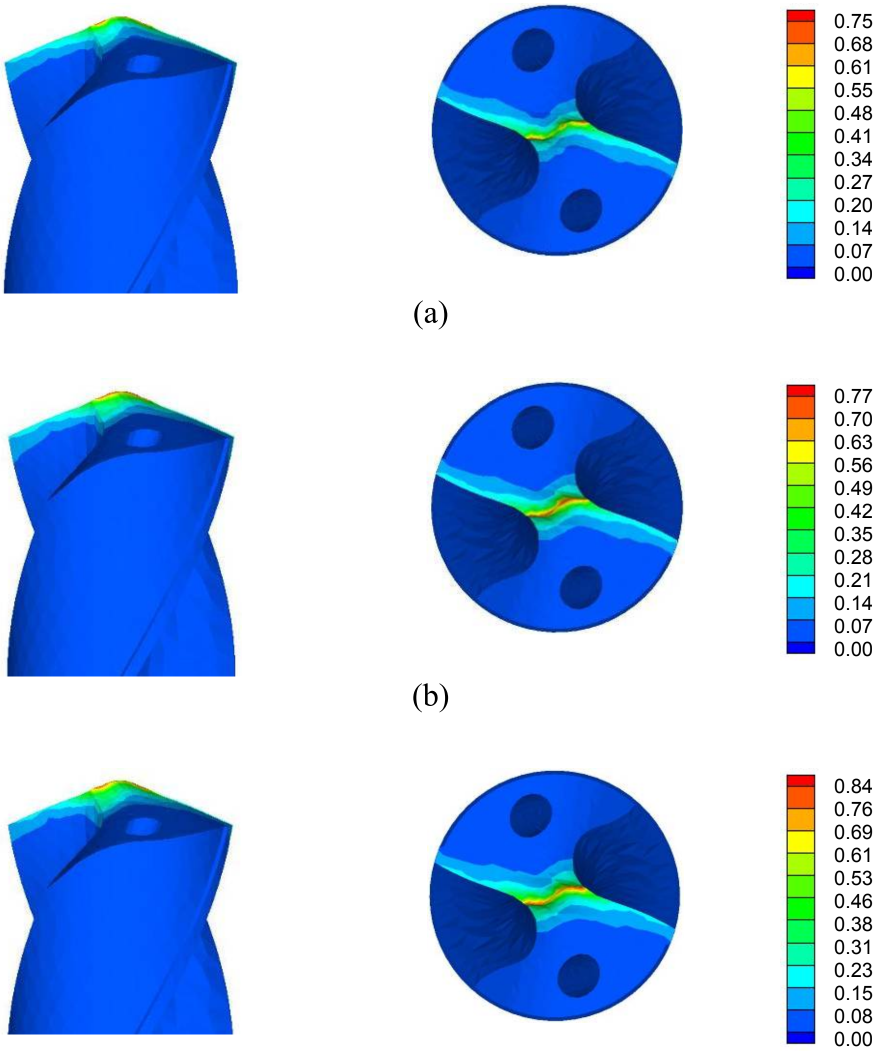
0.75
0.68
0.61
0.55
0.48
0.41
0.34
0.27
0.20
0.14
0.07
0.00
0.77
0.70
0.63
0.56
0.49
0.42
0.35
0.28
0.21
0.14
0.07
0.00
0.84
0.76
0.69
0.61
0.53
0.46
0.38
0.31
0.23
0.15
0.08
0.00

(a)

(b)

(c)

Figure 3.17. Distributions of dimensionless stress $\bar{\sigma}_{m-m}$ at the drill tip after 10.2 mm depth of drilling in Exps: (a) W183, (b) W91, and (c) W61.

In wet drilling, the drill temperature is low, but the dimensionless stress increases with the reduced cutting speed and increased feed. Thus, the competing factors of temperature and stress in the chisel edge indicate that an optimum combination of the cutting speed and feed exists. A high-throughput drilling test using the same peripheral cutting speed but a smaller 3.97 mm diameter drill shows that the drill life is very short in dry drilling and the highest drill life occurs at 91 m/min cutting speed (0.102 mm/rev feed) with an internal cutting fluid supply (Li and Shih, 2007a). This drill life data matches to the failure analysis results.

3.8. Concluding Remarks

This study developed the computational models and experimental procedures to predict the spatial and temporal distributions of drill temperature and stress for drilling of Ti. The inverse heat transfer method with a finite element thermal model was applied to find the heat partition on the tool-chip contact region and the convection heat transfer coefficient of cutting fluid for the 9.92 mm diameter spiral point drill. The inverse heat transfer analysis, which used experimentally measured thrust force, torque, chip thickness, and temperature as inputs, was validated with reasonably good agreement.

This study showed that the highest temperature of the drill occurred in the cutting edge under all four drilling conditions. The modified Mohr criterion predicted that the onset of drill failure would initiate in the cutting edge for dry drilling and in the chisel edge for wet drilling. The supply of cutting fluid via through-drill holes was found to be critical in reducing the drill temperature. Without cutting fluid, the temperature was high and continued to rise during drilling. The supply of cutting fluid maintained the drill temperature at a constant level during drilling and was able to decrease the drill peak temperature by half after 10.2 mm drilling of Ti-6Al-4V. The supply of cutting fluid helped to prevent premature tool failure due to high drill temperature. The maximum dimensionless stress of the modified Mohr criterion decreased from 0.91 in dry drilling to 0.75 in wet drilling at 183 m/min cutting speed. The results also suggested that lower peripheral cutting speed and higher feed could further reduce the drill temperature while maintaining the same MRR, but the chisel edge would undergo increasingly higher stress.

This study has identified several future improvements on computational models. The sequential thermo-mechanical analysis in this paper assumed the stress solution was dependent on a temperature field but there was no inverse dependency. To simulate the drilling process more accurately, a coupled thermo-mechanical modeling will be used to solve the stress and temperature simultaneously. Several key assumptions made in this study, including that the ratio of the tool-chip contact length to the chip thickness is constant across the chisel and cutting edges and independent of the cutting fluid supply and the same convection coefficient used for all wet drilling conditions should be considered for future improvements.

This study can be used to aid drill selection, drill geometry design, and optimization of drilling process parameters. For spiral point drills, the chisel edge drill geometry can be refined to reduce the peak compressive principal stress at the relative distance to the drill center (r/R), 0.2. This improvement can potentially further enhance the productivity of drilling Ti and other advanced engineering materials.

CHAPTER 4

3D FINITE ELEMENT MODELING OF HIGH-THROUGPUT DRILLING PROCESS

The updated-Lagrangian finite element modeling of high throughput drilling of Ti-6Al-4V using a spiral point drill was conducted. In the model, the chisel and cutting edges of a spiral point drill were treated as a series of straight-cutting-edge elementary cutting tools with various rake and inclination angles. The oblique-cutting finite element modeling software, AdvantEdge™, was applied to study the cutting forces and material deformation of each elementary cutting tool. Both dry drilling and drilling with internal cutting fluid supplied through the drill body, were investigated. All drilling tests have the same high material removal rate (384 mm^3/s) but different cutting speeds and feeds. The thrust force and torque predicted by the finite element model matched well with experimentally measured values. The model also enables better understanding of the work-material deformation and drill temperatures and stresses.

4.1. Introduction

Yang and Liu (1999) concluded that, to further reduce the cost of effective machining of Ti, a better understanding of the underlying mechanism of Ti machining process was necessary through better process and performance models, thermal modeling, and finite element simulation. Benefiting from advancement of computational power, finite element modeling (FEM) is becoming a standard, commercially-available tool to analyze the machining process in recent years. FEM of metal cutting can be classified into the Eulerian and updated-Lagrangian methods. The Eulerian method has a fixed mesh and captures the continuous material flows around the tool tip (Strenkowksi et al., 2004). It is based on the assumption of uniform chip thickness with no segmented or discontinuous chip formation. The updated-Lagrangian method tracks a fixed material body as it approaches and passes the tool, meaning it can model complicated chip morphology. The chip is serrated in Ti machining, so the updated-Lagrangian formation is necessary to accurately model the cutting process. The continuous remeshing technique has been developed to relieve the severe mesh distortion resulting from the large-strain and high-strain rate plastic deformation in the machining process.

Compared to numerous models of orthogonal and oblique cutting, the research in the FEM of drilling is limited, mainly due to the complexity of tool geometry and difficulty in modeling the large negative rake angle cutting which occurs in the drill center (at the chisel edge). Using the Eulerian formulation, Strenkowski et al. (2004) has developed the approach of dividing conventional twist drill into a series of elementary cutting tool (ECT) segments (Armarego and Cheng, 1972; Wiriyacosol and Armarego, 1979; Watson, 1985) and applying the oblique cutting model for each ECT to predict the forces and torque in drilling. For the updated-Lagrangian method, Guo and Dornfeld (1998, 2000) have investigated 3D drilling burr formation with a split point drill, Min et al. (2001) developed a 2D burr formation model for a twist drill, and Marusich et al. (2006) simulated 3D drilling of Ti-6Al-4V using a conventional twist drill. However, the updated-Lagrangian method has not yet been applied to predict the thrust force and torque in drilling due to the technical difficulty in modeling the material deformation under the large negative rake angle at the chisel edge. The goal of this study is to expand the ECT-based oblique cutting approach to model the Ti drilling using the spiral point drill.

The high-throughput drilling of Ti-6Al-4V was proven experimentally feasible (Li and Shih, 2007a). This created an immediate need for modeling of high-throughput Ti drilling to understand the underlying material removal mechanism. The 3D updated-Lagrangian finite element method is applied because it can simulate the complicated serrated chip formation in the high-throughput drilling. In this chapter, the spiral point drill geometry is introduced first. The oblique cutting mechanics, finite element model, and validation experimental setup are then presented. Finally the model validation and modeling results are discussed.

4.2. Finite Element Drilling Model

4.2.1. Drill Geometry Model and Oblique Cutting Mechanics

The drill used in this paper was a 9.92 mm diameter spiral point drill (Kennametal K285A03906). The drill chisel and cutting edges were treated as a series of ECTs, as shown in Figure 3.3. For each ECT, oblique cutting mechanics is applied to calculate the cutting forces in its local coordinate system. The oblique cutting model of an ECT is shown in Figure 3.6. The thrust force and torque of the whole drill is calculated from the sum of forces on each ECT through a coordinate transformation from each local ECT coordinate system to the global (drill) coordinate system, as discussed in Sec. 3.3.

4.2.2. Oblique Cutting FEM Modeling

Figure 4.1 shows the initial 3D finite element mesh of the oblique cutting models of ECT1, which is at the drill center, ECT4, which is in the middle of the cutting edge, and ECT7, which is at the drill periphery. A 4-node tetrahedral element type is used to model the workpiece and tool. The initial mesh of the workpiece is coarse, but the mesh density increases quickly and significantly at the start of cutting, particularly at the tool cutting edge. This is because the work material deforms severely along tool cutting edge. Finer mesh is generated automatically by adaptive mesh to handle this material deformation. The top and back surfaces of the tool are fixed in all directions. The workpiece is constrained in the vertical and lateral directions on the bottom surface and moves at the cutting speed in the horizontal direction towards the stationary tool. The cutting configurations at different locations have clear differences: ECT1 has large negative rake angle and small inclination angle, ECT4 has a small positive rake angle and a medium inclination angle, while ECT7 has a large positive rake angle and a medium inclination angle.

4.2.3. Equations of Motion

The 3D models are governed by the equations of motion in tensor form (Marusich and Ortiz, 1995):

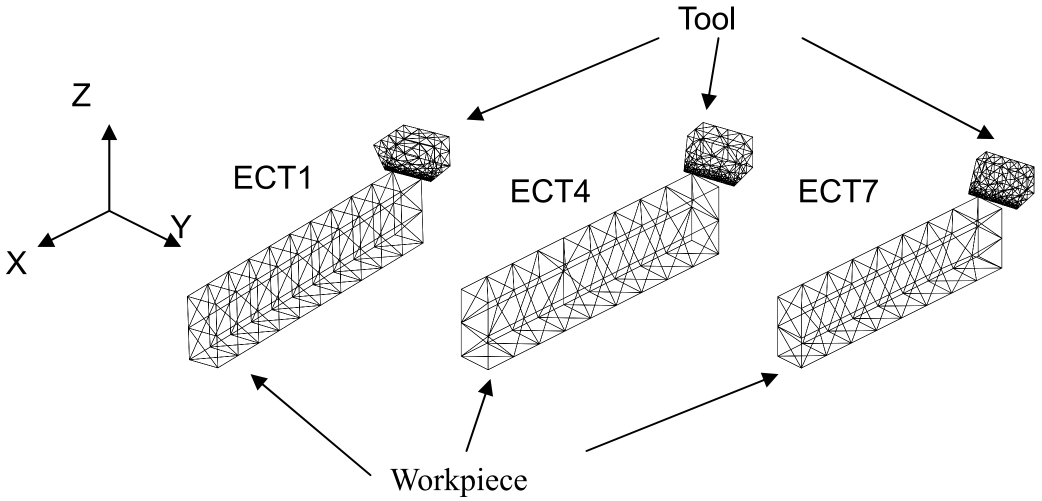

Figure 4.1. Initial finite element mesh for 3D oblique cutting model of three ECTs.

$$\rho\ddot{u}_i = \sigma_{ij,j} + \rho b_i \tag{4.1}$$

where

$\sigma_{ij,j}$ is the partial differentiation of stress in i direction,

ρ is the density of the material,

b_i is the body force in i direction, and

$\ddot{u}_i$ is the acceleration in i direction.

Integration by the virtual work principle provides

$$\int_{B_0} \rho v_i \ddot{u}_i dV = \int_{B_0} v_i \sigma_{ij,j} dV + \int_{B_0} v_i \rho b_i dV \tag{4.2}$$

$$\int_{B_0} \rho v_i \ddot{u}_i dV + \int_{B_0} v_{i,j} \sigma_{ij} dV = \int_{\partial B_{0\tau}} v_i \sigma_{ij} n_j d\Omega + \int_{B_0} v_i \rho b_i dV \tag{4.3}$$

where

v_i is the virtual displacement in the i direction,

B_0 is the space occupied by the solid, and

$B_{0\tau}$ is the boundary of B_0.

Finite element discretization of the equation provides a matrix form equation

$$\mathbf{Ma} + \mathbf{R}^{int} = \mathbf{R}^{ext} \tag{4.4}$$

where

$\mathrm{M}_{\mathrm{ab}} = \int_{B_0} \rho \mathrm{N}_{\mathrm{a}} \mathrm{N} dV_0$ is the mass matix,

a_i is the nodal acceleration,

$R_{ia}^{\mathrm{int}} = \int_{B_0} P_{iJ} N_{a,J} dV_0$ is the internal force item, in which P_{iJ} is the first Piola-Kirchhoff stress tensor,

$R_{ia}^{ext} = \int_{B_0} b_i N_a dV_0 + \int_{\partial B_{0\tau}} \tau_i N_a d\Omega_0$ is the external force item, and

N_a and N_b are shape functions.

4.2.4. Thermal Equations

The thermal analysis of the model is governed by the heat diffusion equations:

$$\rho c\dot{T} = -k\Delta T + \dot{q} \tag{4.5}$$

where

ρ is the mass density,

c is the heat capacity,

T is the temperature,

$\dot{T}$ is the time rate of temperature change,

k is conductivity, and

q is the heat generation rate.

Integration of the equation provides

$$\int_{B_t} \rho c\dot{T}\eta dV + \int_{B_t} D\nabla T \cdot \nabla \eta dV = \int_{B_t} \dot{q}\eta dV \tag{4.6}$$

where η is the virtual temperature, and

B_t is the space occupied by the solid.

Finite element discretization provides the matrix form equation

$$\mathbf{C}\dot{\mathbf{T}} + \mathbf{KT} = \mathbf{Q} \tag{4.7}$$

where

$C_{ab} = \int_{B_t} \rho c N_a N_b dV_0$ is the heat capacity matrix,

$K_{ab} = \int_{B_t} D_{ij} N_{a,i} N_{b,j} dV_0$ is the conductivity matrix, and

$Q_a = \int_{B_t} s N_a dV_0 + \int_{\partial B_{tq}} h N_a dS$ is the heat source,

s is the distributed heat source generated by the plastic deformation in the workpiece,

h is the heat source generated by tool-workpiece friction,

B_t is the space occupied by the solid,

B_{tq} is the boundary of it in the thermal analysis, and

N_a and N_b are shape functions.

4.2.5. Material and Friction Models

The work-material model in finite element analysis contains the power-law strain hardening, thermal softening and rate sensitivity (Marusich and Ortiz, 1995). .

In the machining process, very high strain rates may be attained within the primary shear zone, while the remainder of the workpriece deforms at moderate rates. Experimental stress-strain rate curves usually exhibit a transition from low strain rates to high strain rates (Klopp, 1985). In this model, stepwise variation of the rate sensitivity exponent m is used to account for this behavior.

The material behaviors are governed by the following constitutive equations (Marusich and Ortiz, 1995):

$$(1+\frac{\dot{\varepsilon}^p}{\dot{\varepsilon}_0^p})=[\frac{\overline{\sigma}}{g(\varepsilon^p)}]^{m_1} \text{ for } \dot{\varepsilon}^p \le \dot{\varepsilon}_t^p \tag{4.8a}$$

$$(1+\frac{\dot{\varepsilon}^p}{\dot{\varepsilon}_0^p})[1+\frac{\dot{\varepsilon}_t}{\dot{\varepsilon}_0^p}]^{\frac{m_2}{m_1}-1}=[\frac{\overline{\sigma}}{g(\varepsilon^p)}]^{m_2} \text{ for } \dot{\varepsilon}^p \ge \dot{\varepsilon}_t^p \tag{4.8b}$$

$$g(\varepsilon^p)=\sigma_0\theta(T)[1+\frac{\varepsilon^p}{\varepsilon_0^p}]^{\frac{1}{n}} \tag{4.9}$$

where

$\overline{\sigma}$ is the effective Mises stress,

ε^p is the plastic strain,

$\dot{\varepsilon}^p$ is the plastic strain rate,

$\dot{\varepsilon}_0^p$ is a reference plastic strain rate, and

$\dot{\varepsilon}_t$ is the threshold strain rate.

The $\theta(T)$ in Eq. (4.9) is determined by:

$$\theta(T)=C_0+C_1T+C_2T^2+C_3T^3+\cdots \text{ is used for } T \le T_{cut}, \tag{4.10a}$$

$$\theta(T)=\theta(T_{cut})-(\frac{T-T_{cut}}{T_{melt}-T_{cut}}) \text{ is used for } T \ge T_{cut}. \tag{4.10b}$$

where

C_0, C_1,… is the material constants,

T_{cut} is the threshold temperature, and

T_{melt} is the melting temperature.

All parameters are built-in constants in the material database of the software. Because the Young's modulus of WC-Co is much larger than that of Ti-6Al-4V, the deformation of the tool is almost negligible. As a result, the WC-Co tool is assumed to be perfectly elastic. Combined sliding and sticking friction is assumed along the tool-chip interface. Sliding is assumed to occur until a maximum frictional stress is reached, after which sticking occurs and the stress is constant (Stephenson and Agapiou, 2006). The thermal conductivity and heat capacity are assumed to be temperature independent. The properties of CP grade two Ti and Ti-6Al-4V are listed in Appendix I.

4.2.6. Thermo-Mechanical Coupling

During the simulation, staggered mechanical and thermal computations are taken (Marusich and Ortiz, 1995; Shih, 1995). In one time step cycle, based on the initial temperature distribution, the nodal displacement is calculated by Eq. (4.4) and then the distributions of stress and strain are derived. The heat generation is then calculated from the plastic strain energy and friction. With this information, the temperature is recalculated by Eq. (4.7) and used in the material equation Eq. (4.10) to account for thermal softening effect.

4.3. Experimental Setup and Design

Four high-throughput drilling tests of Ti-6Al-4V were simulated. The first experiment, denoted as Exp. D183, was a dry drilling with 183 m/min peripheral cutting speed and 0.051 mm/rev feed. The second experiment (Exp. W183) was conducted at the same peripheral cutting speed and feed with the cutting fluid supplied internally from two through-the-drill holes. Such a cutting fluid supply method has been shown to be important to increase the drill life (Li and Shih, 2007; Trent and Wright, 2000). In the third and fourth experiments (Exps. W91 and W61), the feed was increased to 0.102 and 0.152 mm/rev, and the peripheral cutting speed was reduced to 91 and 61 m/min, respectively, along with using the internal supply of cutting fluid and maintaining the same material removal rate (384 mm^3/s). The drilling depth was 10.2 mm, and drilling time was 2.0 s under all four experimental conditions. The thrust force and torque of each ECT is extracted following the method developed by Ke (2003).

4.4. Results and Discussions

4.4.1. Experimental Validation of Thrust Force and Torque at ECTs

Table 4.1. compares the measured and calculated thrust force, torque, and power for the whole drill. Reasonable agreement can be achieved under most conditions.

Figure 4.2 shows the comparison between the experimentally-measured (solid symbol) and the finite-element-predicted (open symbol) thrust force and torque. The experimental and modeled results show reasonably good agreement in all four experiments. For the thrust force, the discrepancy between experimental and modeled results is less than 27% for all ECTs. The highest discrepancy occurs at the drill center, ECT1. This is probably due to the deflection of workpiece, which makes the full engagement of ECT1 occur later than the theoretical time. High thrust forces occur at ECT1 and ECT2 in drill center due to the negative rake angle at the drill chisel edge (Strenkowski et al., 2004). High torque arises at the ECT6 and ECT7 at the drill periphery. Comparing results in Exps. D183 and W183, at the same 183 m/min cutting speed and 0.051 mm/rev feed, the supply of the cutting fluid does not change the thrust force and torque significantly. Comparing the results of Exps. W183, W91, and W61, with the same material removal rate, the decrease of cutting speed and increase of feed, raises the thrust force and torque.

Table 4.1. Comparison of thrust force, torque, and power of the whole spiral point drill.

Exp.		D183	W183	W91	W61
Thrust force (N)	Exp.	576	621	871	938
	FEM	669	638	977	1114
Torque (N-m)	Exp.	1.94	2.21	2.64	3.10
	FEM	1.98	1.82	3.55	5.08
Power (W)	Exp.	1189	1355	1620	1902
	FEM	1218	1118	2179	3121

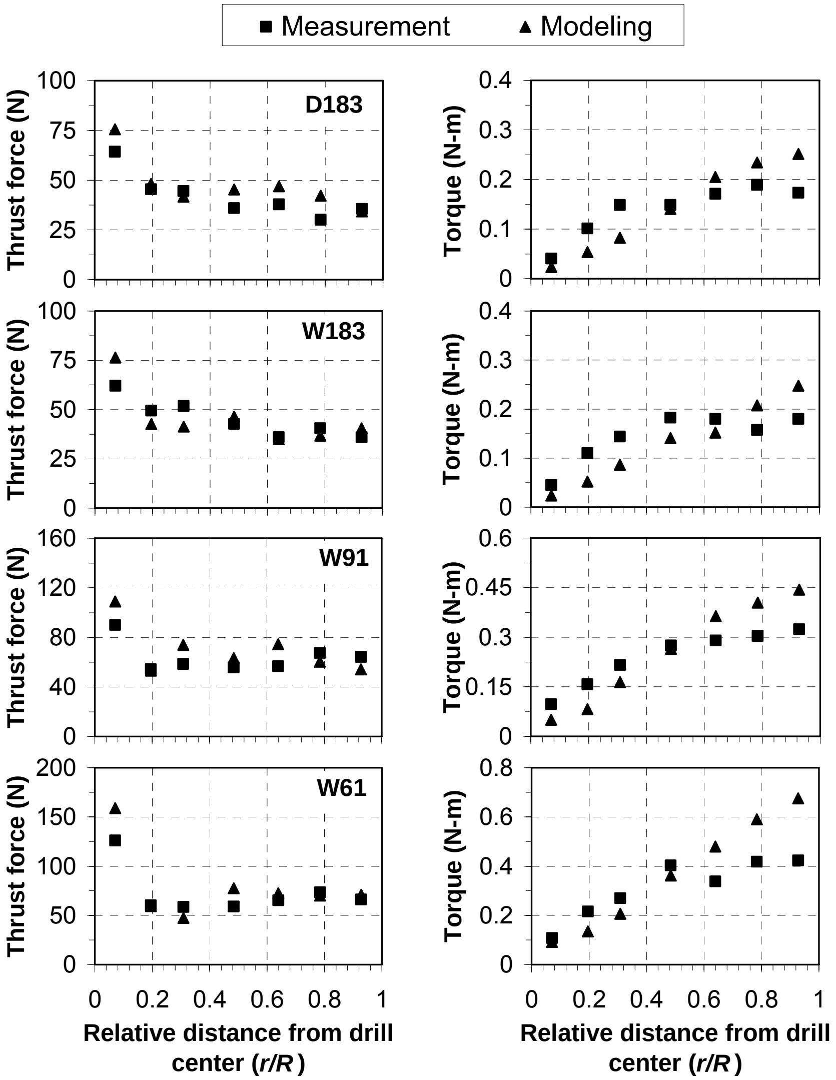

Figure 4.2. Comparison of thrust force and torque of ECTs.

The large discrepancy in torques occurs at ECT2 and ECT3, which are near the transition between the chisel and cutting edges, and ECT6 and ECT7, which are at the periphery of the drill. As shown in Figure 3.6, ECT2 and ECT3 have larger inclination angles than other ECTs. This makes accurate oblique cutting modeling more difficult, and results in higher discrepancies. For ECT6 and ECT7, the torque is overestimated.

This is possibly due to the discrepancy in temperature distributions between the experiments and modeling. In the drilling experiments, due to the high thermal conductivity of the WC-Co tool material, the heat generated at the drill center from the initial contact of the drill and workpiece is transferred to the drill periphery, i.e., ECT6 and ECT7. It results in a high tool and workpiece temperature, softens the workpiece, and reduces the drilling force and torque. In comparison, the tool simulated in FEM is at room temperature when the cutting edges of ECT6 and ECT7 fully engage the workpiece. As a result, the workpiece is harder, yielding a higher torque. Another possible reason for the discrepancy comes from the inaccuracy of both the material and friction modeling. The lack of accurate friction modeling is a limitation in FEM modeling of machining processes (van Luttervelt, 1998).

4.4.2. FEM Prediction of Tool, Workpiece, and Chip Temperatures and Stresses

The cutting situation varies drastically along the ECTs as one moves from the drill chisel edge to the cutting edge. In the drill center (the chisel edge), the cutting speed is close to zero and the work-material is plowed under a high negative rake angle. Along the drill cutting edge, the cutting speed and rake angle both vary with respect to distance from the drill center. The outermost point on the cutting edge has the highest peripheral cutting speed and positive rake angle. This high cutting speed generates very high temperatures, close to the melting temperature of 1600ºC of the Ti workpiece.

The distributions of tool and workpiece/chip temperatures at ECT1, ECT4, and ECT7 at 183 m/min peripheral cutting speed, 0.051 mm/rev feed, and without the cutting fluid are shown in FIGURE 4.3.

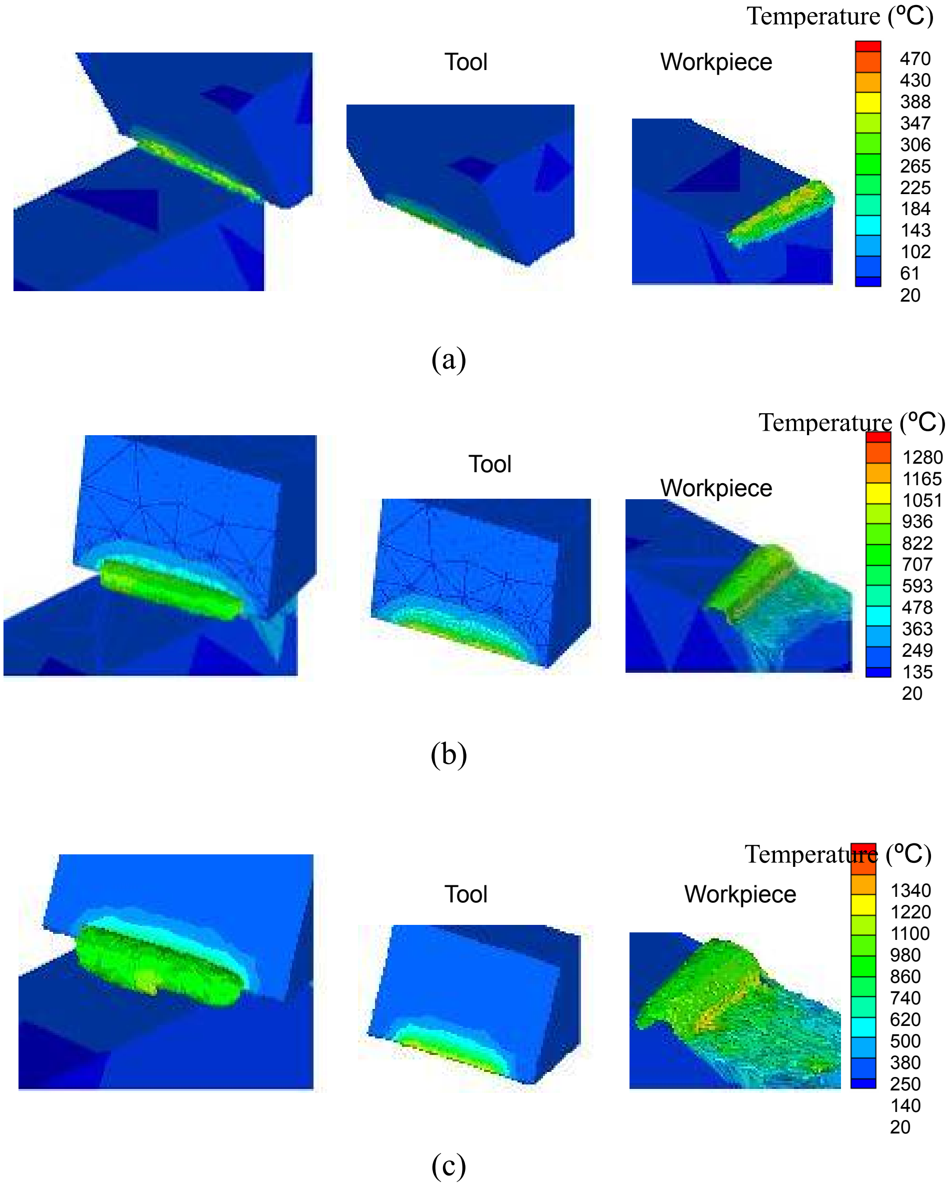
Temperature (ºC)
Tool
Workpiece
470
430
388
347
306
265
225
184
143
102
61
20
(a)
Temperature (ºC)
Tool
Workpiece
1280
1165
1051
936
822
707
593
478
363
249
135
20
(b)
Temperature (ºC)
Tool
Workpiece
1340
1220
1100
980
860
740
620
500
380
250
140
20
(c)

Figure 4.3. Temperature distributions in Exp. D183: (a) ECT1, (b) ECT4, and (c) ECT7.

The peak workpiece/chip temperature at ECT1 is about 470ºC, which is low compared with the 1280ºC and 1340ºC peak temperatures in the ECT4 and ECT7 workpiece/chip. The difference in cutting speeds of 12.9, 88.5, and 169.6 m/min at ECT1, ECT4, and ECT7, respectively, affects the workpiece/chip temperature near the cutting edge. The peak tool temperature, 380ºC in ECT1, 1170ºC in ECT4, and 1240ºC in ECT7, also occurs at the sharp cutting edge. This illustrates the capability of FEM to study the distributions of temperature in the drill.

Analyzing the FEM drilling results, the effect of cutting fluid (Exp. D183 vs. Exp. W183) and reduced cutting speed and increased feed (Exp. W183 vs. Exp. W91 vs. Exp. W61) can be identified, as shown in Figure 4.4. Compared to the temperature results of Exp. D183 (Figure 4.3) under the same cutting speed and feed, the temperature decreases with a cutting fluid supply. In Exp. W183, the peak tool temperatures are reduced to 330ºC, 800ºC, and 1130ºC, and the peak workpiece/chip temperatures decrease to 420ºC, 940ºC, and 1200ºC at ECT1, ECT4, and ECT7, respectively.

Under the same material removal rate, when the cutting speed decreases, the tool temperature also decreases. In Exp. W91, when the cutting speed decreases to 91 m/min, comparing to results of Exp. W183, the tool temperatures decrease to 220ºC, 770ºC, and 1090ºC, and the workpiece/chip temperatures decrease to 280ºC, 890ºC, and 1120ºC at ECT1, ECT4, and ECT7, respectively. When the cutting speed further decreases to 61 m/min in Exp. W61, the tool temperatures decrease to 140ºC, 690ºC, and 960ºC, and the workpiece/chip temperatures decrease to 280ºC, 780ºC, and 1020ºC at ECT1, ECT4, and ECT7, respectively.

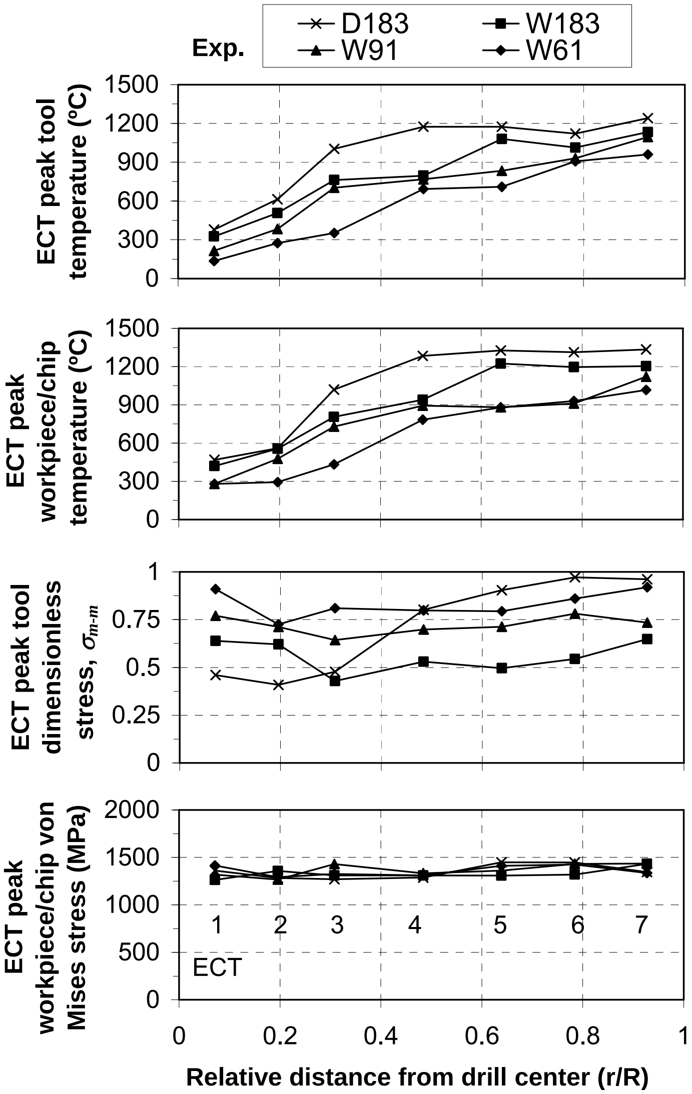

Figure 4.4. Peak temperature and stress distributions at tool and workpiece/chip in Exps. D183-W61.

The stress distributions of ECTs 1-7 in Exps. D183-W61 are also shown in FIGURE 4.4. For the WC-Co tool, the stress is the dimensionless stress according to Modified Mohr criterion, $\bar{\sigma}_{m-m}$ as defined in Chapter 3. For the Ti-6Al-4V workpiece, the stress is von Mises stress. The peak $\bar{\sigma}_{m-m}$ predicted by this model shows a similar trend as the estimation in Chapter 3. In Exp. D183, the maximum $\bar{\sigma}_{m-m}$ is located in the cutting edge because of the high temperature and low tensile and compressive strengths. In all experiments with cutting fluid supply, the $\bar{\sigma}_{m-m}$ at chisel edge is comparable to that at cutting edge because of the lower temperature at cutting edge. Different from the estimation in Chapter 3, the stress at ECT 6 and 7 are high for drilling with cutting fluid supply. This is due to the overestimated torque as in Figure 4.2.

The workpiece/chip stress is about 1250-1400 MPa, independent of the cutting condition. The peak stress is located at the end of the shear zone near the workpiece/chip free surface (away from the cutting tool tip).

4.5. Concluding Remarks

The 3D updated-Lagrangian finite element modeling of high-throughput drilling of Ti-6Al-4V was validated by comparison with experimentally-measured thrust force and torque under four cutting conditions. The discrepancy between experimentally-measured and FEM-predicted thrust forces was less than 27% for the four drilling conditions, and the difference in torque was less than 50%. The comparison with experimentally measured temperature will be conducted in the future work.

FEM was able to show the distributions of stress and temperature in both the drill and workpiece/chip. The peak tool temperature in drilling Ti was high: 1240ºC at 183 m/min cutting speed and 0.051 mm/rev feed under dry condition (Exp. D183) and 1130ºC with the same drilling process parameters and cutting fluid internally supplied through the drill body (Exp. W183). The reduction in cutting speed and increase in feed in Exps. W91 and W61 under the drilling with an internal cutting fluid supply further reduced the peak tool temperature to 1090 and 960ºC and increased the peak drill stress dimensionless stress of the modified Mohr criterion from 0.64 at Exp. W183 to 0.77 and 0.92. The coupled effect of tool temperature and stress was discussed.

The 3D, oblique-cutting-based FEM model developed in this study has limited capabilities and accuracy, and requires further development. The interaction between adjacent segments is neglected in this model. This results in a lack of accuracy in ECT2 and ECT3. To further improve the modeling accuracy, a model treating the whole drill cutting and chisel edges together is under development at ThirdWave Systems. Instead of using a single friction coefficient for the whole rake face, a more complex, stress, strain rate, and temperature-dependent friction model is required to simulate the drilling more closely. This study can also be expanded for the drill selection, drill geometry design, and optimization of drilling process parameters to further enhance the productivity of drilling Ti and other advanced engineering materials.

CHPATER 5

METALLURGICAL ANALYSIS AND NANOINDENTATION CHARACTERIZATION OF TI-6AL-4V WORKPIECE AND CHIPS IN HIGH-THROUGHPUT DRILLING

The metallurgical analyses, including SEM, XRD, electron microprobe, and nanoindentation characterization are conducted to study the Ti-6Al-4V hole surface and subsurface and the chips in high-throughput drilling tests. The influence of high temperature, large strain, and high strain rate deformation on the β phase decomposition and mechanical properties is investigated. Diffusionless β phase decomposition in the subsurface layer adjecent to the hole surface can be observsed in dry drilling, but not in other drilling conditions with the supply of cutting fluid. Nanoindentaion tests identify a 15~20 μm high hardness subsurface layer with peak hardness over 9 GPa, relative to the 4~5 GPa bulk material hardness, adjecnt to the hole surface in dry drilling,. For drilling chips, the β phase is retained under all conditions tested due to rapid cooling. On the chips, the saw-tooth feature and narrrow shear bands are only formed at the outmost edge and no significant change of hardness across the shear bands can be found in nanoindentation.

5.1. Introduction

Ti-6Al-4V is a two-phase alloy. An example of the microstructure of the Ti-6Al-4V used in this study is shown in Figure 5.1. The dark region is α phase and the light region is β phase.

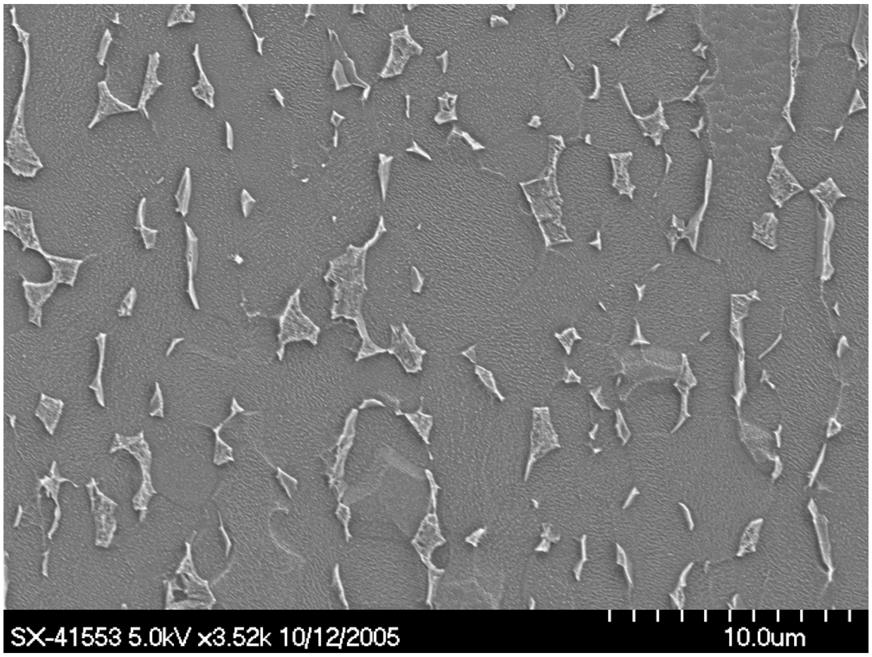

Figure 5.1. SEM micrograph of an etched microstructure of Ti-6Al-4V with dark region for HCP α phase and light region for BCC β phase.

In high-throughput drilling of Ti-6Al-4V, the workpiece and chips undergo large deformation at high strain rate and temperature, which can alter the microstructure and material properties of the Ti work-material and chips. The high temperature and the following cooling process may cause the β phase decomposition, usually by martensitic transformations to α' or α''. Bayoumi and Xie (Bayoumi and Xie, 1995) reported the disapperance of β phase in scanning electron microscopic (SEM) and X-ray diffraction (XRD) study of Ti-6Al-4V chips generated in turning. Cantero et al. (2005) reported the formation of an "α case" where the β phase is absent adjacent to the hole surface in the dry drilling of Ti-6Al-4V. In high-throughput drilling, the temperature is higher and plastic deformation is more severe than drilling at lower speed and feed rate. One of the goals of this reserach is to gain better understanding of the phase transformation on surface and subsurface layer of the hole and chip in high-throughput drilling of Ti-6Al-4V.

The change of V concentration due to diffusion has been reported as another cause of the phase transformation in the subsurface layer adjacent to the hole surface in deep-hole drilling of Ti-6Al-4V at a relatively low feed rate, 0.04 m/min (Reissig, 2004). In this study, the feed rate of high-throughput drilling is much higher, 0.75 m/min. Since the drilling time is short, diffusion is unlikely to occur. However, the change in V concentration is investigated in this study.

Mechanical properties in the hole subsurface can be affected by the combination of phase transformation, thermal softening, and strain hardening during drilling. This layer is usually called the subsurface layer (Machado and Wallbank, 1990; Mantle and Aspinwall, 2001) or deformed layer (Che-Haron, 2001) underneath the machined surface. The microhardness evaluation of the cross-section of drilled Ti-6Al-4V holes by Cantero et al. (2005) found a 125 μm thick hardened subsurface layer. High-throughput drilling is expected to create a narrower subsurface layer due to the short drilling time. Microhardness testing is not adequate and nanoindentation evaluation is utilized.

Serrated or saw-tooth type chips are generated in Ti machining. Most of researchers attributed the adiabatic shear band formation for the observed serrated chips

(Shaw et al, 1954; Komanduri and Von Turkovich, 1981; Komanduri, 1982; Xie, 1996; Sheikh-Ahmad and Bailey, 1997; Barry et al., 2001; Komanduri and Hou, 2002). Nakayama (1974) and Vyas and Shaw (1999) proposed that the crack initiated at the chip free face was the cause of serrated chip formation. Sheikh-Ahmad et al. (2004) combined these two theories and suggested that flow instability and shear band formation caused the saw tooth formation at high cutting speed, while at low cutting speed, the cracking followed by shear localiztion dominated. The high temperature and shear strain concentrated in the shear bands are expected to influence the mechanical properties. High hardness across the shear band was reported by Sheikh-Ahmad et al. in turning of commercially pure (CP) Ti (Sheikh-Ahmad et al., 2004). Until now, most studies of Ti machinig chips were constrained to orthogonal cutting in which the cutting conditions were constant along the tool cutting edge. Drilling has a more complicated material removal process. During the chip formation in drilling, the cutting speed and rake angle vary along the cutting edge of the drill. As a result, complicated chip morphology at different stages of chip formation process is created. The chip morphology and the associated changes in material properties are investigated in high-throughput drilling of Ti-6Al-4V.

In this study, metallurgical studies, including SEM, XRD, electron microprobe, and nanoindentation tests were conducted. Changes in microstructure, phase, chemical composition, and mechnical properties are dicussed on the drilled hole surface, subsurface layer, and drilling chips.

5.2. Experimental Setup

5.2.1. Sample Preparation

Four high-throughput drilling conditions, marked as Exp. D183, W183, W91, and W61 as in Secs. 3 and 4, were analyzed. After drilling, each specimen was cut in half axially along each drilled hole, as shown in Figure 5.2(a). One of the sectioned specimens was metallographically mounted in epoxy potting and then polished with fine diamond compound for nanoindentation testing and chemical composition analysis. After nanoindentation, the specimens were etched with a solution containing 6 ml HNO_3 and 3 ml HF in 100 ml H_2O to distinguish the α and β phase structure of Ti-6Al-4V in the SEM. The other sectioned specimen was used for XRD. An original Ti-6Al-4V bulk material was also polished and etched to extract the α–β phase information in SEM and for XRD evaluation. The chips, as shown in Figure 5.2(b), were cleaned by acetone, metallographically mounted in epoxy, and sectioned and polished for nanoindentation testing and SEM study.

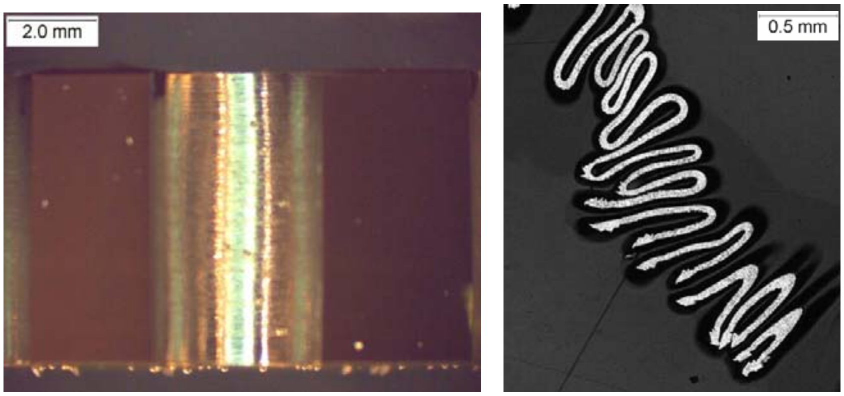

(a) (b)

Figure 5.2. Macroscopic pictures of the Ti-6Al-4V specimen: (a) hole cross-section and (b) chip.

5.2.2. SEM Microstructure Observations

The polished and etched hole and chip cross-sections were examined by a Hitachi S-4700 SEM to identify the α–β phase.

5.2.3. Quantitative Analysis of Phase Content by XRD

As shown in Figure 5.3, a PANalytical XPERT-PRO MPD X-ray diffractometer with Cu tube (generator setting: 40 mA, 45 kV) and proportional detector was used with parallel beam optics, incident parabolic multilayer mirror and diffraction-side 0.09° radial divergence limiting slits, to examine the phase transformation of α–β phase on the cylindrical surfaces of the machined hole. Parallel beam optics were employed to eliminate sample surface displacement effects (Watkins et al., 2003). The beam width was confined to be less than the hole diameter in order to obtain signal from the cylindrical surfaces only. The scan rate was 15 s/step.

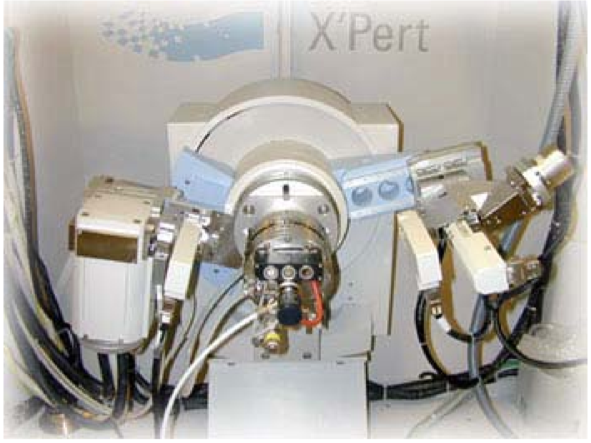

Figure 5.3. PANalytical XPERT-PRO MPD X-ray diffractometer

The Rietveld method (Young, 1995) was utilized for the quantitative XRD analysis of the α–β phase fraction using X'Pert HighScore Plus^{TM} software made by PANalytical. The scan profile is refined with least squares fitting (Young, 2005):

$$S_y = \sum_i w_i (y_i - y_{ci})^2 \tag{5.1}$$

where w_i (=1/y_i), and y_i and y_{ci} are observed and calculated intensities of the spectrum pattern lines at the ith step, respectively. The calculated intensities y_{ci} are represented as:

$$y_{ci} = s \sum_k L_k |F_k|^2 \phi(2\theta_i - 2\theta_k) P_k A + y_{bi} \tag{5.2}$$

where s is the scale factor, k represents the Miller indices, L_k contains the Lorentz polarization, and multiplicity factors, F_k is the structure factor for the kth Bragg reflection, ϕ is the reflection profile function, $2\theta_i$ is the measured position at the ith step, $2\theta_K$ is the calculated positions of the Bragg peak, P_K is the preferred orientation function, A is an absorption factor, and y_{bi} is the background intensity at the ith step.

5.2.4. Analysis of Chemical Composition by Electron Microprobe

Wavelength dispersive spectroscopy was used to detect the possible changes in chemical composition, especially the Al as α stabilizer and V as β stabilizer, using a JEOL 8200 electron microprobe. Spectra taken from a region less than 10 μm from the edge of the hole surface were compared with those taken from a region far away from the hole surface.

5.2.5. Nanoindentation Characterization of Mechanical Properties

The subsurface regions adjacent to the hole surface and the chips were narrow, only a few μm wide. Nano-indentation using the Hysitron triboindenter™ (by Hysitron Inc., as shown in Figure 5.4 was applied to investigate mechanical properties of the subsurface layer adjacent to the hole surface. Array of indents were made along the direction parallel and perpendicular to the hole axis. The spacing between each indent was 5 to 12 μm. For each indent, the applied load was 2 mN. A MTS Nano-indenter™ W183 was used for chips. To investigate the influence of shear bands on mechanical properties, nanoindentation was conducted on the chips with distinct saw tooth formations. For each indent, the displacement of the indenter was 150 nm. For both machines, Berkovich diamond indenters were used. The area of indents was less than 1 μm². The hardness, *H* is calculated as follows (Oliver and Pharr, 1992; Qu et al., 2003):

$$H = \frac{P_{\max}}{A} \tag{5.3}$$

where P_{max} is the peak indentation load, A is the projected area of the contact at peak load evaluated from the shape function of the indenter and the maximum indent displacement.

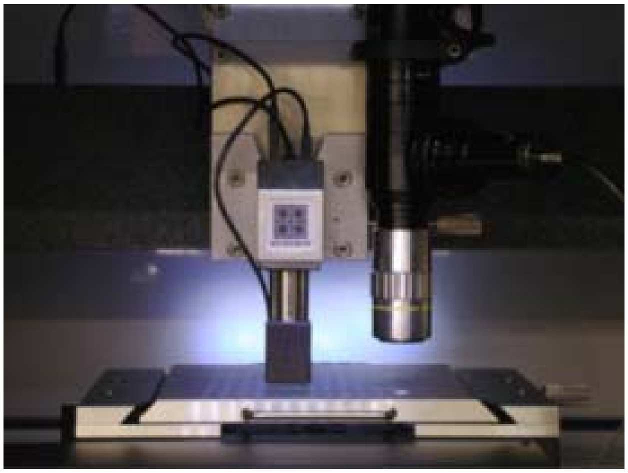

Figure 5.4. Hysitron triboindenter^{TM}.

5.3. Metallurgical Analysis of Hole Surface and Subsurface Layer

5.3.1. Microstructural Observations

Figure 5.5 shows the SEM micrographs of the hole cross-section of Exp. D183. As shown in Figure 5.5(a), there is a 10~15 μm thick subsurface layer next to the hole surface. In this layer, there is a gradation of distinct grain boundaries between α and β phases to indiscernable ones from the bulk toward the hole surface. Figure 5.5(b) shows the high magnification micograph of the bulk material. Both large and tiny β grains can be observed among the α phase. At the transitional region between the bulk and subsurface layer, as shown in Figure 5.5(c), large β grains are still observable, but most tiny β grains dissapear and transform to martensites which have acicular or needle-like shape. This phase transformation is a result of high temperature above β transus temperature and subsequent fast cooling by conduction into bulk. In the machining influenced subsurface layer as shown in Figure 5.5 (d), even large β griains dissappear.

The whole layer is distributed with martensitic grains, but grains are equiaxed, as a result of plastic deformation by rubbing between the drill and hole surface. Because the drilling time is short, the heat affected zone is significantly narrower than 125 μm observed in drilling at lower peripheral cutting speed (50 m/min) (Cantero et al., 2005).

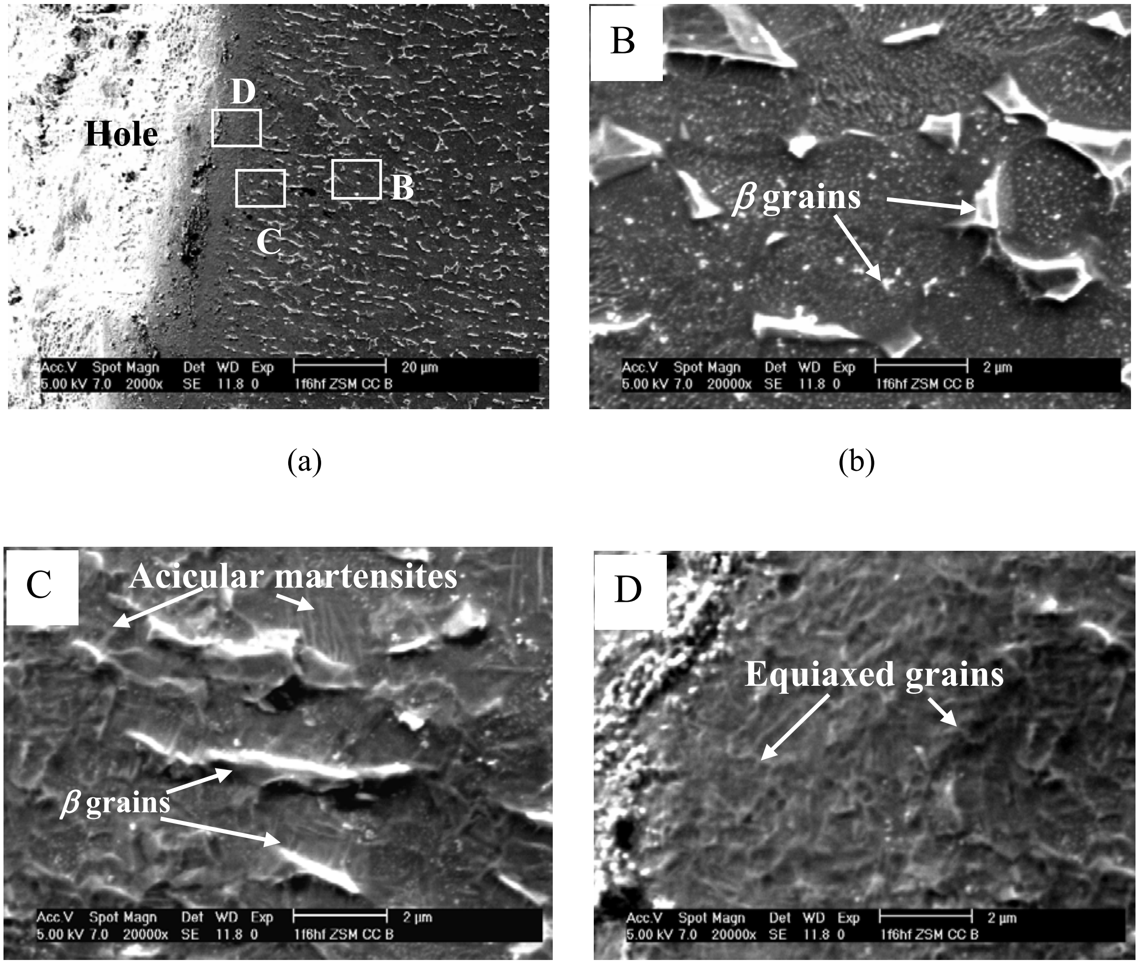
Hole
D
C
B
Acc.V Spot Magn Det WD Exp 20 μm
5.00 kV 7.0 2000x SE 11.8 0 1f6hf ZSM CC B
B
β grains
Acc.V Spot Magn Det WD Exp 2 μm
5.00 kV 7.0 20000x SE 11.8 0 1f6hf ZSM CC B
C
Acicular martensites
β grains
Acc.V Spot Magn Det WD Exp 2 μm
5.00 kV 7.0 20000x SE 11.8 0 1f6hf ZSM CC B
D
Equiaxed grains
Acc.V Spot Magn Det WD Exp 2 μm
5.00 kV 7.0 20000x SE 11.8 0 1f6hf ZSM CC B

(a) (b)

(c) (d)

Figure 5.5. SEM micrographs of the polished and etched cross-sections of drilled holes in Exps. D183 (dry): (a) hole, subsurface, bulk material, (b) bulk material, (c) transition layer, and (d) subsurface layer.

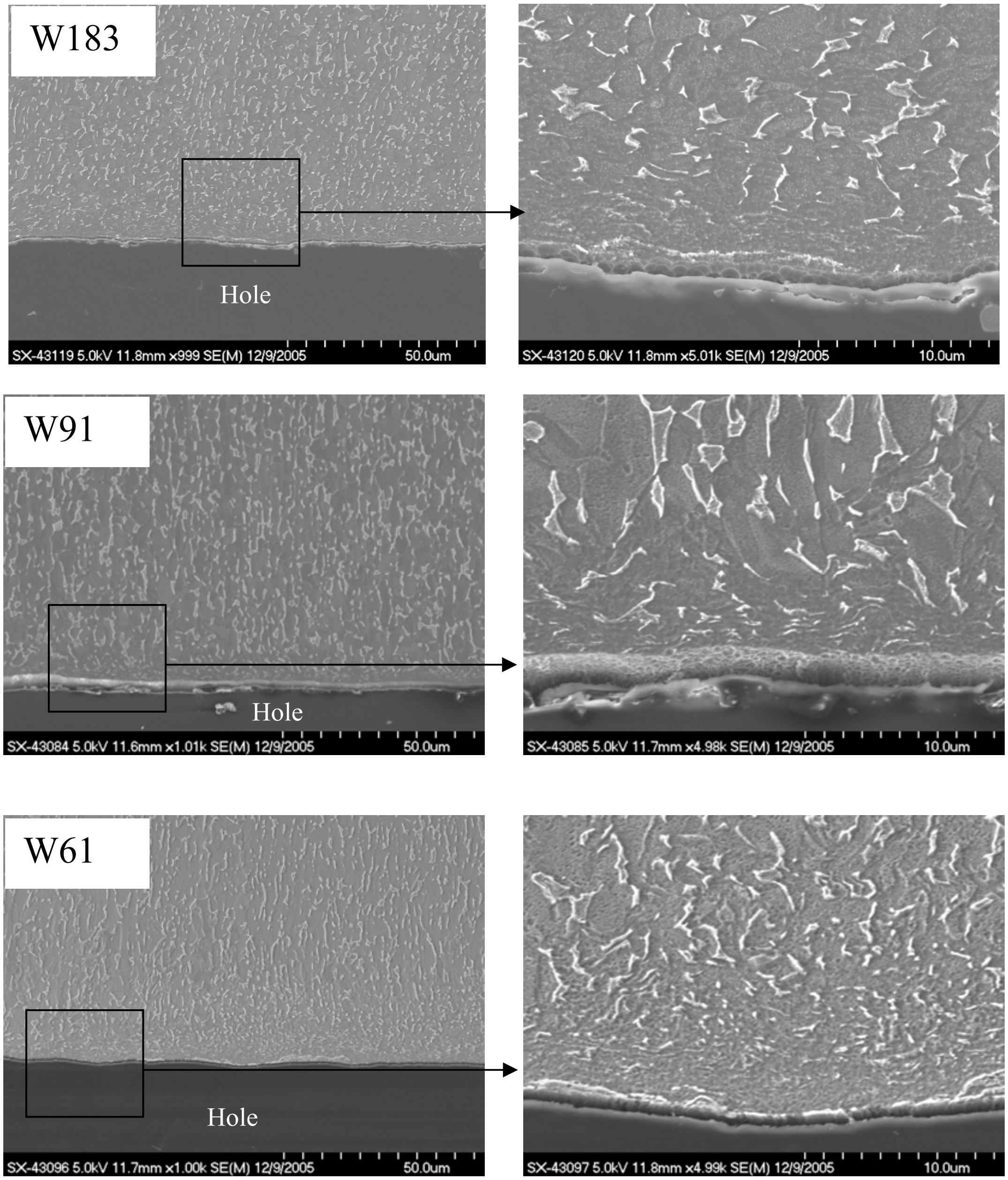
W183
Hole
SX-43119 5.0kV 11.8mm x999 SE(M) 12/9/2005 50.0um
SX-43120 5.0kV 11.8mm x5.01k SE(M) 12/9/2005 10.0um
W91
Hole
SX-43084 5.0kV 11.6mm x1.01k SE(M) 12/9/2005 50.0um
SX-43085 5.0kV 11.7mm x4.98k SE(M) 12/9/2005 10.0um
W61
Hole
SX-43096 5.0kV 11.7mm x1.00k SE(M) 12/9/2005 50.0um
SX-43097 5.0kV 11.8mm x4.99k SE(M) 12/9/2005 10.0um

Figure 5.6. SEM micrographs of the polished and etched cross-sections of drilled holes with cutting fluid supply (Exps. W183-W61).

Fig. 5.6. shows the Exps. W183-W61, which have the same drilling peripheral cutting speed and feed per revoluation as Exp. D183. In Exp. W183, the β structure is obseravable at regions very close to the hole surface, primarily due to two reasons: less phase transformation above β transus temperature and the following β phase decomposition as a result of a decreased cutting temperature with internal cutting fluid supply. The subsurface layer is about only 3 μm. As shown in the high magnification micograph, the grain structure within the subsurface layer is elongated parallel with the hole edge, indicating the severe plastic deformation. The micrographs of Exps. W91 and W61 showed similar features and dimensions as those in Exp. W183.

5.3.2. Quantitative XRD Analysis of Phase Transformation

X-ray diffraction analysis results of as-polished bulk material and drilled hole surface of Exp. D183 are shown in Figure 5.7. The X-ray diffraction pattern of the as-polished bulk material shows the BCC β phase has a (110) preferred orientation/texture. The HCP α phase is also textured on the (100) and (002) planes.

In Exp. D183 (dry drilling), compared to the pattern of as-polished bulk material, the α peaks are clearly broader due to the decreased size of crystallite and likely rms strains (i.e. nanostrains) (Cullity, 1978), resulting from the severe plastic deformation in the subsurface layer. Drilling process also changes the original texture and makes the α crystallites in the material more randomly distributed. The peaks corresponding to α (100) and (200) planes are weakened relative to the (101) planes. All peaks corresponding to β phase disappear. Because the most prominent changes are concentrated in the range of 30° and 45° 2θ diffraction angle, the close-up view of the XRD patterns along with the fitted profiles of the bulk material and four drilled hole surfaces of Exps. D183-W61 are shown in Figure 5.8 for mutual comparison.

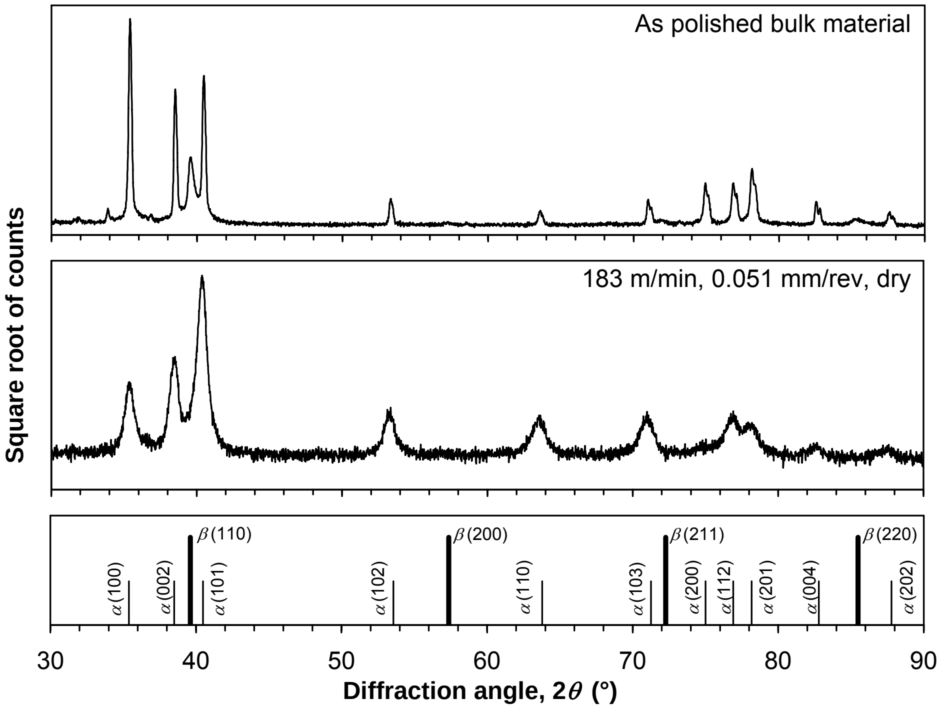

Figure 5.7. X-ray diffraction patterns of the as-polished bulk material and hole surface of Exp. D183 (intensity plotted as square root of counts to help distinguish the weak peaks from the background).

Quantitative analysis by Rietveld method shows 7.3% *β* in the bulk material, as labeled in Figure 5.8. In Exp. D183, the *β* is reduced to 0%. The x-ray penetration depth is estimated to vary from 4 to 12 μm at 30 to 90° 2θ, respectively, for 95% of the total diffraction intensity. There are two possible causes for the disappearance of *β* peaks. The main cause is the transformation of a large portion of the *β* to martensite phase. The other cause is that the residual broadened *β* peaks are submerged by broadened neighboring *α* peaks and become indiscernible.

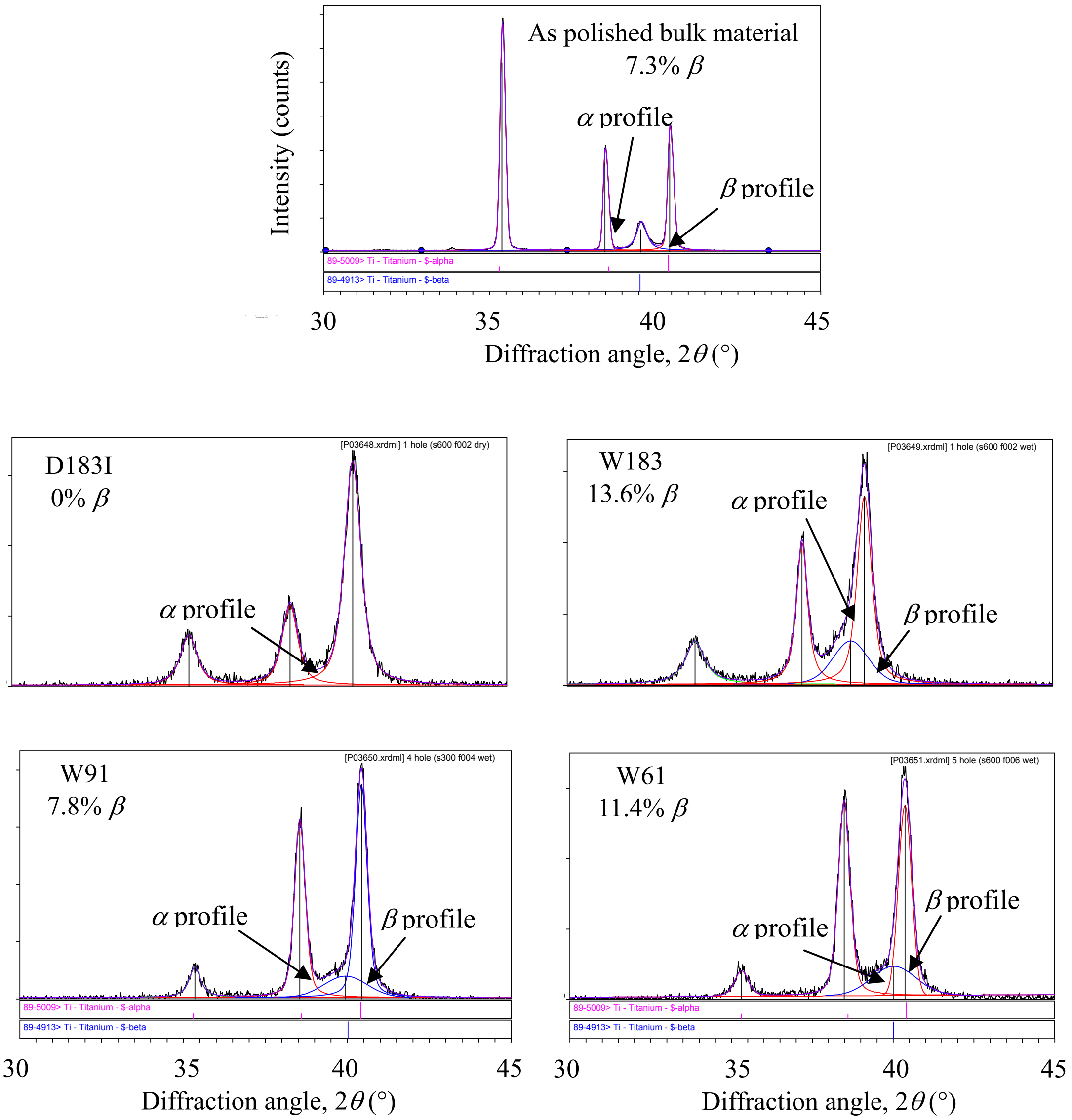

Figure 5.8. X-ray diffraction spectra of as polished bulk material and hole edge of Exps. D183-W61 and calculated profiles from 30° to 45° diffraction angle.

The amount of β phase increases to 13.6, 7.8, and 11.4% with the introduction of cutting fluid for Exps. W183-W61, respectively. These values are higher than the 7.3% β phase in the bulk material and indicates that only a small amount, if any, of the β phase transformed to α on the hole surface during drilling due to the better cooling with cutting fluid. Because of the broadened α peaks, the peaks corresponding to β are not obvious in XRD patterns of Exps. W183-W61 as in Figure 5.8. Since only one or two tests were conducted for each hole, quantitative results may not be determinative, but the difference between Exps. D183 and W183 is manifested.

5.3.3. Chemical Composition Analysis

The Al and V contents were measured at seven points randomly chosen within a region less than 10 μm from the hole surface and seven points in the region far from the hole surface (i.e., the bulk) in Exps. D183 and W183. For comparison, the Al and V contents were also measured in the bulk material.

Table 5.1 summarizes results of average and standard deviation of the Al and V contents. No statistically significant change of Al and V composition can be observed between regions close to and far away from the hole surface, which supports the hypothesis that the β phase decomposition under dry drilling condition is a diffusionless transformation (the transformation without chemical composition change).

Table 5.1. Comparison of Al and V content in the chemical analysis of cross-sectional subsurface layer (within 10 μm from the hole surface) in Exps. D183 and W183 and the bulk material.

	Bulk		Exp. D183		Exp. W183	
	Avg	Std	Avg	Std	Avg	Std
Al (%)	6.7	0.3	6.7	0.6	6.5	0.2
V (%)	4.0	0.8	4.1	0.1	4.1	0.5

The same diffusionless transformation for the decompostion of β phase is also observed in the heat treatment of Ti-6Al-4V (Donachie, Jr., 1988). Any β phase decomposition is more likely due to the high temperature. This matches with the same conclusion observed in turning of Ti-6Al-4V (Bayoumi and Xie, 1995) but is different from the result reported in (Reissig et al., 2004) for drilling of Ti-6Al-4V at low feed rate.

5.3.4. Nanoindentation Hardness

Figure 5.9 shows the nanoindents and associated hardness values of the hole cross-section in Exp. D183, which has a 15 to 20 μm subsurface layer of almost 0% β phase (Figure 5.5). Figure 5.9(a) shows a matrix of indents in directions roughly parallel and perpendicular to the hole axis. The spacing between each indent is about 8 to 12 μm. Another set of nanoindentations with a line of nanoindents close to the hole surface is shown in Figure 5.9(b). Higher hardness values are found at indents closer to the hole surface. Adjacent to the hole surface, the hardness can reach 10.0 GPa. All indents are under the same 2 mN load.

Two load-displacement curves at indent A with low (5.2 GPa) hardness and at indent B with high (9.7 GPa) hardness are shown in Figs. 5.9(c) and (d), respectively. Indent A has larger displacement which indicates larger area at peak load.

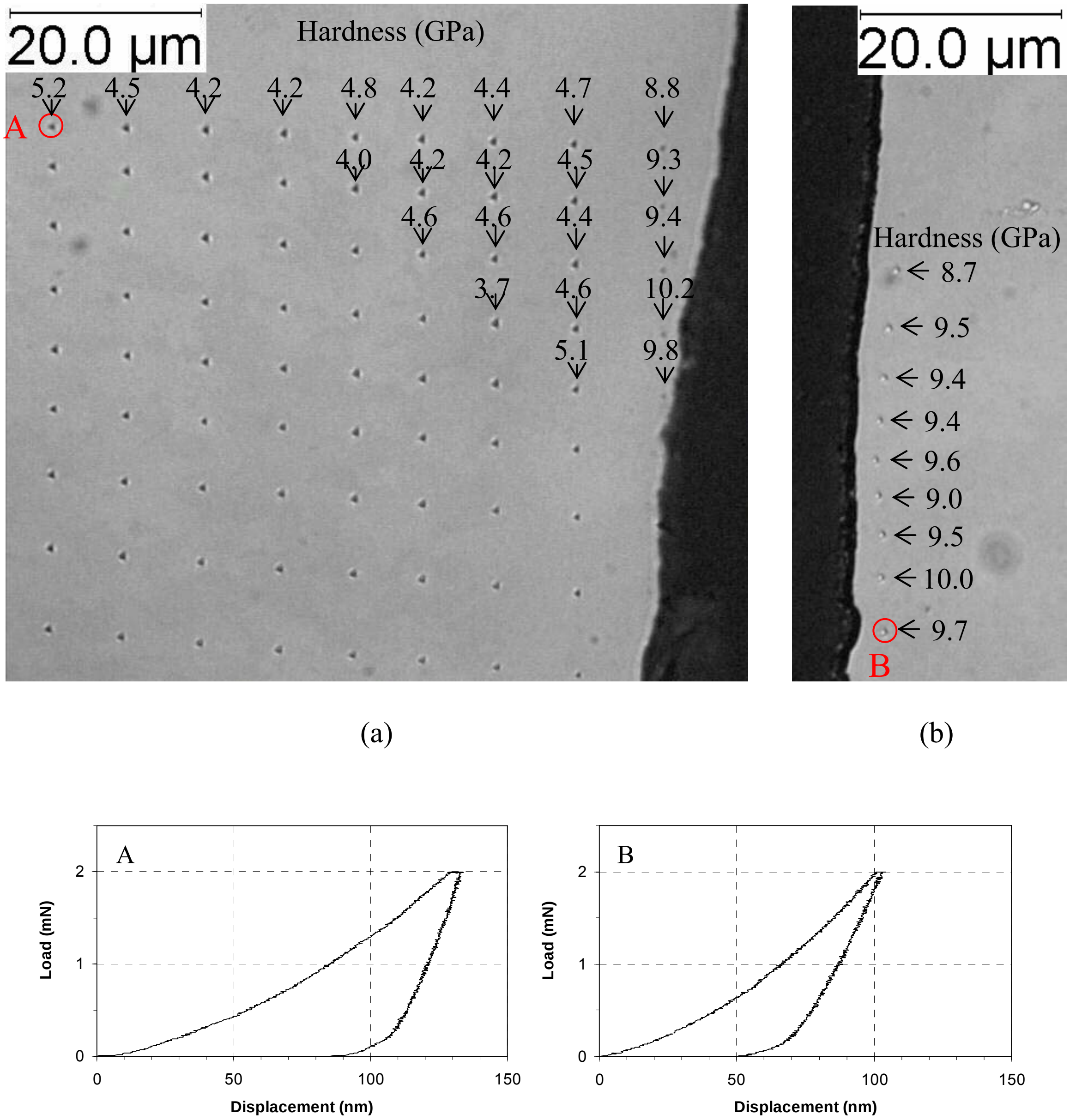

(a) (b)

(c) (d)

Figure 5.9. Nanoindentation on the workpiece cross-section in Exp. D183: (a) array of indents, (b) indents close to the hole edge, (c) load-displacement curve of indent A away from hole edge, and (d) load-displacement curve of indent B close to the hole edge.

Figure 5.10 compares the nanoindentation hardness, *H*, vs. distance from the hole surface in Exps. D183-W61. The layer of high hardness exists in all conditions, but the extent and the depth of high hardness layer are different. The highest hardness exists under the dry drilling condition in Exp. D183. At the reigon less than 5 μm from the hole surface, the hardness is over 8 GPa, which is about twice the hardness measured in the bulk. The high hardness layer is about 15 to 20 μm wide, which is in reasonable agreement with the microstructural observations of Exp. D183 as in Figure 5.5. The thickness of hardened layer is significantly narrower than prior results observed in drilling at moderate speed (Cantero et al., 2005) and demonstrates a benefit of high-throughput drilling. The existence of this hardened layer is the result that high strain rate plastic deformation outweighs the thermal softening. The high temperature β phase decomposition as stated in Sec. 3.2 may also contribute to the formation of this layer (Machado and Wallbank, 1990; Cantero, 2005) . Beyond this layer, the hardness is stablized around 4.1 to 5 GPa.

When the cutting fluid is supplied at the same cutting speed and feed (Exp. W183), the peak hardness reduces to 5 to 5.5 GPa in the subsurface layer close to the hole edge. This hardness is only slightly higher than that of the bulk material. The thickness of hardened layer is also reduced to between 5 to 15 μm. Relative to the results of Exp D183, the benefit of cutting fluid to lubricate the tool-chip interface and reduce the temperature and plastic deformation on the hole surface is apparent.

For Exps. W91 and W61, no significant change in the hardenss profile from Exp. W183 was observed. The peak hardness remains in the range of 5 to 5.5 GPa as in Exp. W183. The thickness of machining affected layer are about 5 μm, which is smaller than that of Exp. W183. The decrease of layer thickness is possibly the result of smaller plastic deformation and a lower strain hardening effect at high feed and lower cutting speed.

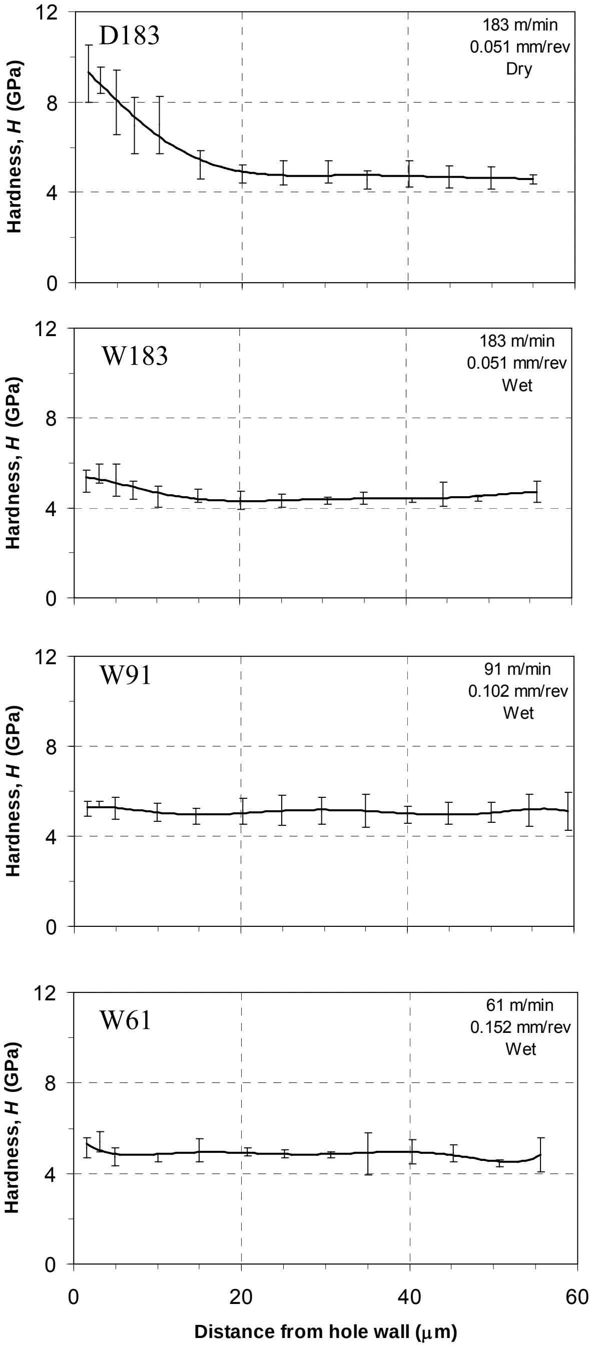

Figure 5.10. Nanoindentation hardness profile of subsurface adjacent to the hole edge in Exps. D183-W61.

5.4. Drilling Chips

In Sec. 5.3, significant differences in hardness and depth of subsurface layer are observed between dry drilling (Exp. D183) and drilling with supply of cutting fluid (Exp. W183) at 183 m/min high cutting speed and 0.051 mm/rev feed. With the supply of cutting fluid, different cutting speeds and feeds in Exps. W183 to W61 do not influence the product quality metallurgically As a result, only chips in Exps. D183 and W183 are investigated.

5.4.1. Chip Morphology

As discussed in Section 2.7, in all Ti-6Al-4V drilling experiments in this study, the spiral point drill generates the same chip morphology: a continuous chip with spiral cone followed by folded long ribbon. An example of the chip generated in Exp. D183 is shown in Figure 2.10.

Serrated chip formation with the saw-tooth shape surface is commonly observed in orthogonal turning of Ti alloys (Mantle and Aspinwall, 2001; Che-Haron, 2001; Shaw et al, 1954; Komanduri and Von Turkovich, 1981; Komanduri, 1982; Xie, 1996; Sheikh-Ahmad and Bailey, 1997). Surprisingly, as shown in Figure 5.11, the saw tooth is not a common feature on the chip surface in high speed drilling of Ti-6Al-4V. As labeled as the point F in Figure 5.11(a) and magnified in Figure 5.11(b), the saw teeth can be seen only at the outmost edge of the chip. This region is generated by the outmost point on the drill cutting edge. This saw teeth region is less than 50 μm from the chip edge. It is only a very small part of the whole chip.

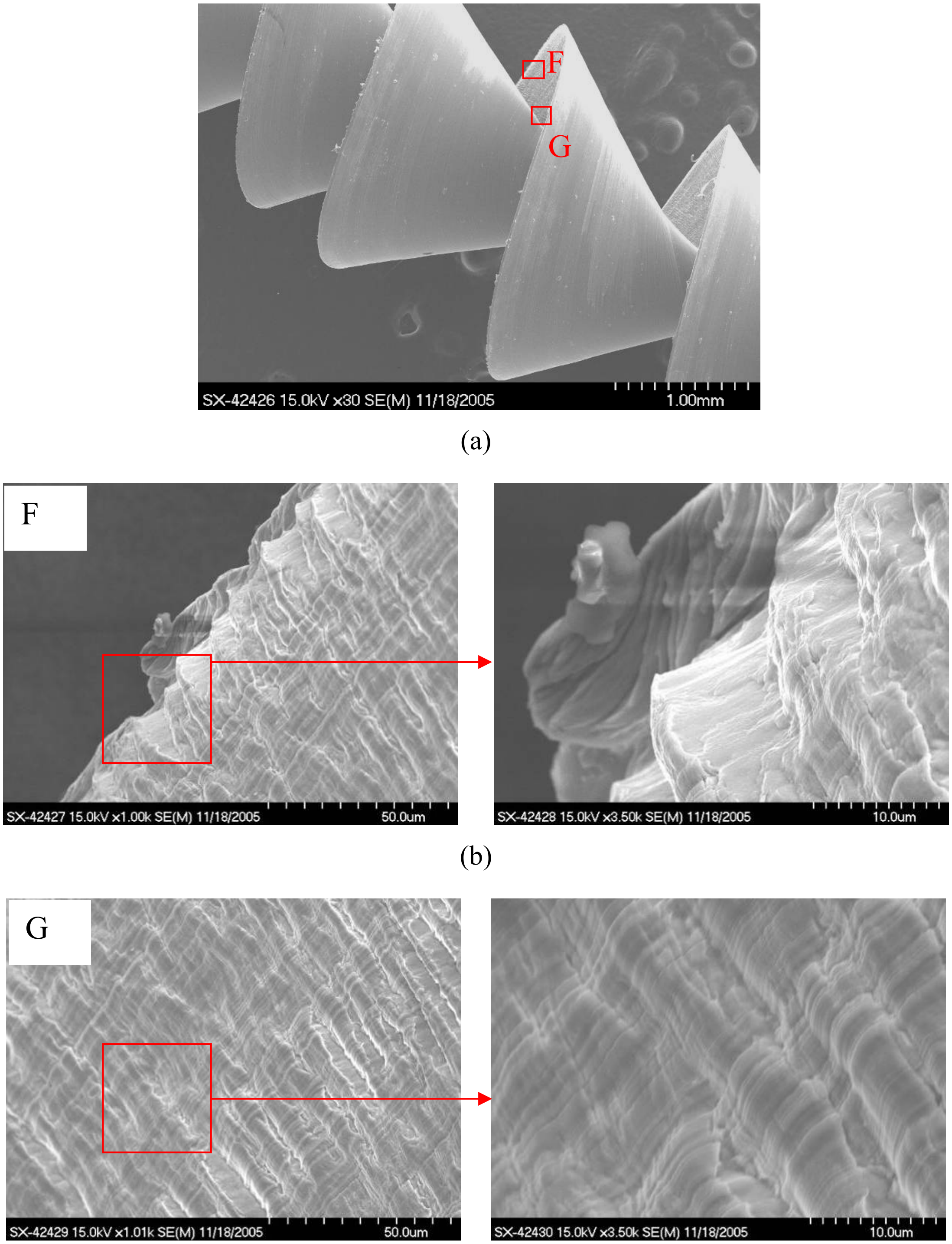
F
G
SX-42426 15.0kV x30 SE(M) 11/18/2005
1.00mm
F
SX-42427 15.0kV x1.00k SE(M) 11/18/2005
50.0um
SX-42428 15.0kV x3.50k SE(M) 11/18/2005
10.0um
G
SX-42429 15.0kV x1.01k SE(M) 11/18/2005
50.0um
SX-42430 15.0kV x3.50k SE(M) 11/18/2005
10.0um

(a)

(b)

(c)

Figure 5.11. SEM micrographs of chip morphology in Exp. D183: (a) spiral cone chip, (b) outer edge of the chip, and (c) inner side of the chip.

Other than this narrow region, the saw tooth formation becomes indiscernible.

The free surface on the chip degrades to lamellae (Barry et al., 2001), as shown by an example point G in Figs. 5.11(a) and its close-up view in Figure 5.11(c). This observation is different from Ti chips formed in turning (Mantle and Aspinwall, 2001; Che-Haron, 2001; Shaw et al, 1954; Komanduri and Von Turkovich, 1981; Komanduri, 1982; Xie, 1996; Sheikh-Ahmad and Bailey, 1997). Contrary to the orthogonal cutting, chips in drilling are not generated uniformly along the cutting edge. The rake and inclination angles as well as the cutting speed vary along the drill cutting edge. Near the center of the drill, the strain rate is low, where plowing of the work-material occurs. The strain rate and cutting parameters in this region are not likely reaching the critical cutting condition to initiate the chip saw teeth formation. This and the continuously changing cutting conditions along the drill cutting edge likely inhibit the serrated chip formation in drilling of Ti-6Al-4V. At the outmost region of the drill cutting edge, the chip is less affected by the changing cutting speed and tool geometry. This can explain the saw teeth formation in this narrow region.

Figure 5.12(c) shows the close-up view of the chip free edge in Exps. D183 and W183, as marked by H and J in Figs. 5.12(a) and 5.12(b), respectively. The narrow shear bands initiate from the valley of saw-tooth chips are observed in both drilling conditions. The grain structures are elongated along the both sides of shear bands, clearly identifying the severe plastic shear deformation.

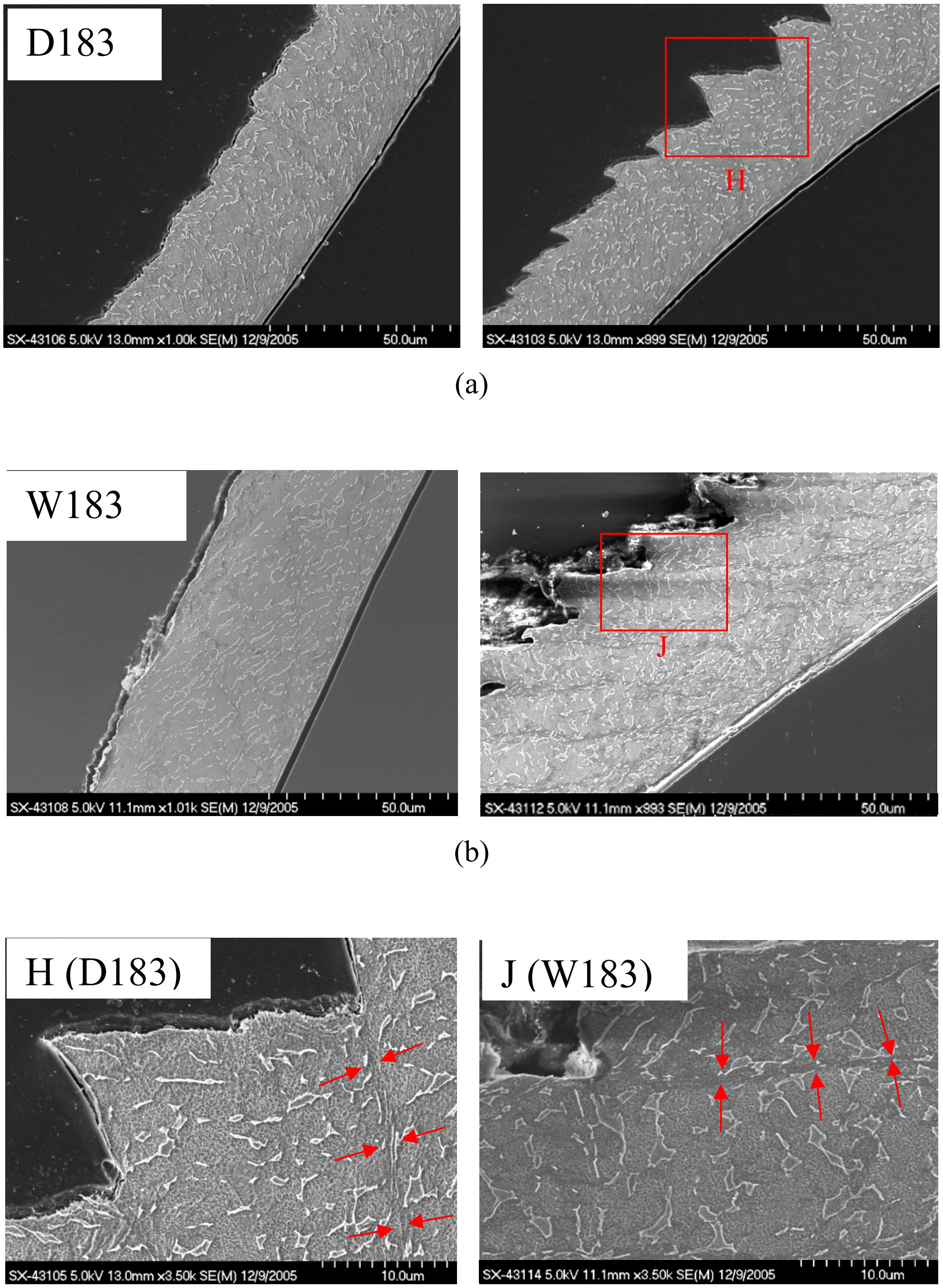
D183
SX-43106 5.0kV 13.0mm x1.00k SE(M) 12/9/2005
50.0um
H
SX-43103 5.0kV 13.0mm x999 SE(M) 12/9/2005
50.0um
W183
SX-43108 5.0kV 11.1mm x1.01k SE(M) 12/9/2005
50.0um
J
SX-43112 5.0kV 11.1mm x993 SE(M) 12/9/2005
50.0um
H (D183)
SX-43105 5.0kV 13.0mm x3.50k SE(M) 12/9/2005
10.0um
J (W183)
SX-43114 5.0kV 11.1mm x3.50k SE(M) 12/9/2005
10.0um

(a)

(b)

(c)

Figure 5.12. SEM micrographs of chips in: (a) Exp. D183 (dry drilling), (b) Exp. W183 (internal cutting fluid supply), and (c) close-up view of regions H (Exp. D183) and J (Exp. W183).

5.4.3. Nanoindentation hardness

Nanoindention on the chip cross-sections was conducted before etching to minimize the influence of chemical etching. The thermal softening and strain hardening are two competing factors which determine the hardness of an indent in the chip. Figure 5.13(a) shows an example of indents on a chip before etching. The spacing between each indent was about 5 μm.

After indentation, the sample was etched to expose the crystal structure and determine if the indent is close to the shear band. An example of etched chip sample is shown in Figure 5.13(b). Two indents close to the shear band are marked by circles in Figure 5.13(b). There is no significant difference of hardness between these two and other indents.

Over 140 and 60 indents were made in a similar configuration on the saw-tooth chip cross-sections in Exps. D183 and W183, respectively. The hardnesses of all indents are shown in Figure 5.14 as a function of the distance to the shear bands. Considering the scattering characteristics of nanoindentation results because of the small scale of indents and two-phase structure of Ti-6Al-4V (Qu et al., 2003), it is concluded that the shear band does not change the nanoindentation hardness in the drilled chip of Ti-6Al-4V. This result is different form that observed of CP Ti chip at low cutting speed turning (Sheikh-Ahmad et al., 2004). At low cutting speed, the thermal effect is weak, so the strian hardening effect dominates. Besides, the CP Ti is a single phase material, no phase transformation occurs. In high speed drilling of Ti-6Al-4V, both thermal effect and phase transformation can occur and counteract the strain hardening effect.

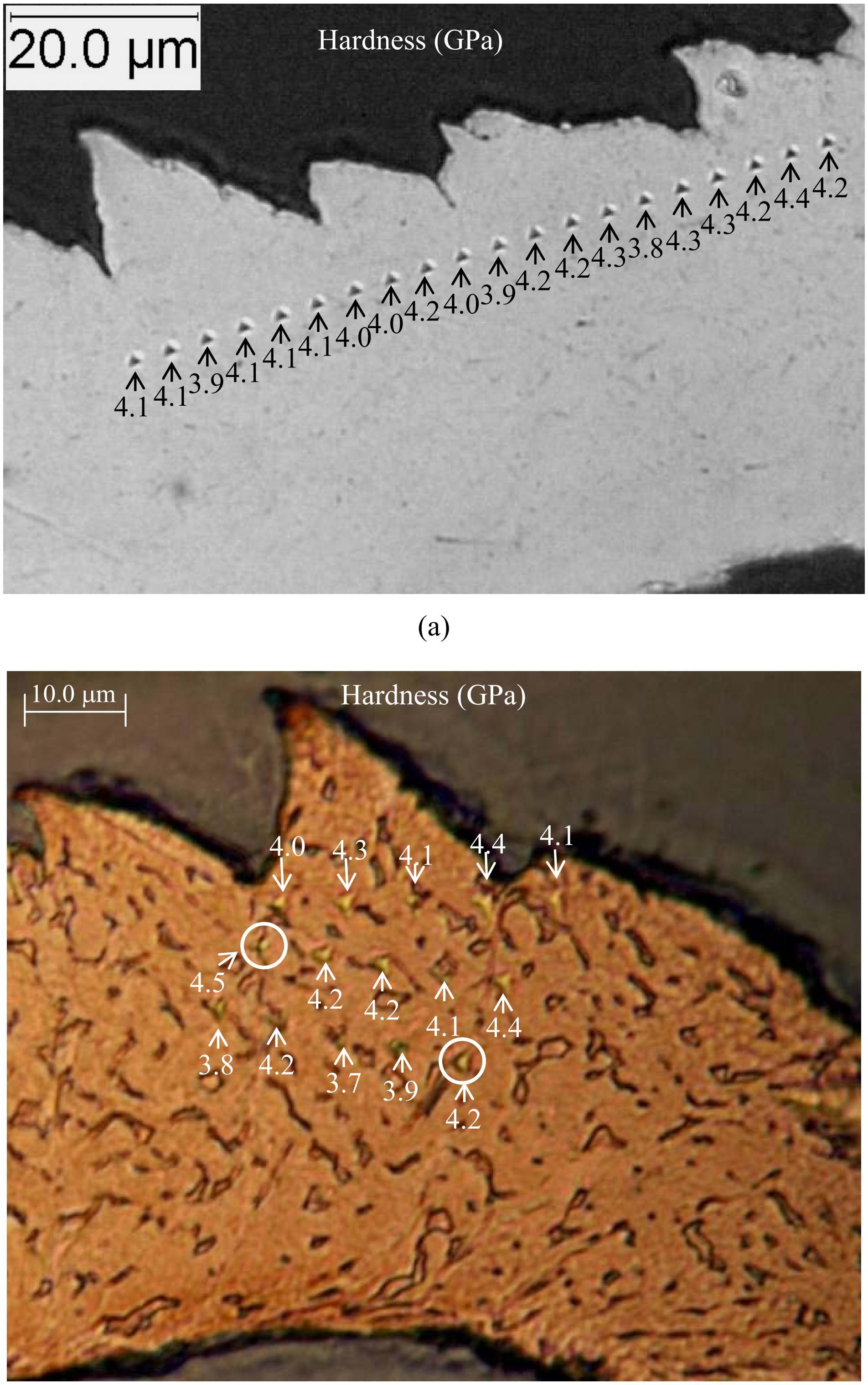
20.0 µm
Hardness (GPa)
4.1
4.1
3.9
4.1
4.1
4.1
4.0
4.0
4.2
4.0
3.9
4.2
4.2
4.3
3.8
4.3
4.3
4.2
4.4
4.2
10.0 µm
Hardness (GPa)
4.0
4.3
4.1
4.4
4.1
4.5
4.2
4.2
4.1
4.4
3.8
4.2
3.7
3.9
4.2

(a)

(b)

Figure 5.13. Nanoindentation on the chip cross-sections in Exp. D183: (a) before etch and (b) after etch (circled indents: indents close to the shear band).

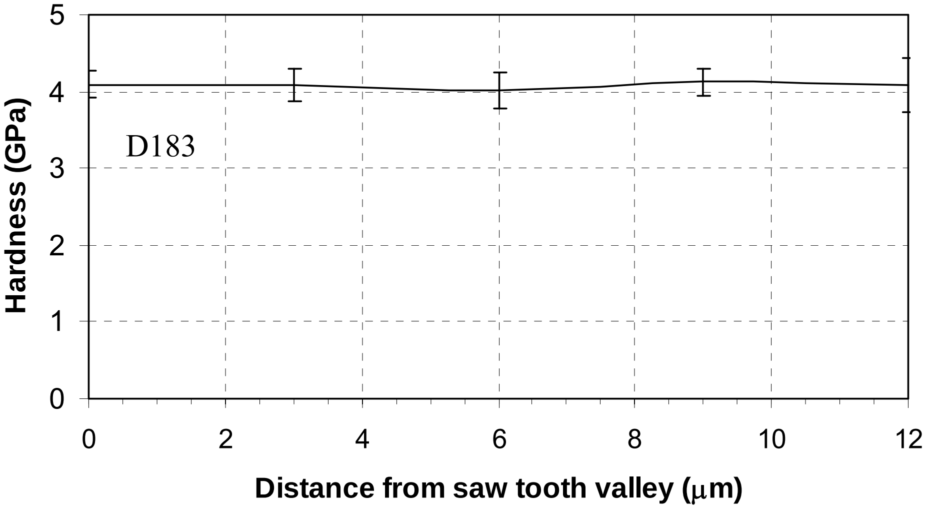

(a)

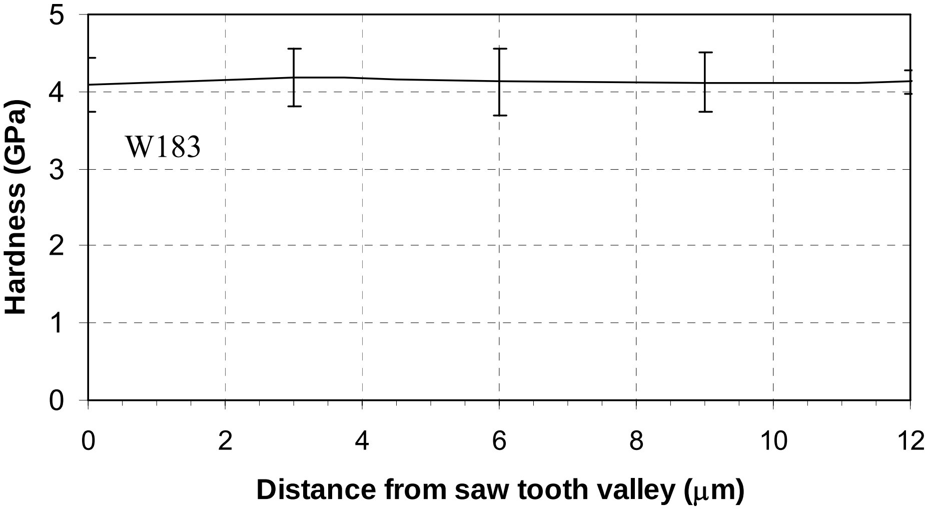

(b)

Figure 5.14. Chip nanoindentation hardness vs. the distance to the shear band: Exps. (a) D183 and (b) W183.

5.5. Concluding Remarks

Metallurgical studies, including SEM, XRD, electron microprobe, and nanoindentation tests were conducted on the hole surface and subsurface and the chips in high-throughput drillling of Ti-6Al-4V. High-throughput drilling decreased the size of crystallite and likely rms strains, changed the original texture and made the α crystallites in the material more randomly distributed. In dry drilling, the transformation of BCC β phase into martensitic HCP α phase was identified in a 10 to 15 μm wide subsurface layer adjecent to the hole surface by SEM and XRD analysis. This transformation was proved to be diffusionless, i.e., without chemical composition change.

High hardness was found in this layer by nanoindentation testing. No obvious β phase decomposition occurrd with the supply of cutting fluid. The high hardness layer was also narrower than that of dry drilling. Unlike chips formed in orthogonal cutting, drilling chips had complicated morphology. The saw-tooth feature only formed at the outmost region of the drill cutting edge, mainly due to the variable cutting speed along the cutting edge. Narrrow shear bands could be observed in the cross-sections of chips with distinct saw teeth, but no significant change of mechanical properties along the chips was found using nanoindentation tests.

CHAPTER 6

CONCLUSIONS

This research is a contribution to an on-going effort to increase the productivity and reduce the cost in the drilling of Ti alloys. The high-throughput drilling of Ti alloys was investigated through the experimental exploration, finite element modeling, and metallurgical analysis.

6.1. Major Contributions

The major contributions made in this research include:

1. The high throughput drilling of Ti alloy was demonstrated technically feasible up to a MRR comparable to that of cast iron, by using the proper drilling process parameters, spiral point drill geometry, fine-grained WC-Co tool material, and internal cutting fluid supply.
2. At the same MRR, the tool life and surface finish were optimized through the manipulation of different combination of cutting speed and feed.

3. The spatial and temporal distributions of temperature in a WC-Co spiral point drill in high-throughput drilling were analyzed in details. This analysis is also the first research attempt to investigate the drill temperature with cutting fluid supplied through drill body.
4. The heat partition on the tool-chip interface and convection coefficient of cutting fluid were determined using an inverse heat transfer method based on a thermal finite element model.
5. The stress distribution of a WC-Co spiral point drill was studied using a thermal-mechanical model which imported temperature history information from the thermal model.
6. The possible failure locations in different drilling conditions were analyzed using brittle failure criteria which considered the difference of WC-Co's tensile and compressive strengths and the temperature dependence of strengths. The relative applicability of Rankine, Mohr-Coulomb, and Modified Mohr criteria was compared.
7. The drilling force, torque, and the chip formation in high-throughput drilling with complicated spiral point drill geometry were simulated using a 3D updated-Lagrangian finite element model. This is also the first 3D updated Lagrangian model of the drilling using a spiral point drill.
8. The phase transformation of Ti-6Al-4V hole surface and subsurface was analyzed qualitatively and quantitatively. This phase transformation was proved to be diffusionless, i.e., without chemical composition change, which clarified the discussions over the cause of phase transformation. The influence of cutting fluid

on phase transformation was identified.

9. The influence of drilling process parameters on the change of Ti-6Al-4V hardness was studied. The effect of cutting fluid to reduce the change of material properties was demonstrated.
10. The commonly observed serrated chip formation in turning was found to be only formed at the outmost region of the drill cutting edge. These serrated chips were proved to be a result of shear band formation.

Through complete experimental analysis, high MRR of 156 mm^3/s with peripheral cutting speed up to 183 m/min was achieved using a commercially available 4 mm diameter WC-Co spiral point drill. The internal cutting fluid supply through the drill was important for long drill life and helped to improve the chip ejection, as demonstrated by the increased length of steady-state spiral cone chip region. The balance of cutting speed and feed was demonstrated to be critical. Under the same MRR (156 mm^3/s), the best drill life and surface finish results were achieved at 91 m/min peripheral cutting speed and 0.102 mm/rev feed using the WC-Co spiral point drill.

This study showed the peak drill temperature was over 1200°C at 183 m/min cutting speed and 0.051 mm/rev feed in dry drilling. The supply of cutting fluid reduced the peak drill temperature by half. Under all high-throughput drilling conditions, the highest temperature of the drill occurred in the cutting edge. The modified Mohr criterion predicted that the onset of drill failure would initiate in the cutting edge for dry drilling and in the chisel edge for wet drilling. It was also shown that the supply of cutting fluid helped to prevent premature tool failure associated with high drill temperature. The results further suggested that lower peripheral cutting speed and higher feed could further reduce the drill temperature while maintaining the same MRR, but the chisel edge would undergo increasingly higher stress. These different trends of temperature and stress made the optimum combination of cutting speed and feed existing in terms of tool life.

The 3D updated-Lagrangian finite element model of the high-throughput drilling of Ti-6Al-4V was validated by the comparison with experimentally measured thrust force and torque. This drilling model was able to show the distributions of stress and temperature in both the drill and workpiece/chip. The simulation results showed that peak chip temperature had the same trend as the peak tool temperature, but was slightly higher. Unlike the tool, the workpiece/chip stress was about 1250-1400 MPa, independent of the cutting condition. The peak stress was located at the end of the shear zone.

The metallurgical analysis showed that high-throughput drilling decreased the size of crystallite, changed the original texture and made the α crystallites in the material more randomly distributed. In dry drilling, the transformation of BCC β phase into martensitic HCP α phase was identified in a 10 to 15 μm wide subsurface layer adjecent to the hole surface. This transformation was proved to be diffusionless. High hardness was found in this layer by nanoindentation testing. No obvious β phase decomposition occurrd with the supply of cutting fluid. The high hardness layer was also narrower than that of dry drilling. Unlike chips formed in orthogonal cutting, drilling chips had complicated morphology. The saw-tooth feature only formed at the outmost region of the drill cutting edge, mainly due to the variable cutting speed along the cutting edge.

Narrrow shear bands could be observed in the cross-sections of chips with distinct saw teeth, but no significant change of mechanical properties along the chips was found.

6.2. Recommendations for Future Study

This study has identified several future directions for the further exploration of high-throughput, cost-effective drilling of Ti alloys:

Modeling of the drilling process based on the finite element method is an important future research direction to understand the work-material deformation and temperature distribution in high throughput drilling. In this research, the sequential thermo-mechanical analysis assumed the stress solution was dependent on a temperature field but there was no inverse dependency. To simulate the drilling process more accurately, a coupled thermo-mechanical modeling will be used to solve the stress and temperature simultaneously. Several key assumptions made in this study, including the negligible interactions between ECTs, the constant ratio of the tool-chip contact length to the chip thickness across the chisel and cutting edges and independent of the cutting fluid supply, and the same convection coefficient under all wet drilling conditions should be considered for future improvements. This study can be used to aid drill geometry design. For spiral point drills, the chisel edge drill geometry can be refined to reduce the peak compressive principal stress at the relative distance to the drill center (r/R), 0.2.

The 3D updated Lagrangian drilling modeling neglected the interaction between adjacent segments. To further improve the modeling accuracy, a model treating the whole drill cutting and chisel edges together is needed. Instead of using a single friction coefficient for the whole rake face, a more complex, stress, strain rate, and temperature-dependent friction model is required to simulate the drilling more closely.

The metallurgical analysis showed the narrow shear bands in the cross-sections of chips with distinct saw teeth, but did not observe significant change of mechanical properties along the chips. Further analysis to explain this phenomenon is needed.

Each of these suggested future topics can be used to further enhance the understanding of high-throughput drilling of Ti and contribute to increasing the productivity of drilling Ti at lower cost.

APPENDICES

Appendix A

Material Properties of CP Ti and Ti-6Al-4V

Table A.1. Material properties of CP Ti and Ti-6Al-4V.

Properties	CP Ti	Ti-6Al-4V
Thermal conductivity, k (W/m-K)	16.4	6.7
Heat capacity, c (J/kg-°C)	523	526
Density, ρ (kg/m^3)	4510	4430
Young's modulus, E (GPa)	105	114
Poisson's ratio, υ	0.37	0.33

Appendix B

Geometrical and Grinding Parameters of Spiral Point Drill

Table B.1. Drill geometrical parameters.

Diameter:	Helix angle	Clearance angle at cutting corner	Point angle	Chisel edge angle
9.92 mm	30°	7°	135°	52°
Chisel edge radius	Chisel angle length	Cutting edge hone radius	Width of margin	Coolant hole diameter
1.4 mm	1.8 mm	25-30 µm	0.43 mm	1.4 mm

Table B.2. Drill grinding parameters.

Grinding wheel diameter	Grinding wheel corner radius	Angle between the drill and grinding wheel axes
150 mm	1.1 mm	87.5°
Rotational velocity of the grinding wheel	Axial velocity of the grinding wheel	Radial velocity of the grinding wheel
1.16°/unit time	0.0436°/unit time	0.178 mm/unit time

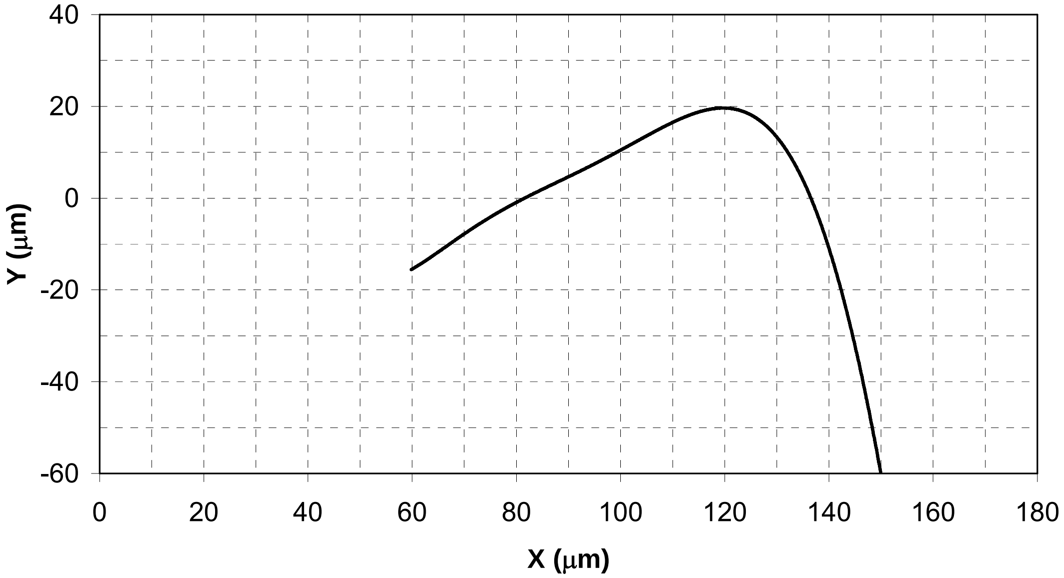

Figure B.1. Drill cutting edge profile (relative location r/R=0.8).

Appendix C

Oblique Cutting Analysis of Elementary Cutting Tool

In the view of drilling process, each ECT is under the effect of torque T and thrust force in the direction of drill axis F_{Th}.

For a simple oblique machining process, the resultant force on the tool can be resolved into several directional components in a number of ways.

By using the coordinate with one axis parallel to the cutting direction, as shown in Figure 3.6, three force components can be defined as: the force parallel to the cutting direction, F_c, the force normal to F_c and cutting edge, F_t, and the force normal to F_c and F_t, F_l. For each ECT, T is introduced by F_c, and F_{Th} results from F_t and F_l (Bono and Ni, 2001).

$$F_c = \frac{T}{r} \tag{C.1}$$

$$F_{Th} = -F_l \frac{\cos\theta}{\cos\lambda} + F_t \frac{\sqrt{\cos^2\lambda - \cos^2\theta}}{\cos\lambda} \tag{C.2}$$

Another way is using the coordinate system referred to the rake face of the tool.

The resultant force is composed of the force normal and parallel to the rake face F_n and F_f. F_f is in the chip flow direction, so it is friction force hindering the movement of the chips.

In order to make the resultant force lie in the plane defined by F_n and F_f, F_l is related to F_c and F_t by (Orfueil, 1987):

$$F_l = \frac{F_c(\sin\lambda - \cos\lambda \sin\alpha \tan\eta) - F_t \cos\alpha \tan\eta}{\sin\lambda \sin\alpha \tan\eta + \cos\lambda} \tag{C.3}$$

With equation A2 and A3, F_t and F_l can be solved in terms of F_c and F_{Th}:

$$F_t = \frac{F_{Th}(\sin\lambda \sin\alpha \tan\eta + \cos\lambda)\cos\lambda + F_c(\sin\lambda - \cos\lambda \sin\alpha \tan\eta)\cos\theta}{\sqrt{\cos^2\lambda - \cos^2\theta}(\sin\lambda \sin\alpha \tan\eta + \cos\lambda) + \cos\alpha \tan\eta \cos\theta} \tag{C.4}$$

$$F_l = F_c(\sin\lambda - \cos\lambda \sin\alpha \tan\eta)\sqrt{\cos^2\lambda - \cos^2\theta} - F_{Th}\cos\lambda \cos\alpha \tan\eta \tag{C.5}$$

With F_c, F_t, and F_l, F_f and F_n can be solved:

$$\begin{bmatrix} F_l \\ F_c \\ F_t \end{bmatrix} = \begin{bmatrix} \cos\lambda & \sin\lambda & 0 \\ \sin\lambda & \cos\lambda & 0 \\ 0 & 0 & 1 \end{bmatrix} \begin{bmatrix} -1 & 0 & 0 \\ 0 & \sin\alpha & \cos\alpha \\ 0 & \cos\alpha & -\sin\alpha \end{bmatrix} \begin{bmatrix} 0 & \sin\eta \\ 0 & \cos\eta \\ 1 & 0 \end{bmatrix} \begin{bmatrix} F_n \\ F_f \end{bmatrix} \tag{C.6}$$

$$F_n = \frac{F_c \cos\alpha \cos\eta - F_t(\cos\eta \cos\lambda \sin\alpha + \sin\eta \sin\lambda)}{\cos\eta \cos\lambda + \sin\alpha \sin\eta \sin\lambda} \tag{C.7}$$

$$F_f = \frac{F_t \cos\alpha \cos\lambda + F_c \sin\alpha}{\cos\eta \cos\lambda + \sin\alpha \sin\eta \sin\lambda} \tag{C.8}$$

Appendix D

Inverse Heat Transfer Solution of Drill Temperature in Drilling of Commercially Pure Ti

D.1. Experimental Setup

The Ti drilling experiment was conducted in a Mori Seiki TV 30 computer numerical control vertical machining center. Figure D.1 shows the experimental setup with the stationary drill and the Ti workpiece driven by a spindle. The drill was stationary so four thermocouples embedded on the flank face could be routed through coolant holes in the drill body to a data acquisition system during drilling (Agapiou and Stephenson, 1994). The drill and machine spindle axes were aligned by a test indicator installed in the spindle. The location of drill was adjusted in the horizontal plane until the eccentricity was less than 10 μm. The tilt of the drill was adjusted so that two planes which were 5 cm apart in height both had less than 10 μm eccentricity. Under the drill holder was a Kistler 9272 dynamometer to measure the thrust force and torque.

The workpiece was a 38 mm diameter grade two CP Ti bar. The drill was a 9.92

mm diameter spiral point drill, Kennametal K285A03906, with a S-shaped chisel edge.

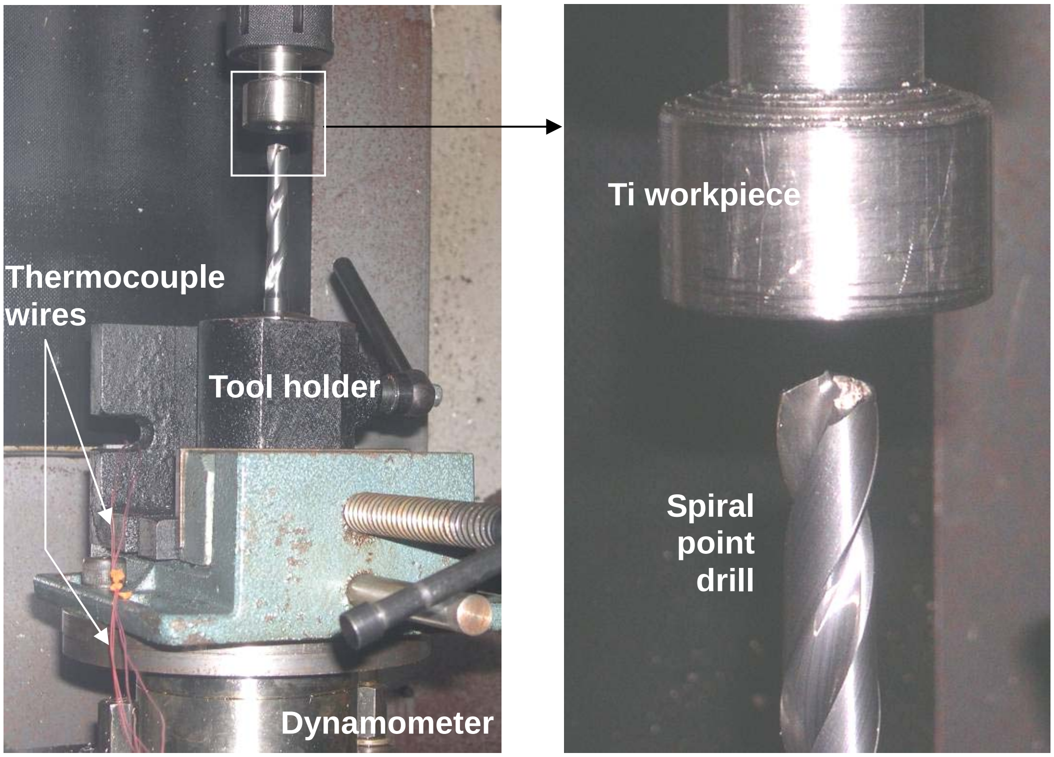

Figure D.1. Experimental setup with workpiece in the spindle and drill in a vertical tool holder.

Compared to a conventional twist drill, the chisel edge of the spiral point drill had lower negative rake angle. Therefore, the web could participate in cutting, not just indenting like the conventional twist drill. This reduces the thrust force and makes the drill self-centering (Ernst and Haggerty, 1958). The tool material was WC in a 9.5 wt% Co matrix (Kennametal grade K715). The spiral point drill has proven to perform well in high speed Ti drilling with peripheral speeds over 180 m/min (Li and Shih, 2007a). The chips were collected after drilling and chip thickness was measured to estimate the shear angle of each ECT. The average of three repeated measurements was used to represent the chip thickness.

Figure D.2 shows the spiral point drill and locations of four thermocouples on the drill frank surface. The top view of a new drill with two flutes and two coolant-through holes is shown in Figure D.2(a). An X_T-Y_T coordinate is defined at the center of the S-shaped chisel edge in the spiral point drill. The Y_T-axis is parallel to the tangent at the apex of the curved cutting edge. The tips of 0.127 mm diameter type E thermocouples (OMEGA 5TC-TT-E-36-72) were installed at the edge of hand-ground slots on the drill flank face. Four thermocouples, denoted as TC1, TC2, TC3, and TC4, are arranged at different locations on the flank surface, as shown in Figure D.2(b). The X_TY_T coordinates of the four thermocouples are listed in Figure D.2. The close-up view of TC1 and TC2 is illustrated in Figure D.2(c). TC1 is located close to the cutting edge and away from the drill center. TC2 is placed close to the flute and away from the drill center. TC3 and TC4, as shown in Figure D.2(d), both near the cutting edge, are close to and away from the drill center, respectively. Thermocouples are covered with cement (Omega OB-400) to secure the position and prevent the contact with the rotating workpiece.

In this dry drilling test, three drilling experiments were conducted at three rotational speeds, 780, 1570, and 2350 rpm, which corresponded to 24.4, 48.8, and 73.2 m/min drill peripheral cutting speeds, respectively. The feed remained fixed at 0.051 mm/rev or 0.025 mm for each tooth of the two-flute drill. All experiments were conducted dry without cutting fluid.

D.2. Experimental Results

The experimentally measured chip thickness, thrust force, and torque are applied to calculate the shear angle, ECT cutting forces, friction heat generation, and heat partition factor.

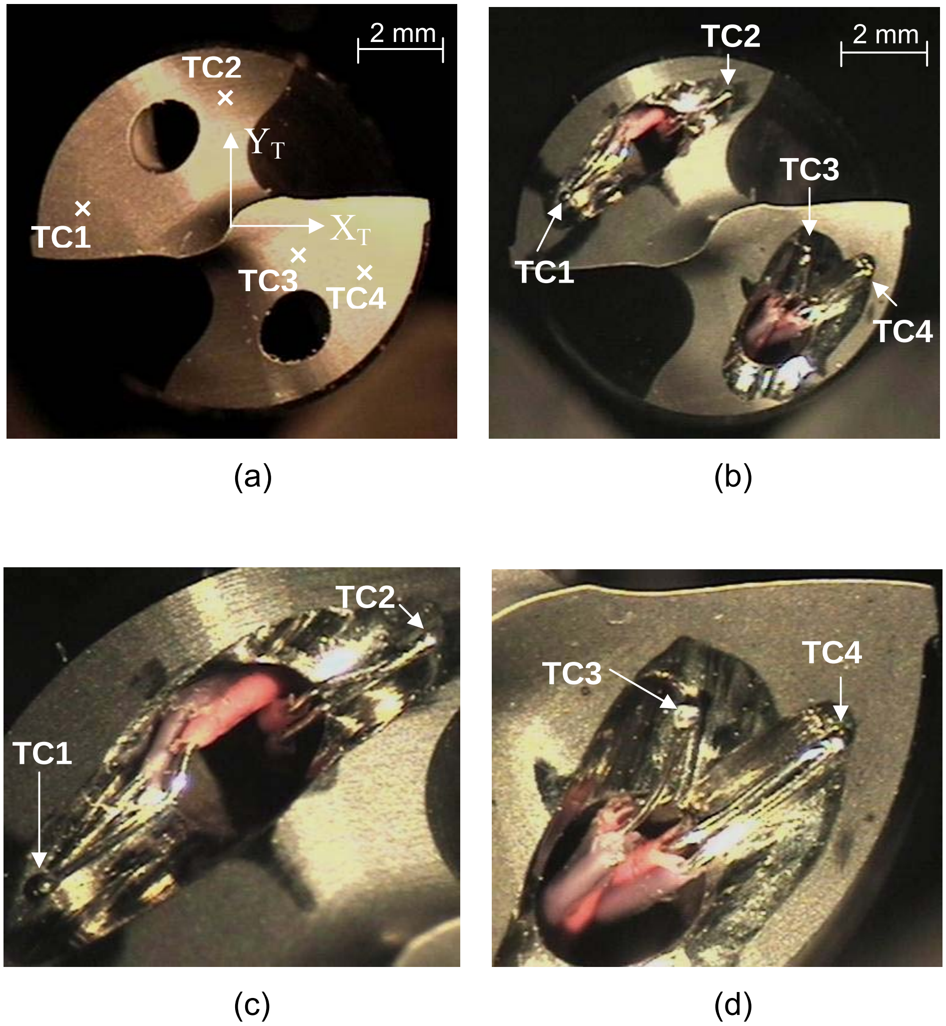
2 mm
TC2
Y_T
TC1
X_T
TC3
TC4
2 mm
TC2
TC3
TC1
TC4
TC2
TC1
TC3
TC4

Coordinates of Thermocouples (mm):

TC1 (–3.51, 1.14)	**TC2 (0.45, 3.60)**
TC3 (2.4, –0.51)	**TC4 (3.93, –0.69)**

(a) (b)

(c) (d)

Figure D.2. The spiral point drill and thermocouple locations in the drill flank face: (a) original drill, (b) drills with thermocouples embedded, (c) close-up view of TC1 and TC2, and (c) close-up view of TC3 and TC4.

D.2.1. Chip morphology, thickness, and shear angle

The morphology of the Ti chips generated at all three drilling speeds has the same shape which is an initial spiral cone followed by a folded long ribbon. An example of the chip machined at 73.2 m/min peripheral cutting speed (2350 rpm rotational speed) is shown in Figure D.3(a). The spiral cone, as shown in the close-up view in Figure D.3(b), is formed by the gradual engagement of chisel and cutting edges at the drill tip. After the drill tip fully engages the workpiece, the chip morphology changes to the ribbon type. Folding of the ribbon chip is due to the resistance caused by chip ejection (Ke et al., 2005).

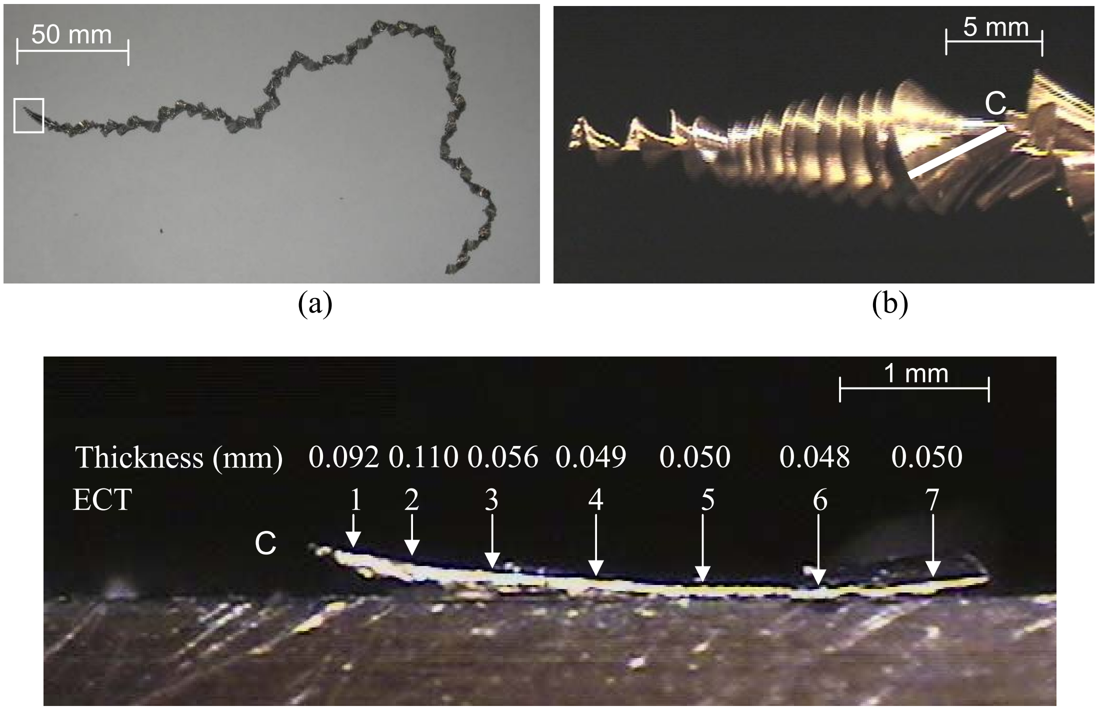

(a) (b)

(c)

Figure D.3. Ti chip at 2350 rpm spindle speed (73.2 m/min peripheral cutting speed): (a) the spiral cone followed by the folded long ribbon chip morphology, (b) close-up view of the spiral cone chip at the start of drilling, and (c) chip cross-section and chip thickness variation of ECT. (C: chip close to the center of drill).

At the end of the spiral cone, a cross-section of the chip, as marked by the line in

Figure D.3(b), determines the variation of chip thickness across the chisel and cutting edges at the moment when the drill tip makes the full-engagement with workpiece. The symbol C in Figure D.3(b) represents the center of the drill. A picture of the chip cross-section and the corresponding ECT and thickness along the line in Figure D.3(b) are shown in Figure D.3(c). The chip generated by the chisel edge is thicker, due to the negative rake angle. This is consistent with the anticipated rake angle effect on chip thickness.

Measured chip thicknesses a_c and calculated shear angles ϕ at seven ECTs under three peripheral cutting speeds are summarized in Figure D.4. Consistently, the chisel edge generates higher chip thickness and lower shear angle, compared to those of the cutting edge. Along the cutting edge, the chip thickness increases and the shear angle decreases. Under the same cutting speed, the rake angle (α) and the angle between drill axis and cutting edge (θ) of each ECT affect the chip thickness and shear angle. Large α usually decreases the chip thickness and increases the shear angle, while large θ increases the uncut chip thickness as well as the chip thickness. Along the cutting edge, α increases and θ is about the same (Figure 3.4). The combination of these two effects results in a lower chip thickness in the cutting edge, as shown in Figure D.4.

D.2.2. Thrust force and torque on ECT

Figure D.5 shows the thrust force and torque measured at three drilling speeds. In the first 1.9 mm of drilling, the force and torque gradually increase until the drill tip makes full-engagement with workpiece. Increments in force and torque are assumed to be contributed by the sequential participation of ECTs in cutting. The vertical dash line and the number above it in Figure D.5 represent the drilling depth and the corresponding ECT fully engaged the workpiece, respectively. After the drill tip fully engages the workpiece, the thrust force and torque both reach a more stable level. The speed has a significant effect on the torque and changes the thrust force only slightly after the full engagement of drill tip. High torque at high cutting speed is mainly due to the increasing difficulty in chip ejection (Ke et al., 2005).

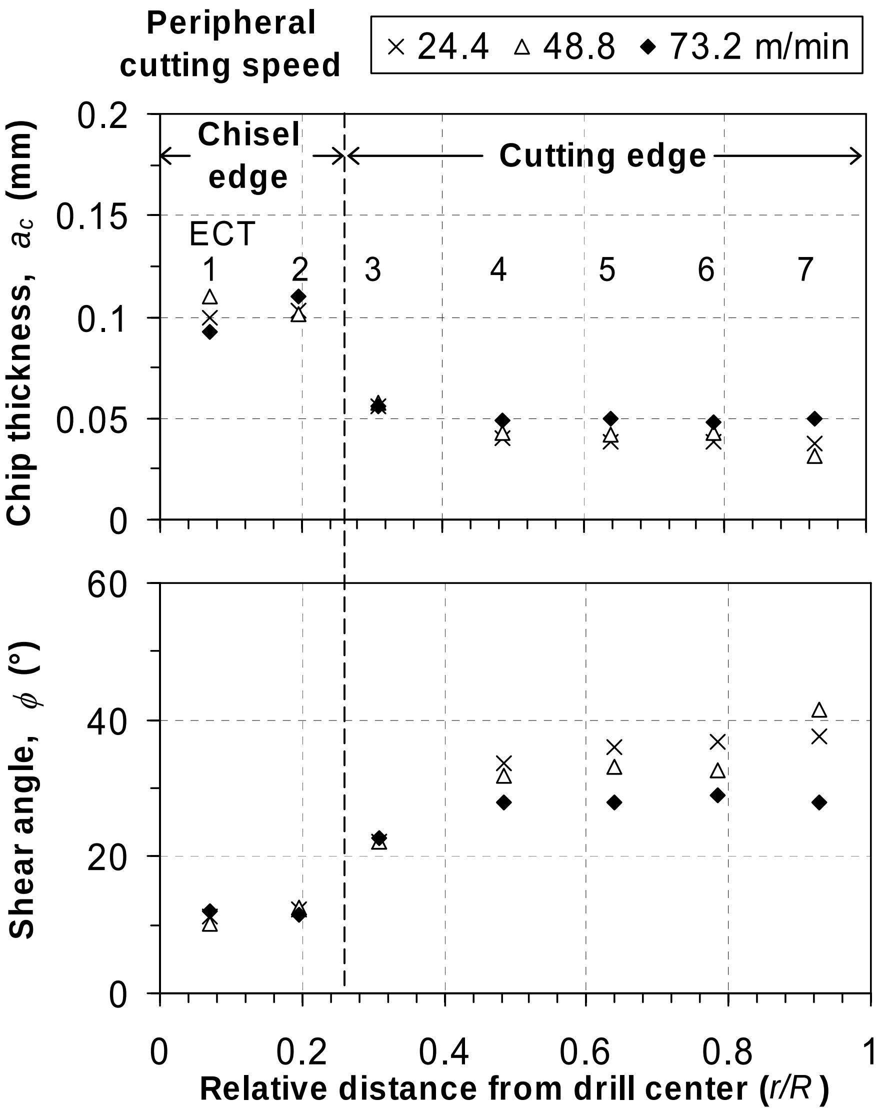

Figure D.4. Chip thickness and shear angle of seven ECTs.

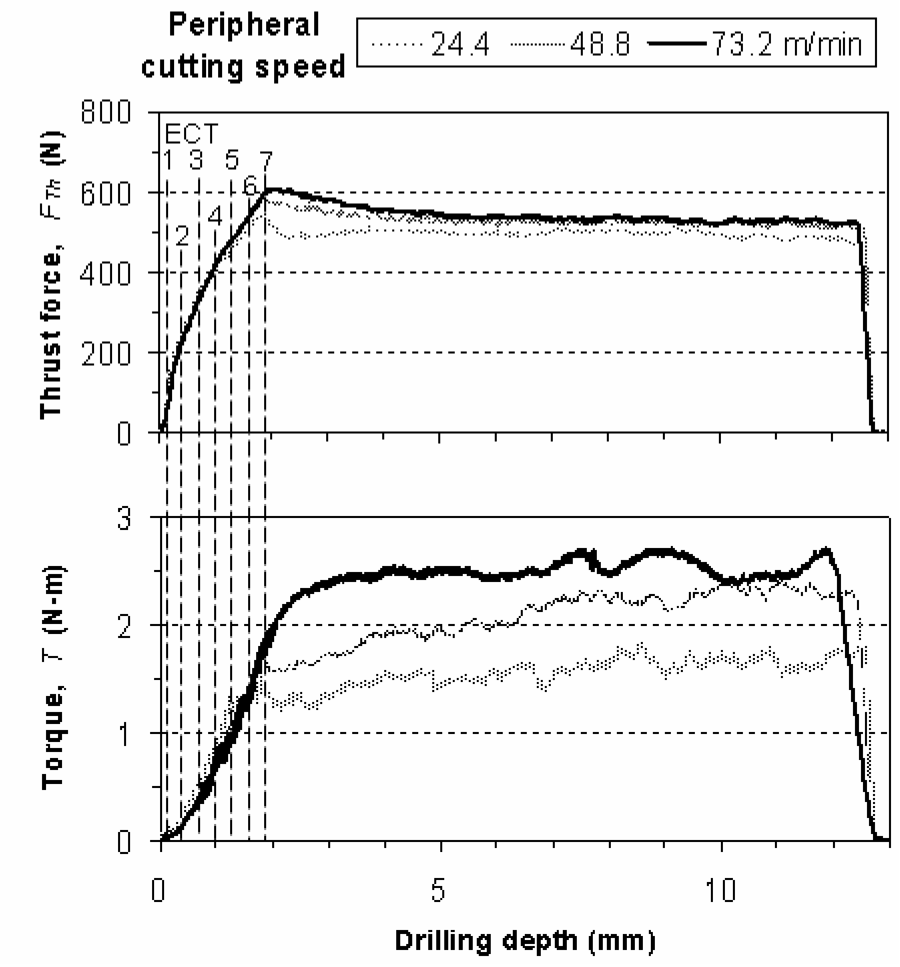

Figure D.5. Thrust force and torque vs. drilling depth.

The F_{Th} and T of each ECT, as shown in Figure D.6, are calculated from the incremental increase of thrust force and torque as each ECT engages in drilling (Figure D.5). Although ECTs 1, 2, and 3 generate high thrust force, their value relative to other ECTs is small in comparison with a conventional twist drill (Strenkowski et al., 2004). Similar to a conventional twist drill, the ECTs at the cutting edge of the spiral point drill has a major contribution to the torque.

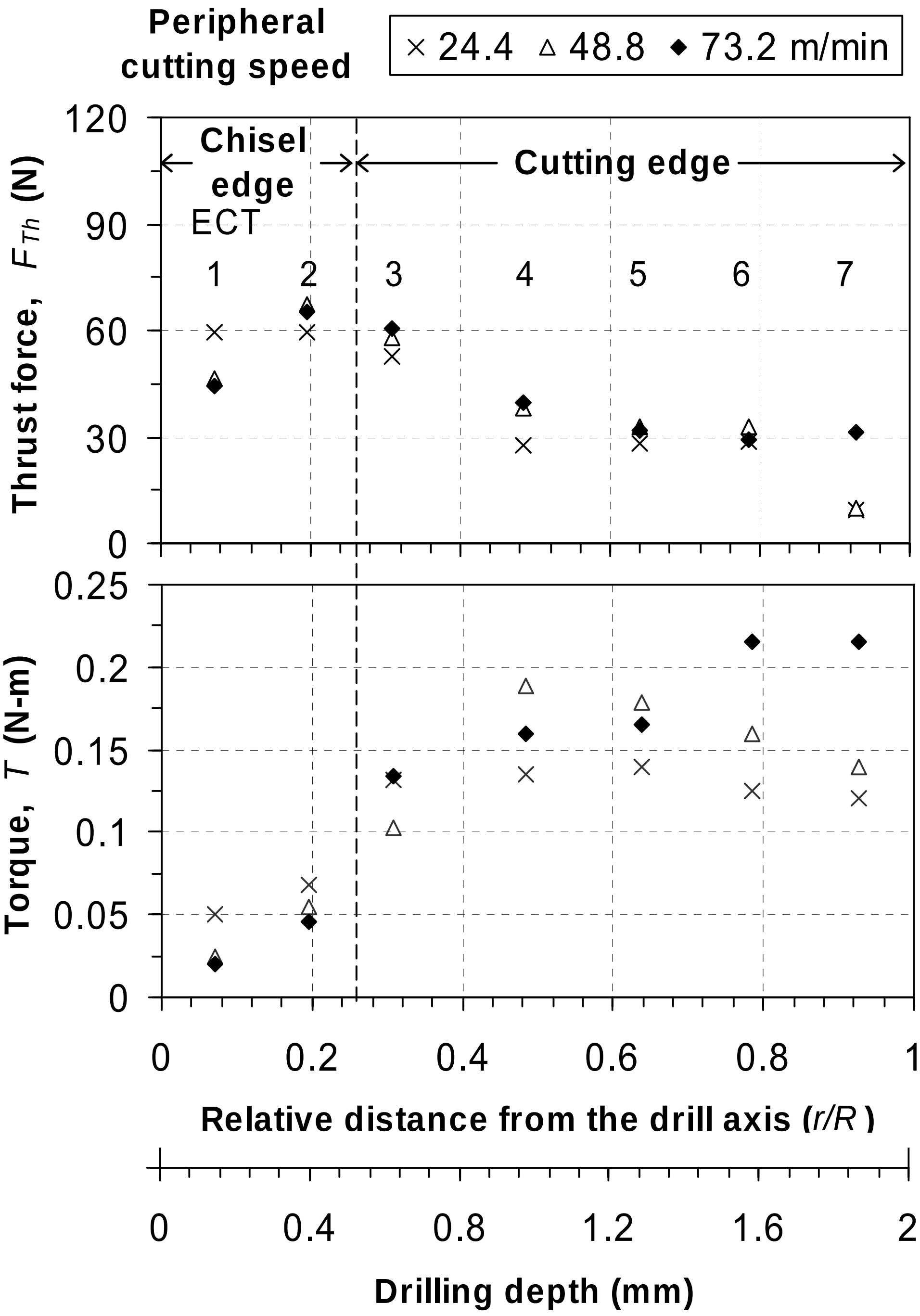

Figure D.6. Thrust force and torque of seven ECTs.

D.2.3. Solution of the s, K and heat generation rate

The measured temperatures at TC1 and TC3 at three peripheral cutting speeds are shown in Figure D.7. By minimizing *Obj*(*s*) using the measured temperature at TC1 and TC3 as input, the value of *s* is solved as 6, 6, and 4 for 24.4, 48.8, and 73.2 m/min peripheral cutting speed, respectively. The Golden Section optimization method (Himmelblau, 1972) was used for solution.

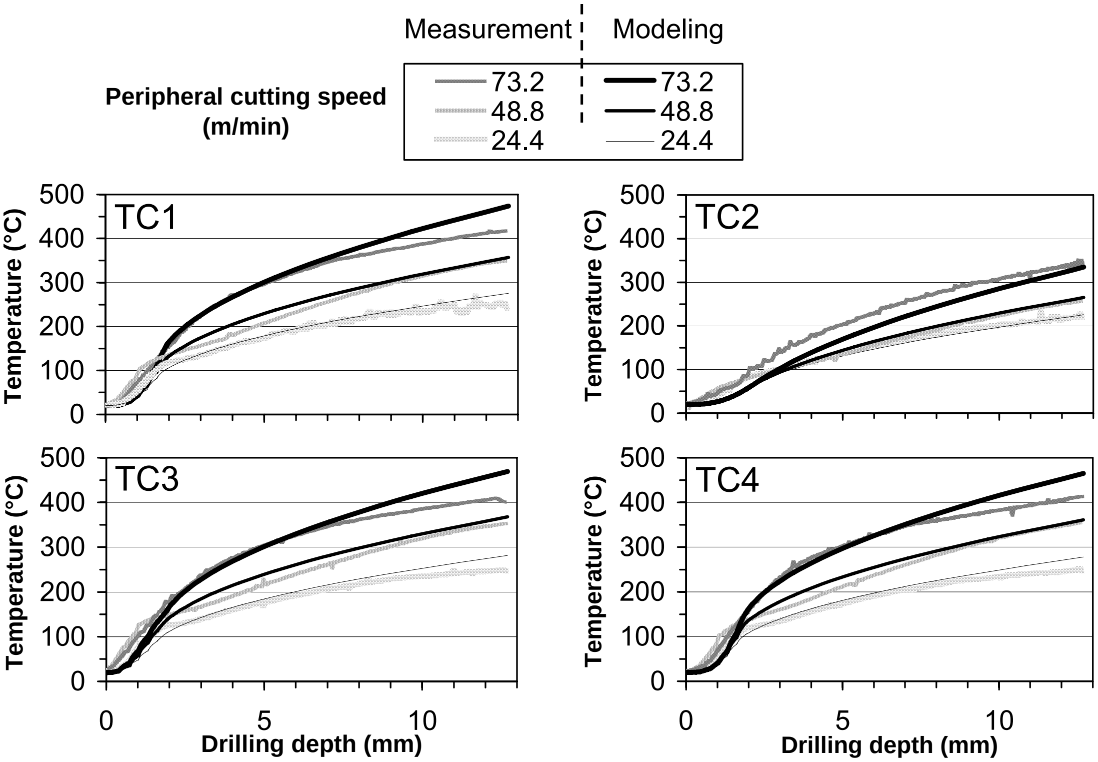

Figure D.7. Comparison of the measured and modeled temperature at four thermocouple locations.

Using the temperature-dependent material properties, the heat partition factor *K* varies both spatially and temporally. The *K* after 1.9 mm depth of drilling, i.e., the stage when the whole cutting edge engages the workpiece, is shown in Figure D.8. The lower *K* at higher cutting speed represents that a larger portion of heat generated at the tool-chip interface is carried away by the chip at higher cutting speed. This is a well-known phenomenon at high cutting speed (Shaw, 1984). Due to the cutting speed effect, ECTs at the cutting edge have a higher *K* than those on the chisel edge.

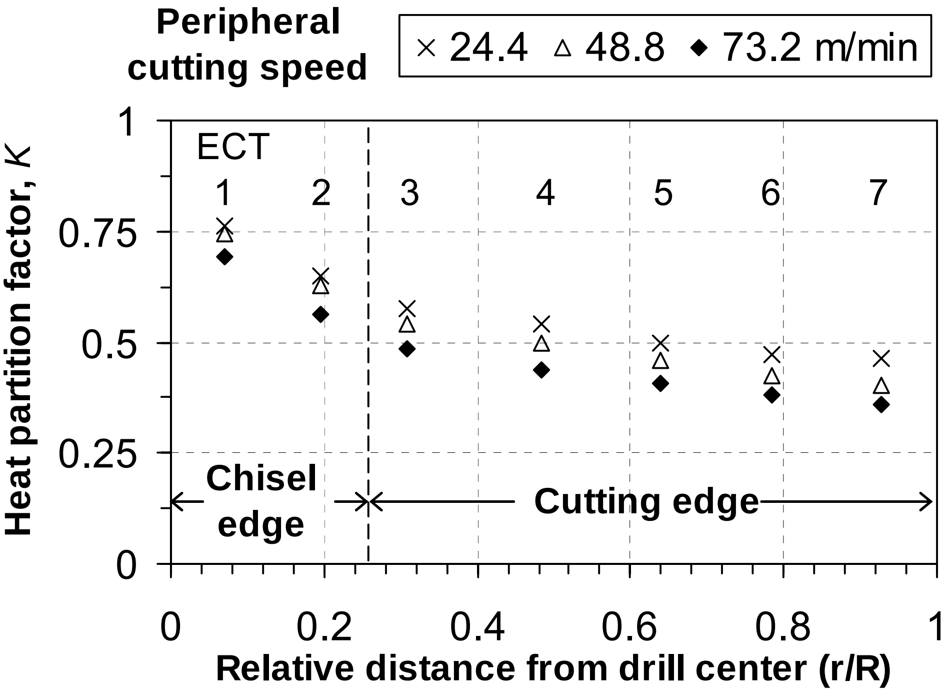

Figure D.8. The heat partition factor K at seven ECTs after 1.9 mm depth of drilling.

To compare the heat transfer to each ECT, the q_{tool} is divided by the length of ECT cutting edge to calculate the heat generate rate per unit length of contact, denoted as q'_{tool}. Results of q'_{tool} after 1.9 mm depth of drilling are shown in Figure D.9. Consistently, due to the higher torque, ECTs at the cutting edge have a much higher q'_{tool} than those at the chisel edge. At 73.2 m/min peripheral cutting speed, the q'_{tool} increases along the cutting edge towards outside of the drill. This trend is altered at 24.4 and 48.8 m/min cutting speeds at which q'_{tool} at ECT 7 is lower than that at ECTs 5 and 6. This is because the torque of ECT 7 is higher than that of ECTs 5 and 6 at 73.2 m/min cutting speed but lower at 24.4 and 48.8 m/min cutting speed (Figure D.6). At lower peripheral cutting speed, i.e., lower rotational speed, the effect of strain rate hardening at ECT 7 is not high enough to compensate the effect of high rake angle (Figure 3.4), which generates lower cutting forces F_c.

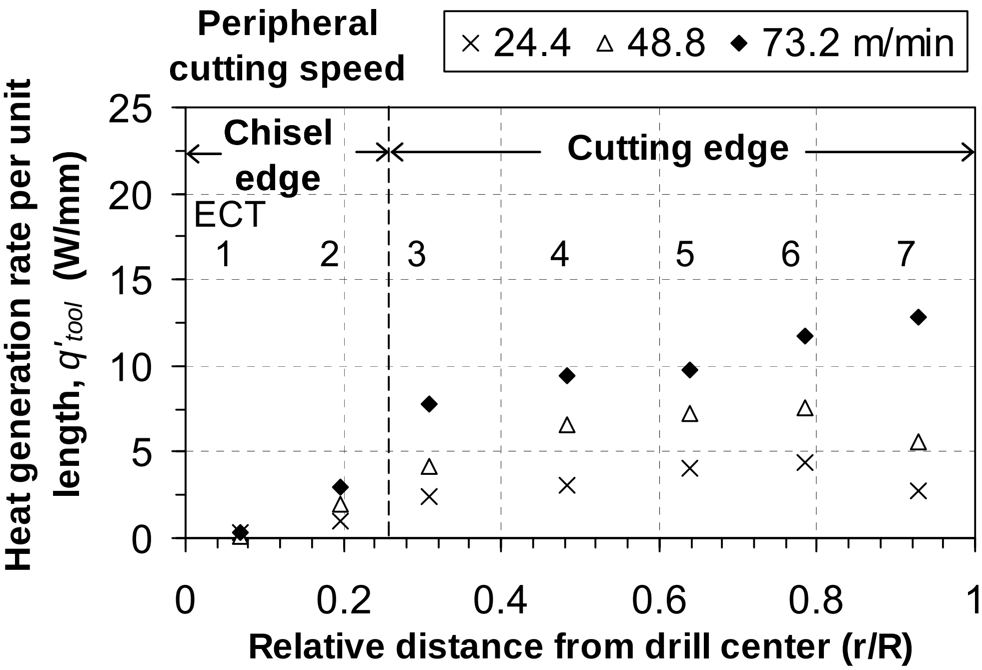

Figure D.9. The heat generation rate per unit length q'_{tool} at seven ECTs after 1.9 mm depth of drilling.

The peripheral cutting speed has a significant effect on the heat generation rate at the cutting edge. As the cutting speed increases from 24.4 to 73.2 m/min, q'_{tool} increases by more than 100% for most of the ECTs on cutting edge.

D.3. Validation of Finite Element Modeling of Drill Temperature

The finite element prediction of drill temperature is validated by the comparison with experimentally measured temperatures at thermocouples TC2 and TC4. As shown in Figure D.7, a good match of temperature can be seen at TC2 and TC4. The temperature at TC2 is lower and the discrepancy is higher than the other three thermocouples because TC2 is the furthest away from the cutting edge. Generally, the simulation underestimates the temperature at the beginning of drilling. This is likely due to the effect of grooves carved on the drill flank face used to install thermocouples. These grooves were not considered in the finite element modeling.

To quantify the discrepancy between the experimental and modeling results, the root mean square (RMS) error, e_{RMS} (Himmelblau, 1972), and the percentage error, p, are defined.

$$e_{RMS} = \sqrt{\frac{1}{N}\sum_{i=1}^{N}(T_{j|\mathrm{exp}}^{t_i} - T_{j|\mathrm{est}}^{t_i})^2} \qquad \text{(D.1)}$$

$$p = \frac{e_{RMS}}{T_{j|peak}} \qquad \text{(D.2)}$$

where N is the number of temperature measurements, j is the thermocouple, and $T_{j|peak}$ is the peak measured temperature. The absolute temperature scale is used to calculate p.

The e_{RMS} and p at four thermocouples are listed in Table D.1. The e_{RMS} increases at high cutting speeds due to the high tool temperature at high cutting speed. In general, the e_{RMS} and p at TC2 and TC4 are comparable with those of TC1 and TC3. At all three cutting speeds, the percentage error p is less than 5%, which is a considerable improvement from the previous drill temperature study (Bono and Ni, 2001). In summary, the low e_{RMS} and p and good match of experimentally measured and finite element modeled temperatures at four thermocouples throughout the drilling process validates the proposed method to predict drill temperature.

Table D.1. Root mean square (RMS) and percentage errors.

Peripheral cutting speed (m/min)		TC1	TC2	TC3	TC4
24.4	e_{RMS} (°C)	10.8	9.5	15.3	12.9
	p (%)	2.1	1.9	2.9	2.5
48.8	e_{RMS} (°C)	18.2	11.8	22.1	17.7
	p (%)	2.9	2.2	3.5	2.8
73.2	e_{RMS} (°C)	24.9	29.6	27.2	23.6
	p (%)	3.6	4.8	3.9	3.4

D.4. Drill Temperature Distributions

The spatial distribution of temperature near the tip of the spiral point drill after 12.7 mm depth of drilling is shown in Figure D.10. The drilling time was 19.2, 9.6, and 6.4 s at 24.4, 48.8, and 73.2 m/min peripheral cutting speeds, respectively. High temperature is concentrated along the cutting edge at the drill tip. High peripheral cutting speed generates high temperatures in the drill. The peak temperature increases from 480 to 1060°C when the drill peripheral cutting speed is increased from 24.4 to 73.2 m/min. The peak temperature is located on the cutting edge near the drill margin for all three cutting speeds. This study shows the high drill temperature and cutting speed effect in drilling Ti.

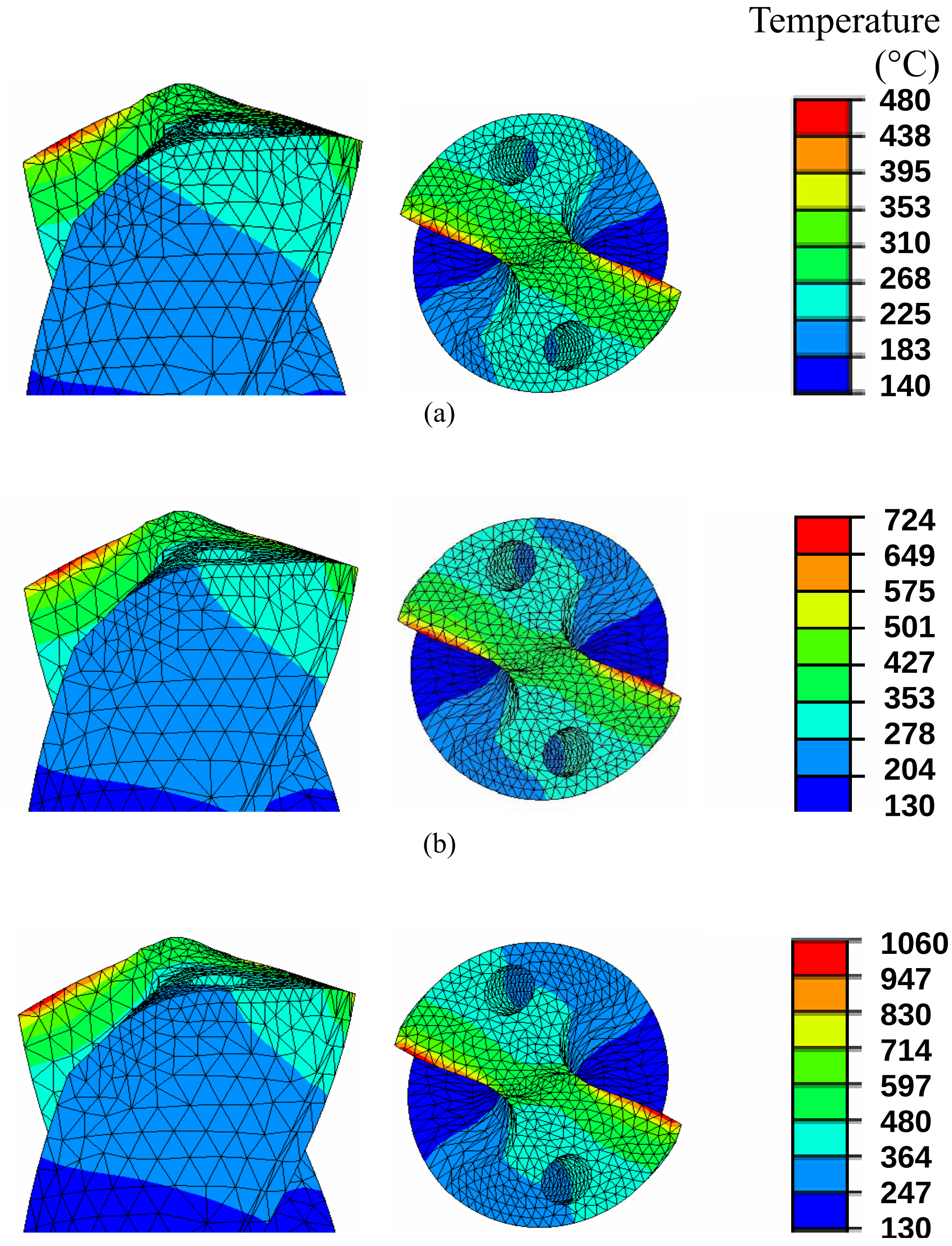

(a)

(b)

(c)

Figure D.10. Temperature distribution at the drill tip after 12.7 mm depth of drilling at peripheral cutting speeds: (a) 24.4, (b) 48.8, and (c) 73.2 m/min.

Figure D.11 shows cutting speed effect on distributions of temperature along the chisel and cutting edges after 12.7 mm depth of drilling. At three peripheral cutting speeds, the pattern of temperature distribution is the same: low at the chisel edge and high near the outside of the cutting edge. As the cutting speed increases, the location of peak temperature moves outside toward the drill margin.

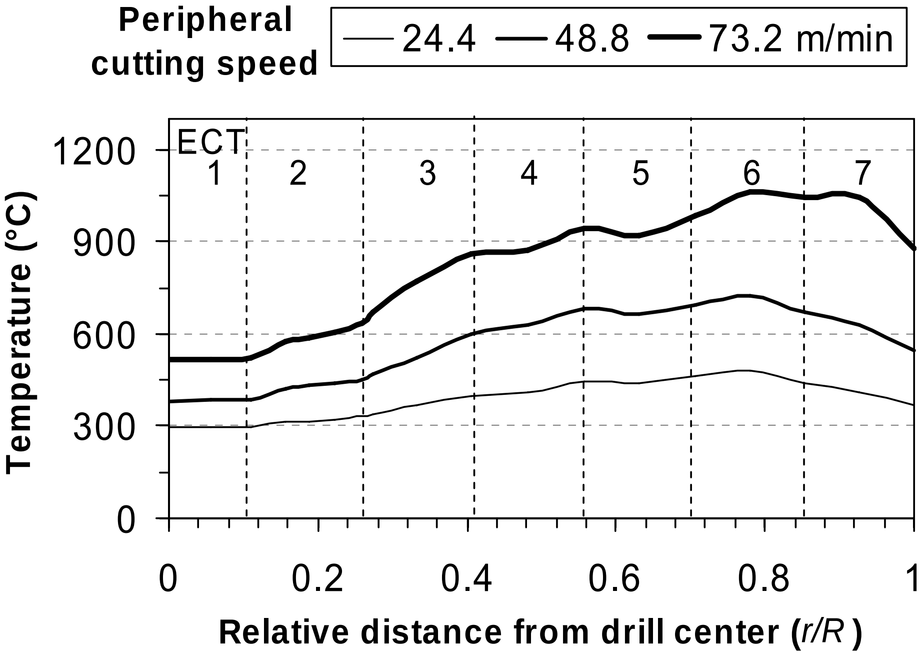

Figure D.11. Temperature along the drill chisel and cutting edges at 12.7 mm depth of drilling.

At the highest peripheral cutting speed, 73.2 m/min, after drilling for 0.2, 0.5, 0.8, 1.0, 6.4, 20, and 50s, the temperature distributions along the chisel and cutting edges of the drill are shown in Figure D.12. The location of peak temperature on the drill cutting edges is moving with respect to the time of drilling. In this case using the spiral point drill for Ti, the location of peak temperature gradually moves from the drill center toward the drill margin. But, even at long drilling time, the peak temperature does not occur at the outmost point of the cutting edge (drill margin). The temporal analysis of drill temperature shows the steady-state was not achieved. The drill temperature keeps rising with the increase of the drilling depth. The peak temperature reaches 1750°C at 50 s drilling time, which corresponds to a 102 mm depth of drilling. The rate of increase in drill temperature gradually drops at higher drilling depth.

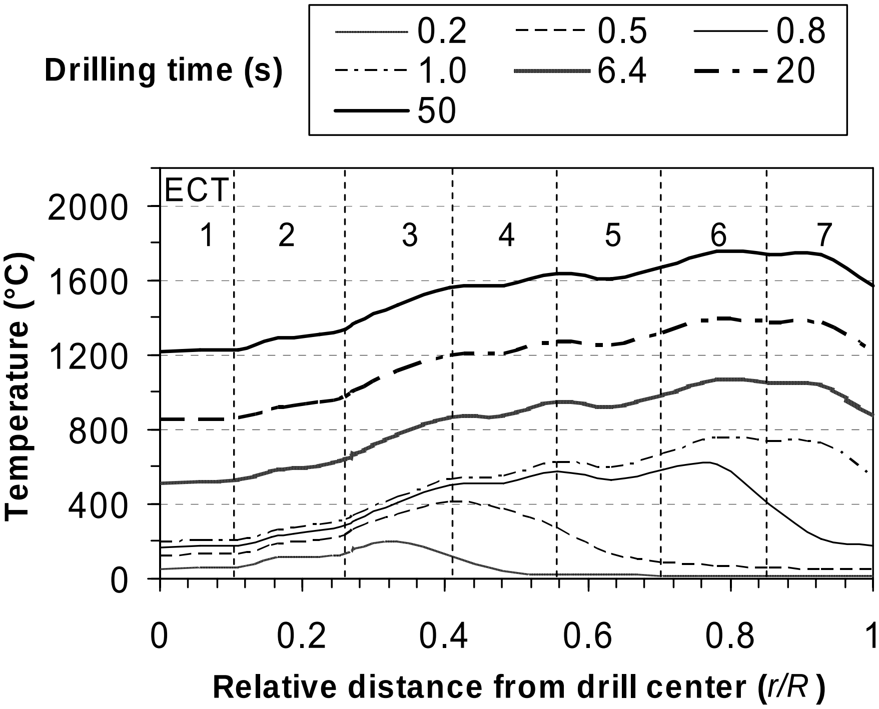

Figure D.12. Temperature along the drill chisel and cutting edges at 73.2 m/min cutting speed.

D.5. Concluding Remarks

For dry drilling of CP with moderate MRR, this study quantified the level of high temperature and effects of cutting speed and cutting time on drill temperature distributions in dry drilling of Ti. An accuracy of less than 5% discrepancy between experimentally measured and numerically predicted drill temperature was achieved. This study showed that the cutting edge had a lower heat partition factor and higher heat generation rate per length than the chisel edge. The peak temperature of the drill increased from 480 to 1060°C as the peripheral cutting speed increased from 24.4 to 73.2 m/min after 12.7 mm depth of drilling. The location of peak temperature moved outside toward the drill margin as the peripheral cutting speed increased. The modeling results also showed the drill temperature did not reach the steady state after a long, 50s, drilling time.

Appendix E

Drill Temperature Measurement Using Embedded Foil Tool-Work Thermocouple Method

The temperature of a HSS twist drill when drilling Ti-6Al-4V plates was measured using the embedded foil thermocouple method developed by Bono and Ni (2002). The temperature pattern was compared with the results of the inverse heat transfer model as presented in Chapter 3.

E.1. Experimental Setup

The drilling experiment was conducted in a Fadal computer numerical control vertical machining center. Figure E.1 shows the experimental setup with a 9.92 mm HSS conventional twist drill and a workpiece consisting of two 6.35 mm thick Ti-6Al-4V plates. The drill was mounted through a slip ring device which could transmit the electrical signal from the rotating drill to a stationary data acquisition setup. An insulation-foil-insulation layer comprised of a 50 μm thick Nickel-Iron foil placed between two 100 μm thick mica thermal insulation materials was embedded between the two Ti-6Al-4V plates. The thermocouple electromotive force (emf) generated when the drill cutting edge cuts through the foil was recorded and calibrated to detect the drill temperature.

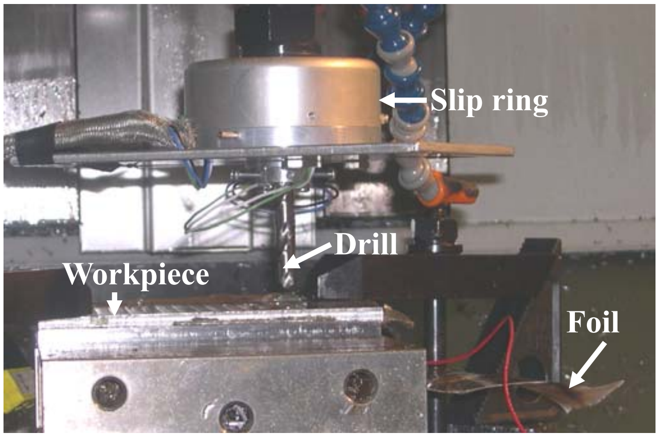

Figure E.1. Experimental setup of embedded foil tool-work thermocouple method.

E.2. Experimental Result

The test was conducted at 10 m/min peripheral cutting speed and 0.05 mm/rev feed without the supply of cutting fluid. The temperature along the cutting edge when it reached 6.35 mm depth was shown in Figure E.2. It has the similar pattern as the temperature calculated for drilling at higher cutting speed: the peak temperature is located at cutting edge close to the drill margin. It proved the effectiveness of the inverse heat transfer model. Even at this low speed, the peak temperature was still as high as 460°C. It demonstrated the high temperature in drilling Ti alloys. Because of the straight chisel edge of this conventional twist drill, the whole chisel edge passed the foil at the same time. As a result, the temperature distribution within the chisel edge could not be revealed.

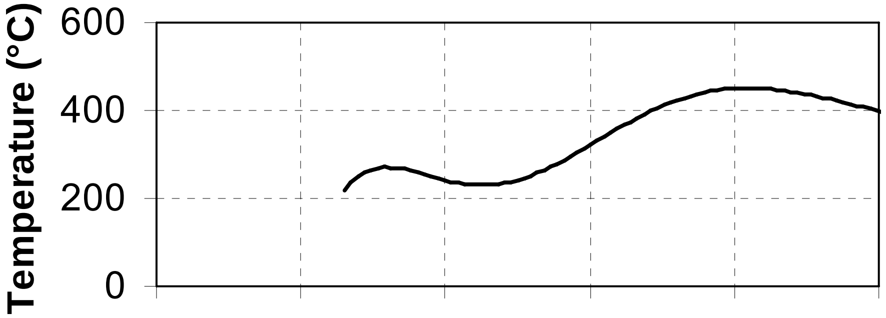

Relative distance from drill center (r/R)

Figure E.2. Drill cutting edge temperature distribution at 10 m/min peripheral cutting speed and 0.05 mm/rev feed using a HSS conventional twist drill.

Appendix F

3D Finite Element Modeling of Low Speed Drilling of Ti-6Al-4V Using Conventional Drills

In the drilling simulations, due to the complexity of drill geometry, the drill cutting and chisel edges are usually represented as a series of oblique or orthogonal cutting sections to simplify the problem. This method has limited capabilities and accuracy, because the interaction between adjacent segments is neglected in this model.

In this chapter, a 3D updated-Lagrangian finite element modeling treating the whole drill cutting and chisel edges together is applied to drilling of Ti-6Al-4V. To simplify the problem, a conventional twist drill geometry is used at low cutting speed. Simulations were performed with Third Wave Systems AdvantEdgeTM FEM software, customized for machining applications.

F.1. Drill MODEL

A two-flute conventional twist drill geometry can be prescribed with a tool diameter D0, clearance diameter (margin width) Dc, helix angle Ha, web thickness w, flute radius Fr and length Fl, cutting edge radius, clearance angle, point angle Pa, and chisel edge angle Ca, as show in Figure F.1.

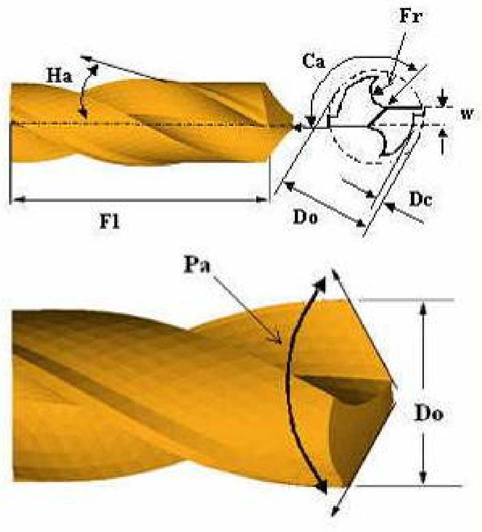

Figure F.1. Parameterization of a standard two flute twist drill.

While momentum effects are included in the FEM formulation, the overall structural dynamics are not taken into consideration in this analysis. The drill itself is modeled as elastic but is idealized as residing in a rigid holder.

F.2. Finite Element Initial Mesh

As shown in Figure 2.2, the drill needs to move downward a distance equal to the drill point length before the drill cutting edge fully engages with the workpiece. It would take a long time to simulate this engagement process, because of the high computational cost of thermal-mechanical coupled analysis.

To overcome this difficulty, a workpiece mesh with a predrilled cone-shape blind hole to accommodate the whole drill point region is generated. Thus, the thrust force and torque would reach a relatively steady state value very quickly since the whole cutting edge engages with the workpiece from the beginning.

Figure F.2 shows the 3D finite element mesh using a conventional twist drill. The 4-node tetrahedral finite element was used to model the workpiece and tool. The models of tool and workpiece include 4,600 and 5,500 initial nodes, respectively. After the start of drilling, due to the remeshing, the number of nodes is expected to increase.

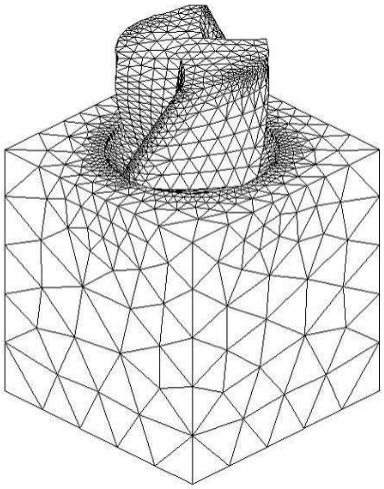

Figure F.2. Finite element mesh for 3D drilling model.

F.3. MODEL VALIDATION

The model is validated by comparison with experimentally measured thrust force and torque. The drilling test was conducted on a Mori-Seiki computer numerical control machining center using a M2 high speed steel twist drill with 3.97 mm diameter, 0.77 mm web thickness, 118° point angle, and 30° helix angle. Workpiece is a 6.35 mm thick Ti-6Al-4V plate. Drilling tests were conducted at three drill rotational speeds, 734, 1100, and 1468 rpm, which corresponds to 9.1, 13.7, and 18.3 m/min drill peripheral cutting speed, respectively. A constant feed of 0.051 mm/rev was used.

Figure F.3 shows the curves of thrust forces and toques of finite element modeling. The averages of experimentally measured thrust forces and torques between Stages A and B are labeled in the figure. As shown in Figure F.3, the FEM model provides a reasonable estimation of thrust force. The thrust force is less than 20% underestimation, but the torque can be overestimated by 50%. In experiments, a large amount of heat is generated from the initial contact of the drill and workpiece to the stage when the drill cutting edge fully engages the workpiece. It results in high temperature and softens the workpiece. In comparison, the drill temperature is at room temperature when the cutting edge fully engages the workpiece in FEM. As a result, the workpiece is harder and results in higher torque. Another possible reason for the discrepancy is the inaccuracy of material and friction modeling. A constant coefficient of friction was used. The lack of accurate friction modeling is, as usual, a limitation in FEM modeling of machining processes (van Luttervelt, 1998).

F.4. Chip Formation and Temperature and Stress Distributions

The chip formation has a significant influence on the thrust force and torque as well as the temperature and tool performance. As a convenient tool, finite element modeling provides an excellent insight to the material deformation during drilling.

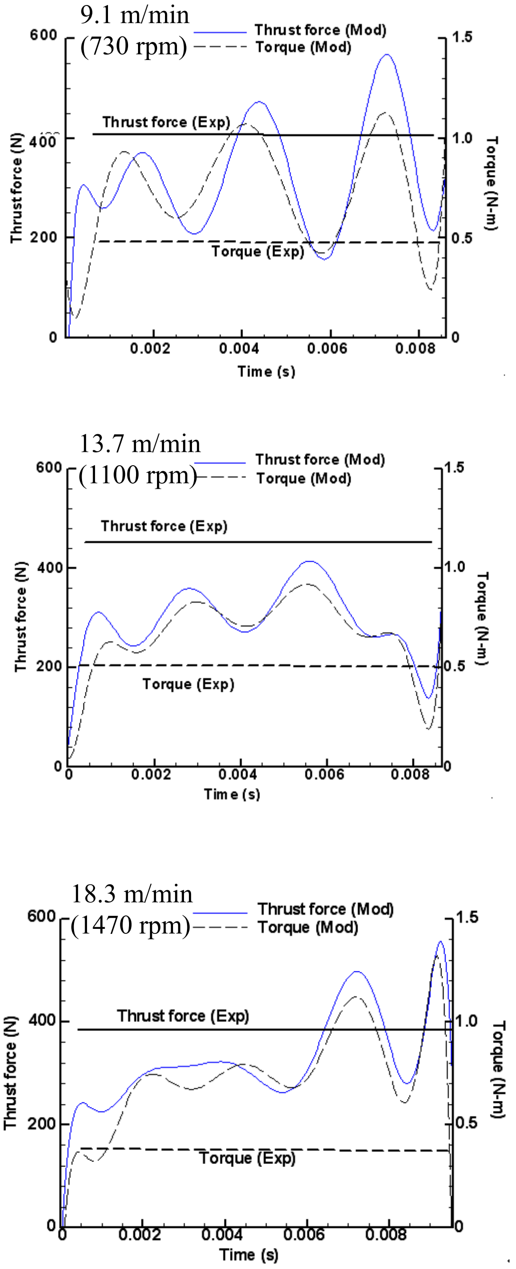

Figure F.3. Comparison of modeling and experimental thrust forces and torques.

An example of the chip formation process is shown in Figure F.4. The cutting speed for the selected example is 13.7 m/min. The chip and the engagement of the drill and workpiece are shown in Figure F.4(a).

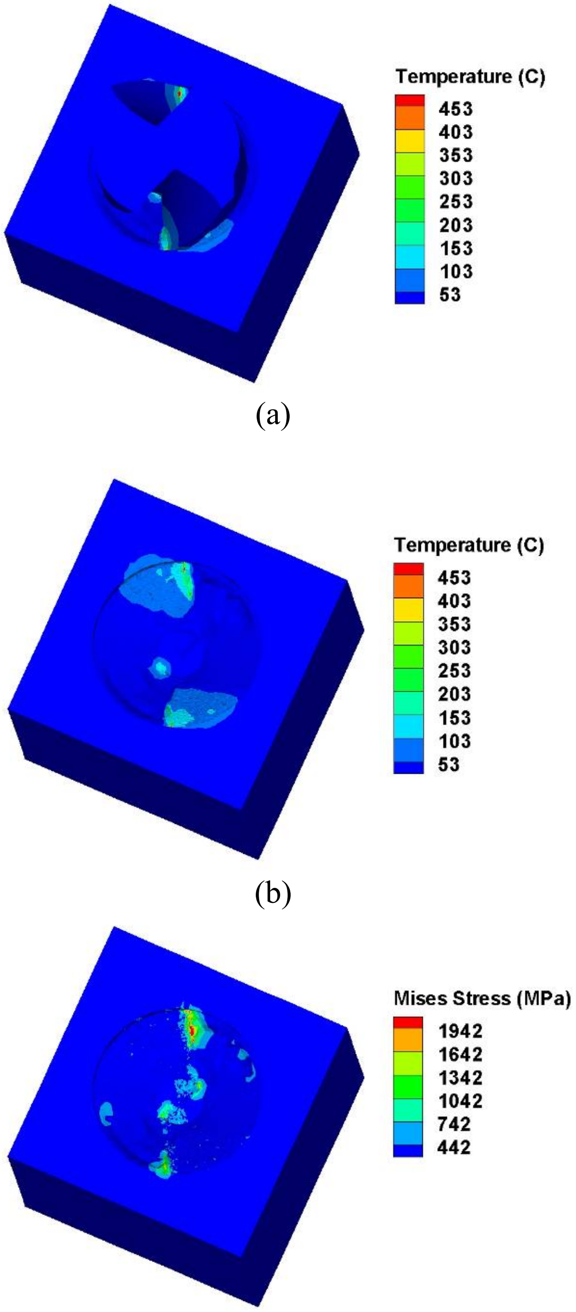
Temperature (C)
453
403
353
303
253
203
153
103
53
Temperature (C)
453
403
353
303
253
203
153
103
53
Mises Stress (MPa)
1942
1642
1342
1042
742
442

(a)

(b)

(c)

Figure F.4. FEM results: (a) drill, chip, and workpiece temperature, (b) chip and workpiece temperature, and (c) chip and workpiece von Mises stress (13.7 m/min peripheral cutting speed).

Figure F.4(b) shows the temperature distribution of the chip and workpiece. The temperature of Ti chip is higher than the cut surface on the workpiece. The highest temperature, about 453°C, is concentrated in regions contacting the drill cutting edge near the drill margin, where the cutting speed is the highest along the cutting edge. The distribution of von Mises stress of the chip and workpiece is shown in Figure F.4(c). The region of high stress coincides with the region with high temperature.

F.5. Tool Performance

Tool temperature is a key factor that accelerates the tool wear and limits the cutting speed and productivity in Ti machining. Experimental measurement of tool temperature is difficult. On the contrary, the finite element simulation can predict the tool temperature under various cutting conditions. Figure F.5(a) shows the temperature distribution on the drill flank face. The high temperature of this twist drill is concentrated at the cutting edge near the margin. This is consistent with the temperature pattern of Li and Shih (2007a). The peak temperature reaches 405°C which is slightly lower than the peak chip temperature, after drilling about 0.008 s. The tool temperature is increasing with the drilling time (Li and Shih, 2007a). Such high temperature is detrimental to the tool life. The distribution of von Mises stress of the tool is shown in Figure F.5(b). Similar to the chip, the region of high stress almost coincides with the region of high temperature. The peak stress of tool is 4651 MPa which is higher than that of chips.

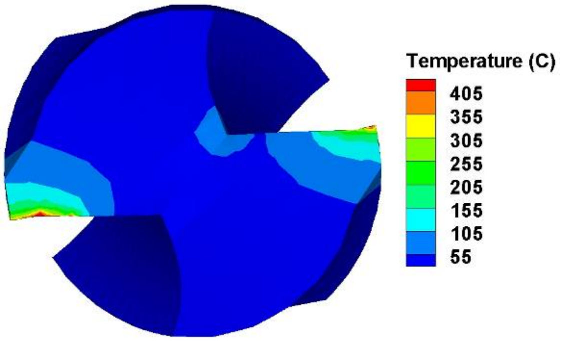
Temperature (C)
405
355
305
255
205
155
105
55

(a)

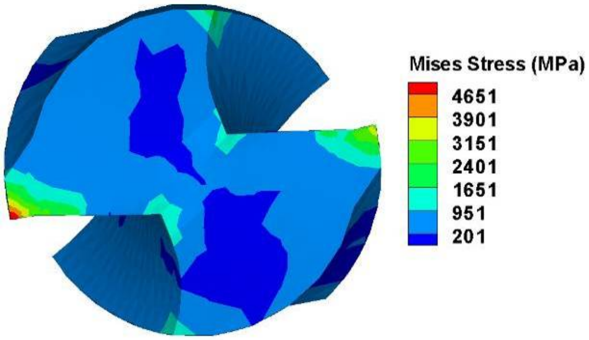
Mises Stress (MPa)
4651
3901
3151
2401
1651
951
201

(b)

Figure F.5. FEM results of drill: (a) temperature and (b) mises stress distributions (13.7 m/min peripheral cutting speed).

F.6. Effect of Cutting Speed

Figure F.6 shows the effect of cutting speed on the peak temperature and von Mises stress on chip and tool. The peak chip temperature increases from 294ºC at 9.1 m/min cutting speed to 589ºC at 18.3 m/min cutting speed. The peak tool temperature increases from 241°C at 9.1 m/min cutting speed to 532°C at 18.3 m/min cutting speed. This demonstrates the effect of high speed on tool temperature quantitatively. The peak tool stress also increases from 3176 MPa at 9.1 m/min cutting speed to 5861 MPa at 18.3 m/min cutting speed. The peak chip stress does not linearly increase with the cutting speed. The maximum chip stress occurs at 13.7 m/min cutting speed. Further increase of cutting speed results in decreased stress because the thermal softening effect outweighs the strain rate hardening effect.

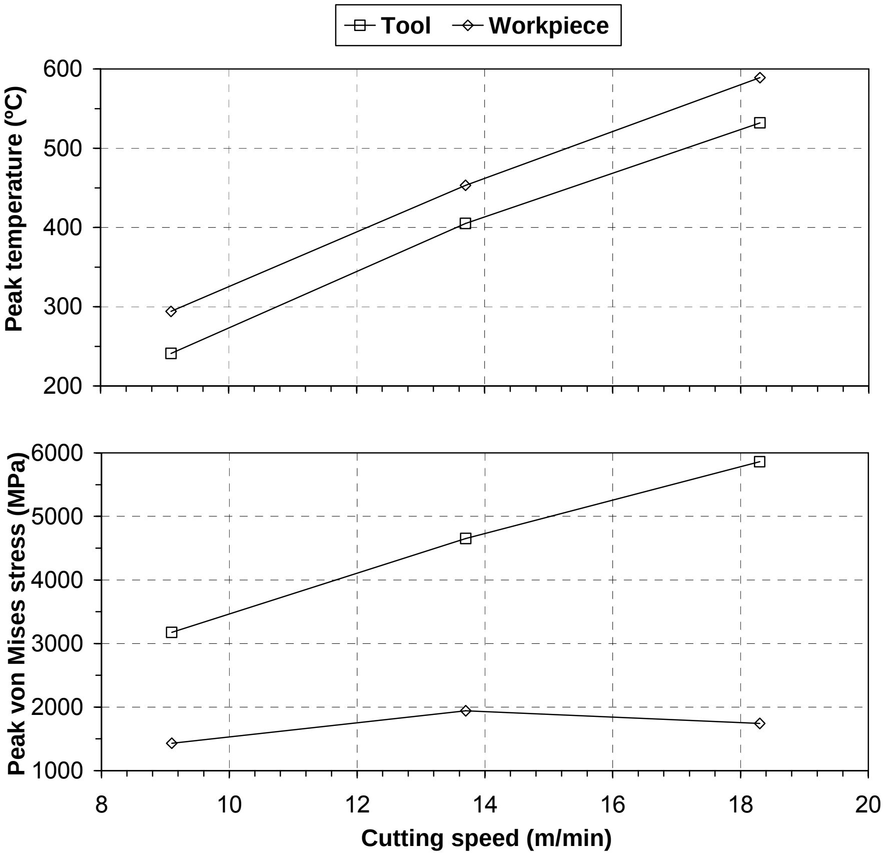

Figure F.6. Peak temperature and von Mises stress vs. drill peripheral cutting speed.

F.7. CONCLUSIONS

Accurate prediction of drilling process behavior including cutting forces, tool and workpiece temperatures, stresses, etc. is necessary for the understanding of the process and subsequent improvement to be made. A 3D FEM model is presented which includes fully adaptive unstructured mesh generation, tight thermo-mechanically coupling, deformable tool-chip-workpiece contact, interfacial heat transfer across the tool-chip boundary, momentum effects at high speeds and constitutive models appropriate for high strain rate, finite deformation analyses. To substantiate the efficacy of numerical and constitutive formulations used, actual drilling tests are performed on Ti-6Al-4V. The thrust force and torque are collected and compared with modeling results for validation. The model provides good estimation of thrust force but the torque is overestimated by 50%. Further improvement of the FEM drilling model is currently ongoing. This study shows that the FEM drilling model is able to predict changes in cutting forces, temperatures, and stresses with respect to drilling process parameters such as cutting speed.

BIBLIOGRAPHY

Bibliography

Agapiou, J. S., Stephenson, D. A., 1994, "Analytical and Experimental Studies of Drill Temperatures," Journal of Engineering for Industry, 116(1), pp. 54-60.

Arai, M., Ogawa, M., 1997, "Effects of High Pressure Supply of Cutting fluid in Drilling of Titanium Alloy," Keikinzoku/Journal of Japan Institute of Light Metals, 47(3), pp. 139-144.

Armarego, E. J. A., Cheng, C. Y., 1972, "Drilling with Flat Rake Face and Conventioanl Twist Drills – I. Theoretical Investigation," International Journal of Machine Tools and Manufacture, 12, pp. 17-35.

Bagci E. and B. Ozcelik B., 2006, "Finite Element and Experimental Investigation of Temperature Changes on a Twist Drill in Sequential Dry Drilling," International Journal of Advanced Manufacturing and Technology, 28, pp. 680-687.

Bakkal, M., Liu, C. T., Watkins, T. R., Scattergood, R. O., Shih, A. J., 2004, "Oxidation and Crystallization of Zr-Based Bulk Metallic Glass Due to Machining," Intermetallics, 12(2), pp. 195-204.

Bakkal, M., Shih, A. J., McSpadden, S. B., Liu, C. T., Scattergood, R. O., 2005, "Light Emission, Chip Morphology, and Burr Formation in Drilling the Bulk Metallic Glass," International Journal of Machine Tool and Manufacture, 45(7-8), pp. 741-755.

Balkrishna, R., Shin, Y. C., 2002, "A Study on the High Speed Face Milling of Ti-6Al-4V Alloy," Proceedings of 2002 ASME International Mechanical Engineering Congress and Exposition, New Orleans, LA, MED 13, pp. 277-286.

Barber, J. R., 2001, *Intermediate Mechanics of Materials*, McGraw-Hill, Boston.

Barry, J., Byrne, G., Lennon, D., 2001, "Observations on Chip Formation and Acoustic Emission in Machining Ti-6Al-4V Alloy," International Journal of Machine Tools and Manufacture, 41(7), pp. 1055-1070.

Bayoumi, A. E., Xie, J. Q., 1995, “Some Metallurgical Aspects of Chip Formation in Cutting Ti-6wt%Al-4wt%V Alloy,” Material Science and Engineering, A190, pp. 173-180.

Berliner, E. M. and Krainov, V. P., 1991, “Analytic Calculations of the Temperature Field and Heat Flows on the Tool Surface in Metal Cutting due to Sliding Friction,” Wear, 143, pp. 379-395.

Bono, M. and Ni, J., 2001, “The Effects of Thermal Distortions on the Diameter and Cylindricity of Dry Drilled Holes,” International Journal of Machine Tools and Manufacture, 41(15), pp. 2261-2270.

Bono, M. and Ni, J., 2002, “A Method for Measuring the Temperature Distribution along the Cutting Edges of a Drill,” Journal of Manufacturing Science and Engineering, 124, pp. 921-926.

Bono, M. and Ni, J., 2006, “The Location of the Maximum Temperature on the Cutting Edges of a Drill,” International Journal of Machine Tools and Manufacture, 46, 901-907.

Cantero, J., Tardío, M., Canteli, J., Marcos, M., Miguélez, M., 2005, “Dry drilling of alloy Ti-6Al-4V”, International Journal of Machine Tool s and Manufacture, 45(11), pp. 1246-1255.

Che-Haron, C. H. 2001, “Tool Life and Surface Integrity in Turning Titanium Alloy,” Jouranl of Materials Processing Technology, 118(1-3), pp. 231-237.

Chen, W.-C., 1996, “Effect of the Cross-Sectional Shape Design of a Drill Body on Drill Temperature Distributions,” International Communications in Heat and Mass Transfer, 23(3), pp. 355-366.

Chen, W. F. and Han, D. J., 1988, *Plasticity for Structural Engineers,* Springer-Verlag, New York.

Chernvavskii, K. S., Travushkin, G. G., Sapronova, Z. N., Aleksandrovich, A. A., 1993, “Micromechanisms of Deformation and Failure at Successive Stages of Compressive Loading of Hard Alloys WC-Co,” Strength of Materials, 25, pp. 746-54.

Cullity, B. D., 1978, *Elements of X-Ray Diffraction*, Addison-Wesley, Reading, MA.

DeVries, M. F., Wu, S. M., Mitchell, J. W., 1967, “Measurement of Drilling Temperature by the Garter Spring Thermocouple Method,” Microtecnic Journal, 21(6), pp. 583-586.

Donachie, Jr., M. J., 1988, *Titanium: A Technical Guide*, ASM International, Material Park, OH.

Dornfeld, D. A., Kim, J. S., Dechow, H., Hewson, J., Chen, L. J., 1999, “Drilling Burr Formation in Titanium Alloy, Ti-6Al-4V,” CIRP Annals - Manufacturing Technology, 48(1), pp. 73-76.

Ehmann, K. F., Kapoor, S. G., Devor, R. E., Lazoglu I., 1997, “Machining Process Modeling: A Review,” Journal of Manufacturing Science and Engineering, 119, pp. 655-663.

Ernst, H., Haggerty, W. A., 1958, “Spiral Point Drill – New Concept in Drill Point Geometry,” ASME Transactions, 80, pp. 1059-1072.

Ezugwu, E. O., Wang, Z. M., 1997, “Titanium alloys and their machinability-a review,” Journal of Materials Processing Technology, 68(3), pp. 262-274.

Fuh, K. H., 1987, *Computer Aided Design and Manufacturing of Multi-Facet Drills*, PhD Dissertation, University of Wisconsin at Madison.

Guo, Y. B., Dornfeld, D. A., 1998, “Finite Element Analysis of Drilling Burr Minimization with a Backup Material,” Transactions of the North American Manufacturing Research Institution of SME, 26, pp. 207-212.

Guo, Y. B., Dornfeld, D. A., 2000, “Finite Element Modeling of Burr Formation Process in Drilling 304 Stainless Steel,” Journal of Manufacturing Science and Engineering, 122, pp. 612-619.

Himmelblau, D. M., 1972, *Applied Nonlinear Programming*, McGraw-Hill, New York.

Hinds, B. K. and Treanor, G. M., 2000, “Analysis of Stresses in Micro-Drills using the Finite Element Method,” International Journal of Machine Tools and Manufacture, 40(10), pp. 1443-1456.

Hirosaki, K., Shintani, K., Kato, H., Asakura, F., Matsuo, K., 2004, “High Speed Machining of Bio-titanium Alloy with a Binder-less PcBN tool, JSME International Journal, Series C: Mechanical Systems, Machine Elements and Manufacturing, 47(1), pp. 14-20.

Huang, C.-H., Jan, L.-C., Li, R., Shih, A.J., 2007 “A Three-Dimensional Inverse Problem in Estimating the Applied Heat Flux of a Titanium Drilling – Theoretical and Experimental Studies,” International Journal of Mass and Heat Transfer (accepted).

Huang, Y., and Liang, S. Y., 2005, “Cutting Temperature Modeling Based on Non-Uniform Heat Intensity and Partition Ratio,” Machining Science and Technology, 9(3), pp. 301-323.

Hurless, B. E., Froes, F. H., 2002, "Lowering the Cost of Titanium," The AMPTIAC Quarterly, 6(2), pp. 3-9.

Kalidas, S. Kapoor, S. G., DeVor, R. E., 2002, "Influence of Thermal Effects on Hole Quality in Dry Drilling, Part 1: a Thermal Model of Workpiece Temperatures," Journal of Manufacturing Science and Engineering, 124, 258-266.

Karpat, Y., Ozel, T., 2005, "An Analytical-Thermal Modeling Approach for Predicting Forces, Stresses and Temperatures in Machining with Worn Tools," Proceedings of 2005 ASME International Mechanical Engineering Congress and Exposition, 16(1), pp. 489-498.

Ke, F., 2003, *Analysis and Modeling of Chip Ejection in Deep Hole Drilling Process*, PhD Dissertation, University of Michigan.

Ke, F., Ni, J., Stephenson, D. A., 2005, "Continuous Chip Formation in Drilling," International Journal of Machine Tools and Manufacture, 45(15), pp. 1652-1658.

Klopp, R. W., Clifton, R. J., Shawki, T. G., 1985, "Pressure-Shear Impact and the Dynamic Viscoplastic Response of Metals," Mechanics of Materials, 4, pp. 375-385.

Kitagawa, T., Kubo, A., Maekawa, K., 1997, "Temperature and Wear of Cutting Tools in High-speed Machining of Inconel 718 and Ti-6Al-6V-2Sn," Wear, 202, pp. 142-148.

Koch U. and Levi R., 1971, "Some Mechanical and Thermal Aspects of Twist Drill Performance," CIRP Annals, 19, pp. 247-254.

Komanduri, R., Von Turkovich, B. F., 1981, "New Observations on the Mechanism of Chip Formation when Machining Titanium Alloys," Wear, 69(2), pp. 179-188.

Komanduri, R., 1982, "Some Clarifications on the Mechanics of Chip Formation when Machining Titanium," Wear, 76(1), pp. 15-34.

Komanduri, R., Hou, Z. B., 2002, "On the Thermoplastic Shear Instability in the Machining of a Titanium Alloy (Ti-6Al-4V)," Metallurgical and Materials Transactions, 33A(9), pp. 2995-3010.

Kraft, E. H., 2002, Opportunities for Low Cost Titanium in Reduced Fuel Consumption, Improved Emission, and Enhanced Durability Heavy-Duty Vehicles, Oak Ridge National Laboratory Report ORNL/Sub/4000013062/1, July 2002.

Kraft E. H., 2003, Summary of Emerging Titanium Cost Reduction Technologies, Oak Ridge National Laboratory Report ORNL/Sub/4000023694/1, December 2003.

Law, S. S., DeVries, M. F., Wu, S. M., 1972, “Analysis of Drill Stress by Three-Dimensional Photoelasticity,” Journal of Engineering for Industry, Transactions of the ASME, 94, pp. 965-970.

Lei, S. and Liu, W., 2002, “High-speed machining of titanium alloys using the driven rotary tool,” International Journal of Machine Tools and Manufacture, 42(6), pp. 653-661.

Li, R., Riester, L., Watkins, T. R., Blau, P. J., Shih, A. J., 2006, "Metallurgical Analysis and Nanoindentation Characterization of Ti-6Al-4V Workpiece and Chips in High Throughput Drilling," Materials Science and Engineering: A (submitted).

Li, R. and Shih, A. J., 2006, "High Throughput Drilling of Titanium Alloys," 2006 International Conference on Frontiers of Design and Manufacturing, Guangzhou, China, June 19-22, 2006.

Li, R., Hegde, P., Shih, A. J., 2007, “High-Throughput Drilling of Titanium Alloys,” International Journal of Machine Tools and Manufacture, 43, pp. 63-74.

Li, R. and Shih, A. J., 2007a, "Tool Temperature in Titanium Drilling," Journal of Manufacturing Science and Engineering (accepted).

Li, R. and Shih, A. J., 2007b, "Drill Temperature and Stress in High-Throughput Drilling of Ti Alloys," International Journal of Machine Tools and Manufacture (accepted).

Li, R. and Shih, A. J., 2007c, “Finite Element Modeling of High-Throughput Drilling of Ti-6Al-4V,” Transactions of the North America Manufacturing Research Institute of SME.

Lin, G. C., Mathew, P., Oxley, P. L. B., and Watson, A. R., 1982, “Predicting Cutting Forces for Oblique Machining Conditions,” Proceedings of the Institution of Mechanical Engineers, 196, pp. 141-148.

Lin, X. and Ni, J., 1999, Drill Design For High Throughput Hole Making, 1999, International Conference on Advanced Manufacturing Technology, June 16~18, 1999, Xi’an, China, pp. 162-166.

Lütjering, G., Williams, J. C., 2003, *Titanium*, Springer, Berlin.

Machinability Data Center, *Machining Data Handbook*, Metcut Research Associateds, Inc., 1980.

Machado, A. R., Wallbank, J., 1990, “Machining of Titanium and Its Alloys-A Review,” Proceedings of Institution of Mechanical Engineers, Part B: Management and Engineering Manufacture, 204(1), pp. 53-60.

Mantle, A. L., Aspinwall, D. K., 2001, “Surface Integrity of a High Speed Milled Gamma Titanium Alumide,” Journal of Materials Processing Technology, 118(1-3), pp.143-150.

Marusich, T. D., Ortiz, M., 1995, “Modeling and Simulation of High-Speed Machining,” International Journal for Numerical Methods in Engineering, 38(21), pp. 3675-3694.

Marusich, T. D., Usui, S., Aphale, R., Saini, N., Li, R., Shih, A. J., 2006, “Three-Dimensional Finite Element Modeling of Drilling Processes,” 2006 ASME International Conference on Manufacturing Science and Engineering, October 8-11, 2006, Ypsilanti, Michigan.

Material Properties Handbook: Titanium Alloys, ASM International, Materials Park, OH, 1994.

Mills, B. Mottishaw, T., Chisholm, A., 1981, “The Application of Scanning Electron Microscopy to the Study of Temperatures and Temperature Distributions in M2 High Speed Steel Twist Drills,” CIRP Annals, 30, pp. 15-20.

Min S., Dornfeld, D. A., Kim, J., Shyu, B., 2001, “Finite Element Modeling of Burr Formation in Metal Cutting,” Machining Science and Technology, 5, pp. 307-322.

Nakayama, K., 1974, Formation of “Saw-Toothed Chip” in Metal Cutting, International Conference on Production Engineering, August 26-29, Tokyo, Japan.

Norihiko, N., 2002, “High-speed Machining of Ti Alloy,” Chinese Journal of Mechanical Engineering, 15, pp. 109-114.

Oliver, W. C., Pharr, G. M., 1992, “Improved Technique for Determining Hardness and Elastic Modulus using Load and Displacement Sensing Indentation Experiments,” Journal of Materials Research, 7(6), pp. 1564-1580.

Orfueil, M., 1987, *Electric Process Heating*, Battelle Press, Ohio.

Ozisik M. and Orlande H., 2000, *Inverse Heat Transfer*, Taylor & Francis, New York.

Park, S., Kapoor, S. G., Shiv, G., DeVor, R. E., 2006, “Microstructure-Level Model for the Prediction of Tool Failure in WC-Co Cutting Tool Materials,” Journal of Manufacturing Science and Engineering, Transactions of the ASME, 128, pp. 739-748.

Paul, B. and L. Mirandy, L., 1976, “An Improved Fracture Criterion for Three-Dimensional Stress States,” Journal of Engineering Materials and Technology, 98, pp. 159-163.

Qu, J. Riester, L., Shih, A. J., Scattergood, R. O., Lara-Curzio, E., Watkins, T. R., 2003, "Nanoindentation Characterization of Surface Layers of Electrical Discharge Machined WC-Co," Materials Science and Engineering A, 344(1-2), pp. 125-131.

Rahman, M., Wong, Y. S., Zareena, A. R., 2003, "Machininability of Titanium Alloys," JSME International Journal, Series C: Mechanical Systems, Machine Elements and Manufacturing, 46(1), pp. 107-115.

Reissig, L., Völkl, R., Mill, M. J., Glatzel, U., 2004, "Investigation of Near Surface Structure in order to Determine Process-Temperatures during Different Machining Processes of Ti6Al4V," Scripta Materialia, 50, pp. 121-126.

Sakurai, K., Adachi, K., Ogawa, K., Niba, R., 1992a, "Drilling of Ti-6Al-4V Alloy," Keikinzoku/Journal of Japan Institute of Light Metals, 42(7), pp. 389-394.

Sakurai, K., Adachi, K., Ogawa, K, 1992b, "Low Frequency Vibratory Drilling of Ti-6Al-4V alloy," Keikinzoku/Journal of Japan Institute of Light Metals, 42(11), pp. 633-637.

Sakurai, K., Adachi, K., Kamekawa, T., Ogawa, K., Hanasaki, S., 1996, "Intermittently Decelerated Feed Drilling of Ti-6%Al-4%V Alloy," Keikinzoku/Journal of Japan Institute of Light Metals, 46(3), pp. 138-143.

Saxena, U. K., DeVries, M. F., Wu, S. M., 1971, "Drill Temperature Distributions by Numerical Solutions," Journal of Engineering for Industry, 93(B4), pp. 1057-1065.

Schulz H. and Moriwaki, T., 1992, "High-speed Machining," CIRP Annals, 41(2), pp. 637-645.

Shaw, M. C., Cook, N. H., Smith, P. A., 1952, "Mechanics of Three-Dimensional Cutting Operations," American Society of Mechanical Engineers-Transactions, 74(6), pp. 1055-1064.

Shaw, M. C., Dirke, S. O., Smith, P. A., Cook, N. H., Loewen, E. G., Yang, C. T., 1954, Machining Titanium, MIT Report, 1954.

Shaw, M. C., 1984, Metal Cutting Principles, Oxford University Press, New York.

Sheikh-Ahmad, J., Bailey, J. A., 1997, "Flow Instability in the Orthogonal Machining of CP Titainium," Journal of Manufacturing Science and Engineering, 119(3), pp. 307-312.

Sheikh-Ahmad, J. Y., Quarless, V., Bailey, J. A., 2004, "On the role of Microcracks on Flow Instability in Low Speed Machining of CP Titanium," Machining Science and Technology, 8(3), pp. 415-430.

Shih, A. J., 1995, "Finite Element Simulation of Orthogonal Metal Cutting," ASME Journal of Engineering for Industry, 117, pp. 84-93.

Stabler, G., 1951, "The Fundamental Geometry of Cutting Tools," Institution of Mechanical Engineers-Proceedings, 165(63), pp. 14-21.

Stephenson, D.A., Agapiou, J.S. 2006, *Metal Cutting Theory and Practice*, CRC Taylor & Francis, Boca Raton, FL.

Strenkowski, J. S., Hsieh, C. C., and Shih, A. J., 2004, "An analytical finite element technique for predicting thrust force and torque in drilling," International Journal of Machine Tools and Manufacture, 44(12-13), pp. 1413-1421.

Takagi, J. and Shaw, M. C., 1981, "Evaluation of Fracture Strength of Brittle Tools," Annals of CIRP, 30, pp. 53-57.

Thangaraj, A., Wright, P. K., Nissle, M., 1984, "New Experiments on the Temperature Distribution in Drilling," Journal of Engineering Materials and Technology, Transactions of the ASME, 106, pp. 242-247

Trent, E. M., Wright, P. K., 2000, Metal Cutting, Butterworth-Heinemann.

Tueda, M. Hasegawa, Y., Nisina, Y. 1961, "The Study of Cutting Temperature in Drilling, 1st Report: on the Measuring Method of Cutting Temperature," Transaction of the Japan Society of Mechanical Engineers, 27, pp. 1423-1430.

Turner, P. C., Hansen, J. S., 1993, "Progress Toward Low-Cost Titanium," Advanced Materials and Processes, 143(1), pp. 42-43.

Usui, E., Ihara, T., Shirakashi, T., 1979, "Probabilistic Stress-Criterion of Brittle Fracture of Carbide Tool Materials," Bulletin of the Japan Society of Precision Engineering, 13, pp. 189-194.

van Luttervelt, C.A., Childs, T. H. C., Jawahir, I. S., Klocke, F., Venuvinod, P. K., 1998, "Present Situation and Future Trends in Modelling of Machining Operations -- Progress Report of the CIRP Working Group `Modelling of Machining Operations'," CIRP Annals - Manufacturing Technology, 47, pp. 587-626.

Vyas, A., Shaw, M. C., 1999, "Mechanics of Saw-Tooth Chip Formation in Metal Cutting," Journal of Manufacturing Science and Engineering, 121(2), pp. 163-172.

Wang, Jane-Lin, 1994, *Development of New Drilling Force Models for Improving Drill Point Geometries*, PhD Dissertation, University of Michigan

Watanabe, K., Yokoyama, K., Ichimiya, R., 1977, "Thermal Analyses of the Drilling Process," Bulletin of the Japan Society of Precision Engineering, 11(2), pp. 71-77.

Watkins, T. R., Cavin, O. B., Bai, J., and Chediak, J. A., 2003, "Residual Stress Determinations Using Parallel Beam Optics," pp. 119-129 in Advances in X-Ray Analysis, V. 46 CD ROM. Edited by T. C. Huang et al., ICDD, Newtown Square, PA.

Watson, A. R., 1985, "Drilling Model for Cutting Lip and Chisel Edge and Comparison of Experimental and Predicted Results I-Initial Cutting Lip Model," International Journal of Machine Tool Design and Research, 25(4), pp. 347-365.

Wiriyacosol, S., Armarego, E. J. A., 1979, "Thrust and Torque Prediction in Drilling from a Cutting Mechanics Approach," Annals of CIRP, 28, pp. 88-91.

Xie, J. Q., Bayoumi, A. E., Zbib, H. M., 1996, "A Study on Shear Banding in Chip Formation of Orthogonal Machining," 36(7), pp. 835-847.

Yang, X., Liu, C. R., 1999, "Machining Titanium and Its Alloys," Machining Science and Technology, 3(1), pp. 107-139.

Young, R. A., 1995, *Rietveld Method*, Oxford University Press, New York.

Zareena, A. R., Rahman, M., Wong, Y. S., 2001, "High Speed Machining of Aerospace Alloy Ti-6Al-4V," International SAMPE Technical Conference, 33, pp. 739-750.